DEVELOPMENT OF A RESONANCE IONIZATION SPECTROSCOPY ION-TRANSPORT PROBE FOR THE ENRICHED XENON OBSERVATORY

A DISSERTATION
SUBMITTED TO THE DEPARTMENT OF CHEMISTRY
AND THE COMMITTEE ON GRADUATE STUDIES
OF STANFORD UNIVERSITY
IN PARTIAL FULFILLMENT OF THE REQUIREMENTS
FOR THE DEGREE OF
DOCTOR OF PHILOSOPHY

María Montero Díez
May 2012

This dissertation is online at: http://purl.stanford.edu/rw784cm4325

I certify that I have read this dissertation and that, in my opinion, it is fully adequate in scope and quality as a dissertation for the degree of Doctor of Philosophy.

Giorgio Gratta, Primary Adviser

I certify that I have read this dissertation and that, in my opinion, it is fully adequate in scope and quality as a dissertation for the degree of Doctor of Philosophy.

Hongjie Dai

I certify that I have read this dissertation and that, in my opinion, it is fully adequate in scope and quality as a dissertation for the degree of Doctor of Philosophy.

William Moerner

Approved for the Stanford University Committee on Graduate Studies.

Patricia J. Gumport, Vice Provost Graduate Education

This signature page was generated electronically upon submission of this dissertation in electronic format. An original signed hard copy of the signature page is on file in University Archives.

Abstract

The Enriched Xenon Observatory (EXO) is a series of experiments seeking to measure the neutrino mass through observation of neutrinoless double beta decay ($0\nu\beta\beta$). The next generation of $0\nu\beta\beta$ experiments aims to probe Majorana neutrino masses at or below 10 meV. To reach this sensitivity, ton-scale detectors are needed with lower radioactive backgrounds than the best ones operating today. The EXO collaboration is developing a novel strategy for a virtually background-free search for the $0\nu\beta\beta$ of ^{136}Xe, based around detecting individual ^{136}Ba ions resulting from such decays. This dissertation details the efforts to develop a barium tagging technique which uses resonance ionization spectroscopy (RIS) to selectively and efficiently ionize barium atoms for injection and detection in an ion trap. A simple radionuclide-driven single-ion source has been developed to push the technology to high efficiency with a small number of ions.

Acknowledgements

Thank you to everyone who has helped me get to where I am today; this thesis would not have been completed without your help. To my advisor, Giorgio Gratta, for taking a chance and believing in me, for your infectious curiosity, and for showing me how science should be done. To Bill Fairbank, for always leading me down the right path. To my labmates, past and present, for providing not only ideas and encouragement but also endless entertainment (and candy and friendship). In particular to Karl Twelker, for doing more for this project than I could ever thank him for. To my friends, near and far, for making it so that I always have something to look forward to. I am lucky to have met you all! And most importantly, to my parents Enrique and Aurora and my sisters Cristina and Marta, for sacrificing so much so that I could find my own way in life and loving and supporting me in all my endeavors.

Contents

List of Tables

List of Figures

Chapter 1

Introduction

Over the last couple of decades, results of neutrino oscillation experiments such as SuperK [8], SNO [9], and KamLAND [10] have shown neutrinos to be massive particles. Although oscillation experiments have provided measurements of the mass differences between eigenstates [11], the absolute mass scale remains unknown. This remains one of the most important questions in particle physics, as measurement of the absolute neutrino masses may provide insight to physics beyond the Standard Model.

The Enriched Xenon Observatory (EXO) attempts to determine the effective neutrino mass by observation of the neutrinoless double beta decay ($0\nu\beta\beta$) of ^{136}Xe. This process is a yet unseen second-order weak interaction that is only allowed if neutrinos are their own antiparticles, and has a decay amplitude proportional to an effective neutrino mass [12]. Current lower limits on the half-life of $0\nu\beta\beta$ decay are $T_{1/2}^{0\nu\beta\beta} > 1.6\text{x}10^{25}$ yr for ^{76}Ge [13] ($T_{1/2}^{0\nu\beta\beta} > 5.7\text{x}10^{24}$ yr for ^{136}Xe [14]), resulting in a neutrino upper mass limit < 0.35 eV.

Improving on such a small mass limit requires both larger quantities of the target isotope and, perhaps more importantly, the reduction of the radioactive backgrounds that limit the experimental sensitivity to $0\nu\beta\beta$. The usage of ^{136}Xe as a source material in EXO has the fundamental advantage that the daugther of its double beta decay, ^{136}Ba, can be tagged. Verification of the presence of a Ba atom at the site of a $0\nu\beta\beta$ candidate event can eliminate all backgrounds except for the standard two neutrino double beta decay ($2\nu\beta\beta$) mode [15, 16]. Several barium tagging schemes

have already been investigated for EXO [17, 18]. This dissertation describes the development of an ion transport probe for the extraction, selective ionization, and detection of single Ba^+ ions using resonance ionization spectroscopy (RIS).

In Chapter 2, the physics of double beta decay is introduced, and a brief description of the EXO-200 experiment is given. The concept of RIS as a method of barium tagging for future EXO experiments is also discussed. Chapter 3 describes the theory behind resonance ionization processes, as well as the RIS scheme chosen to be most suitable for EXO, taking into consideration the electronic structure of barium, linewidth broadening, and saturation energies of transitions. In Chapter 4, evidence for the resonance ionization of barium from the vapor phase is presented, together with a description of the optical system, vacuum components, and data acquisition system used in the experimental setup. The experimentally determined lineshapes and saturation energies of the transitions are also discussed. Chapter 5 describes the development, fabrication, and characterization of a radionuclide-driven single-ion source that allows for efficiency measurements of the desorption and resonance ionization technique described in this dissertation. In Chapter 6, results from desorption and resonance ionization spectroscopy (DRIS) of Ba^+ are discussed. In this series of experiments, barium is deposited on a silicon substrate, thermally desorbed with a Nd:YAG laser, and resonantly ionized. Three experimental setups, each utilizing a different barium flux and ion guide system, are presented and an efficiency number is determined. Chapter 7 details future prospects for the RIS R&D program.

Chapter 2

The Search for the Neutrino Mass

The observation of flavor conversion in neutrino oscillation experiments implies that neutrinos are massive particles. If neutrinos have mass, then there is a spectrum of three or more neutrino mass eigenstates ν_1, ν_2, ν_3..., that are the analogues of the charged-lepton mass eigenstates e, μ, and τ. The weak interaction produces, in association with the charged lepton of flavor α, a neutrino of flavor α that is a superposition of mass eigenstates described by

$$|\nu_\alpha\rangle = \sum_i U^*_{\alpha i}|\nu_i\rangle \tag{2.1}$$

where U is the unitary leptonic mixing matrix.

Measurements of flavor oscillations in solar, atmospheric, and reactor neutrinos reveal information about neutrino mass differences, $\Delta m^2_{ij} = m^2_i - m^2_j$, but not much about absolute masses. In particular, the actual ordering of the mass states is not yet known. If the mass splittings are small compared to the absolute scale, $m_i \gg \sqrt{\Delta m^2_{ij}}$, then the states are degenerate. If they are of a similar magnitude, then there is a hierarchical pattern. In this case, if the mass states are ordered so as to coincide with their associated charged leptons (i.e. the m_1 state, which is mostly ν_e, should prove to be the lightest), then the mass states follow the normal hierarchy $m_1 < m_2 \ll m_3$, with the solar neutrino mass splitting below the atmospheric. If the mass splittings are reversed they follow the inverted hierarchy $m_3 \ll m_1 < m_2$.

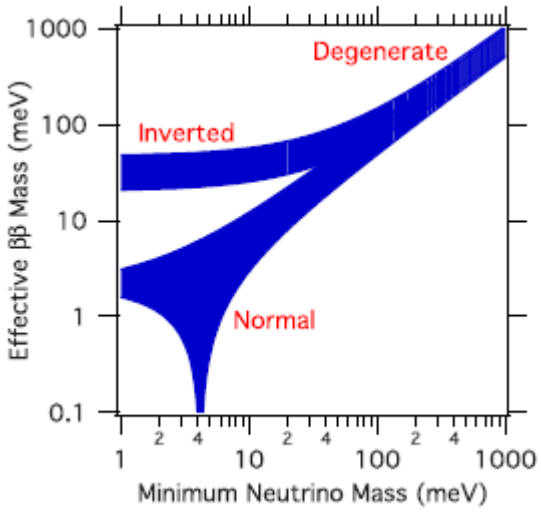

Figure 2.1: Effective Majorana mass $\langle m_{\beta\beta} \rangle$ vs. mass of the lightest neutrino state $m_{\nu_{min}}$. From [1].

Though unable to solve the absolute neutrino mass scale question, the results of oscillation experiments do provide some information. For example, the measured mass splitting responsible for atmospheric oscillations $|\Delta m^2_{32}|$ puts a lower limit on the heaviest neutrino mass, $m_h > 0.04$ eV [19]. Kinematic and cosmological experiments further constrain some of the parameters. The Mainz β spectrometer puts an upper limit on the neutrino mass scale $m_\nu \leq 2$ eV [20], and cosmological observations put an upper bound on the sum of the neutrino masses $\sum_{i=1}^{3} m_i < 0.17$ eV [21].

Of all experimental techniques used to investigate the neutrino mass, $0\nu\beta\beta$ might prove the most interesting. $0\nu\beta\beta$ can potentially probe mass limits in the meV range which, as shown in Fig. 2.1, could give information about the mass hierarchy. Furthermore, observation of $0\nu\beta\beta$ would imply that neutrinos are Majorana particles [1], that lepton number can be violated, and that new physics beyond the Standard Model is at work [22].

[1] That is, that neutrinos are their own antiparticles

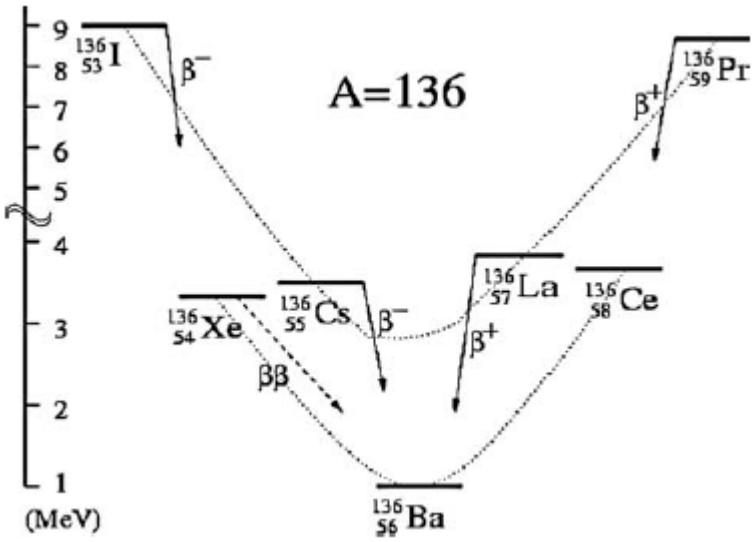

Figure 2.2: Mass parabolae for A = 136. Beta decay of ^{136}Xe to ^{136}Cs is energetically forbidden, but double beta decay of ^{136}Xe to ^{136}Ba is not. From [2].

2.1 Double Beta Decay

Double beta decay is a rare second-order process whereby a nucleus with charge Z and mass A decays into another with charge Z+2 and mass A. It occurs in (even-even) isotopes for which beta decay is energetically forbidden, either because both the initial and final nuclei are more tightly bound than the intermediate one or because the decay to the intermediate nucleus is highly hindered. This is shown for A = 136 in Fig. 2.2. Double beta decay typically proceeds from the ground state of the initial nucleus to the ground state of the final nucleus.

In the standard two neutrino mode ($2\nu\beta\beta$), two neutrons decay into two protons, two electrons, and two electron antineutrinos,

$$(Z, A) \rightarrow (Z + 2, A) + 2e^- + 2\bar{\nu}_e \tag{2.2}$$

This process conserves both electric charge and lepton number. On the other hand, the neutrinoless decay $0\nu\beta\beta$,

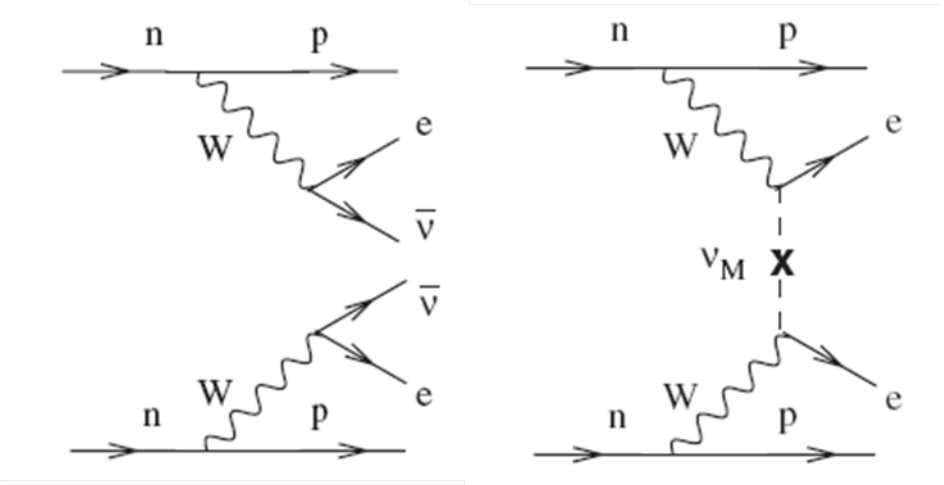

Figure 2.3: Feynman diagrams for two neutrino double beta decay (left) and neutrinoless double beta decay (right). From [1].

$$(Z, A) \rightarrow (Z + 2, A) + 2e^- \tag{2.3}$$

violates lepton number conservation and is forbidden in the standard electroweak theory. The Feynman diagrams illustrating these processes can be seen in Fig. 2.3. In $0\nu\beta\beta$ the $\bar{\nu}_e$ emitted at one vertex is absorbed as a ν_e at another, which can only happen if $\bar{\nu}_e = \nu_e$ and if $\Delta L_e = +2$. The amplitude of the projection of a neutrino onto a wrong-handed helicity is proportional to m_ν/E_ν, and the half-life of this process is proportional to the mass squared,

$$\left(T_{1/2}^{0\nu\beta\beta}\right)^{-1} = G^{0\nu\beta\beta}(Q, Z)\left|M_{GT}^{0\nu\beta\beta} - \frac{g_V^2}{g_A^2} M_F^{0\nu\beta\beta}\right|^2 \langle m_\nu \rangle^2 \tag{2.4}$$

where $G^{0\nu\beta\beta}(Q, Z)$ is a calculable phase-space factor dependent on the decay end-point energy and the nuclear charge, $M_{GT}^{0\nu\beta\beta}$ and $M_F^{0\nu\beta\beta}$ are nuclear matrix elements, g_V^2 and g_A^2 are vector coupling constants, and $\langle m_\nu \rangle$ is the effective neutrino mass [23]. As was described in the previous section, neutrinos created in a definite flavor eigenstate consist of a linear combination of mass eigenstates (see Eq. 2.1). This means that the calculation of the $0\nu\beta\beta$ amplitude involves taking the sum of the mass states

from which ν_e is derived. Each of the two vertices in the Feynman diagram (Fig. 2.3) contributes a factor proportional to $U_{\alpha i}$ so that the effective neutrino mass is given by

$$\langle m_\nu \rangle = \left| \sum_i m_i U_{\alpha i}^2 \right| \tag{2.5}$$

The two double beta decay modes can be easily distinguished by the shape of their electron energy spectra. Fig. 2.4 illustrates these spectra. In the two neutrino mode, the emitted antineutrinos carry some of the energy of the decay, and the summed energy spectrum of the two electrons forms a continuum between zero and the Q-value of the decay. In the neutrinoless mode, the two electrons carry the full energy [2] and the energy spectrum is a delta function at the Q-value. As can be seen from the inset in Fig. 2.4, smearing due to energy resolution means that $2\nu\beta\beta$ is a background for the $0\nu\beta\beta$ mode. The energy spectrum and the decay rate of the $2\nu\beta\beta$ mode thus have to be well understood before any claims can be made about $0\nu\beta\beta$.

$2\nu\beta\beta$ has been observed in various nuclei, including the recent first observation of this decay in ^{136}Xe by the EXO-200 experiment [24], which will be briefly described in the next section. A summary of experimentally measured $2\nu\beta\beta$ half-lives and their corresponding nuclear matrix elements is shown in Table 2.1. A claim of evidence of $0\nu\beta\beta$ in ^{76}Ge has been made by part of the Heidelberg-Moscow collaboration [25, 26], but it has been challenged by much of the particle physics community, including other members of that collaboration [27]. Confirmation or rejection of this claim is thus a goal of the current generation of $0\nu\beta\beta$ experiments.

In order to achieve their goals, double beta decay experiments need to address several factors. First of all, the energy resolution has to be good enough to separate the $2\nu\beta\beta$ contribution to the $0\nu\beta\beta$ spectrum. Secondly, the $0\nu\beta\beta$ count rate has to be maximized while minimizing background. The effective Majorana mass sensitivity is proportional to certain experimental parameters. Specifically, in double beta decay experiments,

[2] The nuclear recoil is negligible for practical purposes

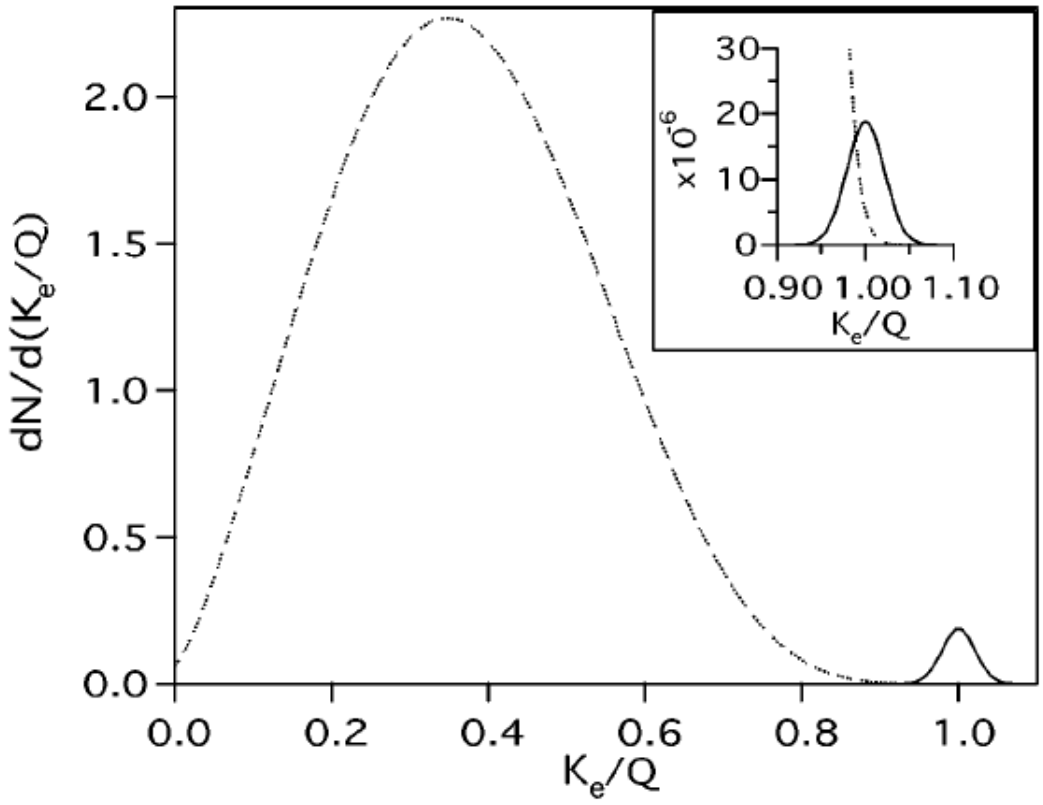

Figure 2.4: Spectra of the sum of the electron kinetic energies K_e from $2\nu\beta\beta$ (dashed) and $0\nu\beta\beta$ (solid), normalized by the decay endpoint Q. The $0\nu\beta\beta$ spectrum is normalized to 10^{-2} (10^{-6} in the inset). All spectra are convolved with an energy resolution of 5%. From [3].

	$T_{1/2}$ (yr)	$M^{2\nu}$ (MeV^{-1})
^{48}Ca	$(4.3^{+2.4}_{-1.1}\pm1.4)x10^{19}$	0.05±0.02 [28]
^{76}Ge	$(1.74\pm0.01^{+0.18}_{-0.16})x10^{21}$	0.13±0.01 [29]
^{82}Se	$(9.6\pm0.3\pm1.0)$x10^{19}	0.10±0.01 [30]
^{96}Zr	$(2.35\pm0.14\pm0.16)$x10^{19}	0.12±0.01 [31]
^{100}Mo	$(7.11\pm0.02\pm0.54)$x10^{18}	0.23±0.01 [30]
^{116}Cd	$(2.9^{+0.4}_{-0.3})$x10^{19}	0.13±0.01 [32]
^{128}Te	$(1.9\pm0.1\pm0.3)$x10^{24}	0.05±0.005 [33]
^{130}Te	$(7.0\pm0.9\pm1.1)$x10^{20}	0.033±0.003 [34]
^{136}Xe	$(2.1\pm0.04\pm0.21)$x10^{21}	0.019±0.001 [24]
^{150}Nd	$(9.1^{+0.25}_{-0.22}\pm0.63)x10^{18}$	0.06±0.003 [35]
^{238}U	(2.2 ± 0.6)x10^{21}	0.05±0.01 [36]

Table 2.1: Summary of experimentally determined $2\nu\beta\beta$ half-lives and nuclear matrix elements.

$$\langle m_\nu \rangle \ = (2.50 \times 10^{-8} \text{ eV}) \left[\frac{W}{f x \epsilon G^{0\nu\beta\beta} |M^{0\nu\beta\beta}|^2} \right]^{1/2} \left[\frac{b \Delta E}{MT} \right]^{1/4} \tag{2.6}$$

or

$$\langle m_\nu \rangle \ = (2.67 \times 10^{-8} \text{ eV}) \left[\frac{W}{f x \epsilon G^{0\nu\beta\beta} |M^{0\nu\beta\beta}|^2} \right]^{1/2} \frac{1}{\sqrt{MT}} \tag{2.7}$$

where W is the molecular weight of the source material, f is the isotopic abundance, x is the number of double beta decay candidate atoms per molecule, ϵ is the detector efficiency, b is the number of background counts, ΔE is the energy window for $0\nu\beta\beta$, M is the mass of the isotope, T is the live time of the experiment, and $|M^{0\nu\beta\beta}|$ is shorthand for the $0\nu\beta\beta$ nuclear matrix elements [3]. In the first case (Eq. 2.6), the mass sensitivity is determined by statistical fluctuations in the background rate, scaling with the detector mass and live time, so that $\langle m_\nu \rangle \propto (MT)^{-1/4}$. This is the case when trace radioactive impurities are present. In the other hand, if radioactive impurities are eliminated, then the mass sensitivity is simply a function of the statistical fluctuations of the count rate itself (Eq. 2.7), $\langle m_\nu \rangle \propto (MT)^{-1/2}$. The minimization of radioactive backgrounds is thus an important design consideration

for double beta decay experiments.

2.2 The Enriched Xenon Observatory (EXO)

The Enriched Xenon Observatory (EXO) is a proposed ton-scale experiment designed to search for the $0\nu\beta\beta$ of ^{136}Xe. Using ^{136}Xe as the source material presents several advantages, chief amongst them the possibility of tagging the ^{136}Ba daugther of decay for background reduction purposes. Moreover, as a noble gas, Xe is relatively easy to enrich and allows for purification during experimental operation. Additionally, there are no long-lived isotopes that can be activated.

The present phase of the experiment, called EXO-200, comprises 175 kg of Xe enriched 80.6% in the A = 136 isotope. It is currently operating 2150 feet (1600 meters of water equivalent) underground at the Waste Isolation Pilot Plant (WIPP) in Carlsbad, NM. A schematic diagram of the detector is shown in Fig. 2.5. Xe serves both as the source and the detector in a liquid phase Time Projection Chamber (TPC), housed inside a thin copper vessel (3). This vessel is surrounded by an ultra-clean, high-density fluid (HFE-7000 [37]) that provides radiation shielding and keeps the xenon at a constant 167 K operating temperature (1). The HFE is housed inside a double-walled, vacuum insulated (2) copper cryostat (5). The outermost shielding layer consists of 25 cm of lead (4). The entire apparatus is housed in a nominally class-1000 cleanroom, surrounded by a muon veto system that provides ∼96% rejection efficiency for muons traversing lead. In order to minimize the radioactive backgrounds that can deposit energy near the ^{136}Xe $\beta\beta$ decay Q-value (2457.8 keV [38]), care is taken to select ultra-low radioactivity construction materials in EXO-200. A list of specific materials employed can be seen in [39].

Good detector energy resolution (∼1%) is needed in order to resolve the $2\nu\beta\beta$ background in the $0\nu\beta\beta$ decay. In EXO-200, the energy resolution is optimized by recording both ionization and scintillation signals in the TPC (Fig. 2.6). When a double beta decay occurs, the electrons ionize the surrounding Xe. Some of the ionized Xe recombines into excited dimers, which then emit 178 nm scintillation light. This light is detected by two arrays of large area avalanche photo diodes (LAAPDs [40],

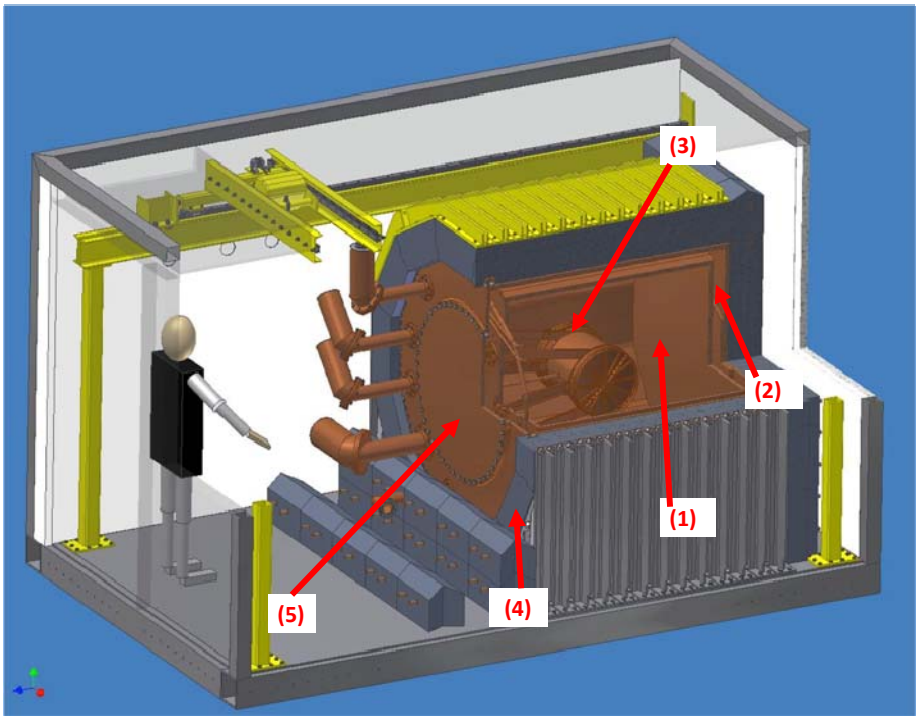

Figure 2.5: Schematic of the EXO-200 detector assembly. (1) HFE volume. (2) Vacuum insulation. (3) Xe vessel. (4) Lead shielding. (5) Outer copper cryostat.

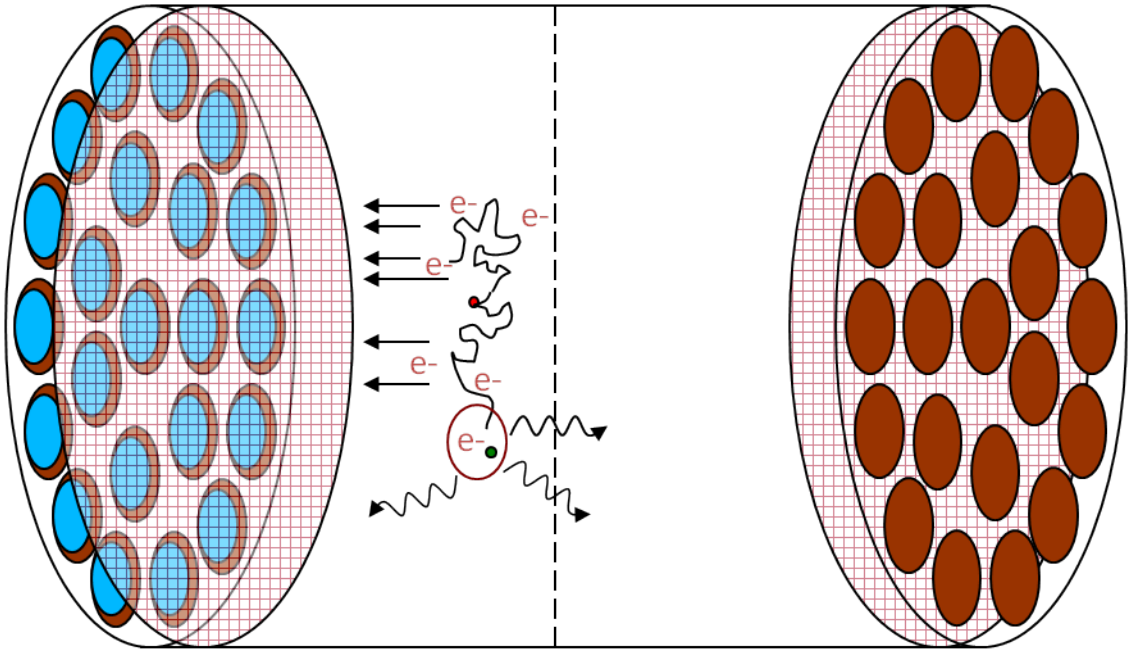

Figure 2.6: Schematic of the EXO-200 TPC. A $\beta\beta$ event ionizes some of the surrounding xenon. Recombination of some of this ionization produces scintillation, detected by the LAAPDs at either end. The rest is drifted to cross-wire anodes for detection.

468 total), and serves as a "start" time for the event. The remaining electrons are drifted to a cross-wire anode where they are collected. The electron drift time can be calculated by using the difference in arrival time of the scintillation and ionization signals, and this allows for three-dimensional position reconstruction. A more detailed description of the detector is given in [41].

2.3 Barium Tagging in Ton-Scale EXO

The current EXO-200 detector was built to better understand the performance of a large liquid xenon TPC, to test the ability to build a low-background experiment, to establish new neutrino mass limits, and to try to make a statement about the claim by [25, 26]. In order to achieve the required sensitivity for neutrino mass hierarchy

determination (see Fig. 2.1), a future EXO experiment is expected to consist of 1-10 tons of enriched ^{136}Xe, in either the liquid or gas phase. It will make use of the techniques employed in EXO-200 to achieve high energy resolution and low radioactive backgrounds. More importantly, this experiment will also tag the barium daughter of the $0\nu\beta\beta$ decay of ^{136}Xe as a means of reducing all backgrounds except for the $2\nu\beta\beta$ mode.

In a LXe TPC, barium tagging will proceed by inserting a special tip after a $\beta\beta$ event. The tip will electrostatically attract the Ba ion produced in the decay, and either directly identify it by means of atomic spectroscopy or transfer it to a vacuum system where the identification is performed. Although the Ba daugther of the $\beta\beta$ decay is produced in a 2+ state, it is likely that it is stable as a 1+ ion in LXe because of the relative ioniziation energies of barium and xenon and the band structure that xenon exhibits in its liquid phase.

For a direct identification tagging scheme, the idea is that the Ba^+ daughter could be drawn to a small optical fiber tip (or the tip could be inserted to the decay site) and captured in a SXe matrix by rapidly lowering the temperature of the tip below the Xe freezing point. Detection of the Ba^+ would then be done by laser-induced fluorescence using the fiber for both laser light delivery and fluorescence collection. The detection process might occur with the tip still in the LXe or with the tip extracted to the region of ambient Xe gas pressure above the LXe.

Different methods of ion transfer, including a sharp tunneling microscope tip and a cryogenic quartz probe [18], haven been investigated by the EXO collaboration without much success. On the other hand, single barium ion trapping in a buffer gas-filled ion trap and identification with resonance fluorescence have already been achieved [42].

Table 2.2 shows the projected mass sensitivities for ton-scale EXO using barium tagging, thus assuming no background due to radioactivity. It also assumes 80% enrichment in the A = 136 isotope and a 68% overall efficiency determined from current EXO-200 data analysis. The range in the $\langle m_\nu \rangle$ sensitivities arises from uncertainties in the calculations of the nuclear matrix elements, which are model dependent.

Case	Mass	Eff	Time	σ_E/E	2ν bkg	$T_{1/2}^{0\nu\beta\beta}$	$\langle m_\nu \rangle$
Conserv.	2 ton	68%	5 yr	1.6%	5.0 evts	2.8×10^{27} yr	16-20 meV
Aggress.	10 ton	68%	10 yr	1%	3.4 evts	3.4×10^{28} yr	4.7-5.8 meV

Table 2.2: Projected ton-scale EXO sensitivity for conservative and aggressive energy resolution and exposure estimates.

2.3.1 Using resonance ionization spectroscopy for barium tagging

If barium detection is to occur away from the LXe TPC, it is imperative to develop an efficient single-ion transport probe. Resonance ionization spectroscopy (RIS) provides a highly selective one-atom release and detection method. Efficiencies up to 25% using such a method have already been reported [43].

A resonance ionization probe makes use of the electronic transitions particular to barium to selectively and efficiently ionize these atoms. Two laser pulses are used to first excite and then ionize barium atoms. The most elegant implementation of a RIS probe delivers all laser pulses through a fiber (Fig. 2.7). In this setup, a 400 μm fiber with a metalized end biased at a negative potential is inserted near the event site in liquid Xe after a $\beta\beta$ trigger. The Ba^+ ion is attracted to the tip and trapped. The tip is then moved to an ion trap. The barium is released with a laser pulse (as a neutral), resonantly ionized with two other pulses, and injected into the trap where it is detected. The advantage of this setup is that, since the desorption and RIS lasers are concentrated to the same small area, high efficiency with low pulse energies can be achieved.

This fiber implementation is, however, not the only one considered, and is presently beyond the scope of this work. The alternative presented here employs desorption from a silicon substrate and resonance ionization in free space. A barium oven and a radionuclide-driven barium source are used to simulate barium produced by double beta decay. This experimental setup offers the flexibility of identifying barium spectroscopically or via mass spectrometry, without the need for an ion trap. The work presented in this dissertation is a precursor to a probe, briefly described in Chapter 7,

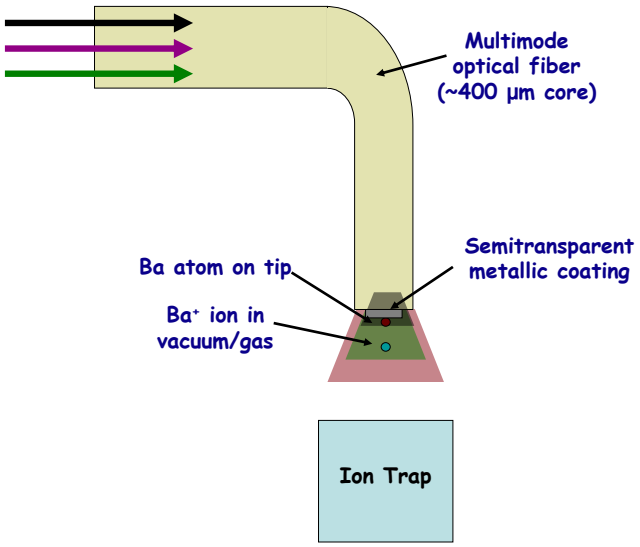

Figure 2.7: Schematic diagram of a possible RIS ion transport probe that makes use of a fiber for laser delivery. The three colored lines indicate the desorption, resonance, and ionization lasers.

that will extract barium from liquid xenon. Eventually, the probe might consist of a metalized fiber for simplicity, and the ion trap used for identification confirmation.

Chapter 3

Resonance Ionization Spectroscopy

Resonance ionization spectroscopy, or RIS, is a multistep photon absorption process in which the final state is the autoionization or ionization continuum of an atom. Resonance ionization is highly selective because it allows only atoms of a given element to be ionized, since the intermediate excited states through which the process proceeds are unique to that element. Furthermore, resonant states with low saturation energies can be selected, so that the majority, if not all, of the atoms in the beam path are ionized [44]. This implies that sensitivity in the single-ion level is possible by saturating the RIS process and detecting the ensuing ions with a gas proportional counter or an electron multiplier [45].

3.1 RIS Processes

Figure 3.1 shows a schematic diagram for the most elementary RIS process, in which a pulsed laser beam produces photons of the right energy to excite an atom from its ground state 1 to an excited level 2. Another photon of the same energy can ionize state 2 into the continuum c. If each atom of a selected species which was originally in its ground state is converted to a positive ion and a free electron during the duration of a laser pulse, then the process is said to be saturated. Two conditions have to be

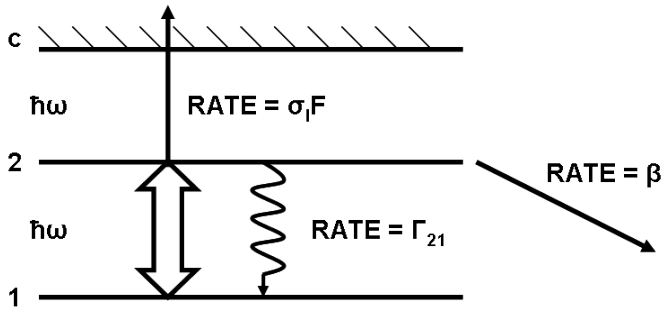

Figure 3.1: Schematic for the most elementary RIS process. An atom in the ground state 1 can be ionized by first exciting to another bound state 2.

satisfied for saturation to occur. First, the photon fluence (photons per unit beam area) has to be large enough. Second, the photon flux (photons per cm^2 per second) has to be larger than the rate β at which the intermediate state is destroyed by possible competing processes.

The rate equation formulation was used by Hurst *et al* in a review of their seminal work [45] to quantitatively demonstrate the necessary conditions for saturating the RIS process. Let $\sigma_a(\nu)$ be the cross section for photon absorption from state 1 to state 2, let $\sigma_s(\nu)$ be the stimulated emission cross section from state 2 to state 1, and let $\sigma_I(\nu_0)$ be the cross section for photoionization of state 2 at the central frequency ν_0. A laser beam is characterized by intensity I where $I(\nu)(\nu)d\nu$ equals the number of photons per cm^2 per second and in the frequency interval ν and $\nu + d\nu$, where, for simplicity, a Gaussian line shape is used:

$$I(\nu) = \frac{F}{\sqrt{2\pi\Delta\nu^2}} e^{-\frac{(\nu-\nu_0)^2}{2\Delta\nu^2}} \tag{3.1}$$

In Eq.(3.1), F is the photon flux and $\Delta\nu$ is the laser linewidth. The rate of change of levels 1 and 2 is given by

$$\frac{dn_1}{dt} = -n_1 \int d\nu\sigma_a(\nu)I(\nu) + \Gamma_{21}n_2 + n_2 \int d\nu\sigma_s(\nu)I(\nu) \tag{3.2a}$$

$$\frac{dn_2}{dt} = n_1 \int d\nu\sigma_a(\nu)I(\nu) - n_2 \int d\nu\sigma_s(\nu)I(\nu) - \Gamma_{21}n_2 - \beta n_2 - \sigma_I F n_2 \tag{3.2b}$$

where Γ_{21} is the spontaneous emission rate, while the rate of photoionization into the continuum c is given by

$$\frac{dn_I}{dt} = \sigma_I F n_2 \tag{3.2c}$$

Using Einstein's detailed balancing and the fact that both $\sigma_a(\nu)$ and $\sigma_s(\nu)$ are narrow compared to $\Delta\nu$,

$$\int d\nu \sigma_a(\nu) I(\nu) = \frac{g_2}{g_1} \frac{\lambda^2 \Gamma_{21} F}{8\sqrt{2}\pi^{3/2}\Delta\nu} \equiv \bar{\sigma}_a F = \frac{g_2}{g_1}\bar{\sigma}_s F \tag{3.3a}$$

$$\int d\nu \sigma_s(\nu) I(\nu) = \bar{\sigma}_s F \tag{3.3b}$$

where g_i is the degeneracy factor for state i, and $\bar{\sigma}_s$ is the average cross section for the phototransition. It is worth nothing that, for a Gaussian or Lorentzian lineshape at line center ν=ν_0,

$$\bar{\sigma}_s = \frac{\lambda^2 \Gamma_{21}}{4\pi^2 \Delta\nu_{laser}} \tag{3.4}$$

where $\Delta\nu_{laser}$ is the FWHM linewidth of the laser. Using these relations, Eqs. (3.2a) and (3.2b) can be solved to obtain n_I, :

$$n_2 = \frac{\bar{\sigma}_a F n_1(0)}{b-a}(e^{-at} - e^{-bt}) \tag{3.5}$$

$$n_1 = (\sigma_I F)\frac{\bar{\sigma}_a F n_1(0)}{b-a}\left|\frac{1}{a}(1-e^{-at}) - \frac{1}{b}(1-e^{-bt})\right| \tag{3.6}$$

where $n_1(0)$ is the initial ground-state population and

$$a = \frac{x_2}{2} - \sqrt{\left(\frac{x_2}{2}\right)^2 - x_1^2} \qquad\qquad b = \frac{x_2}{2} + \sqrt{\left(\frac{x_2}{2}\right)^2 - x_1^2}$$

with

$$x_1^2 = \bar{\sigma}_a F(\beta + \sigma_I F) \qquad x_2 = \Gamma_{21} + \beta + (\bar{\sigma}_a + \bar{\sigma}_s + \sigma_I)F$$

In general, if a laser is tuned near the line center and its linewidth is not excessive, both $\bar{\sigma}_a$ and $\bar{\sigma}_s$ are much larger than σ_I. Imposing a condition on the flux,

$$\sigma_I F >> \beta \tag{3.7}$$

$x_2 >> x_1$, and $b >> a$. Equation (3.5) then simplifies, with $\Gamma_{21} << (\bar{\sigma}_a + \bar{\sigma}_s)F$, to

$$n_2 = \frac{g_2}{g_1 + g_2} n_1(0) e^{-at} \tag{3.8}$$

where the time is restricted so that e^{-bt} can be ignored. The production rate of ions is then

$$\frac{dn_I}{dt} = \frac{g_2}{g_1 + g_2} \sigma_I F n_1(0) \exp\left[-\frac{g_2}{g_1 + g_2} \sigma_I F t \right] \tag{3.9}$$

Integrating over the length τ of the laser pulse gives

$$n_I = n_I(0) \left[1 - \exp\left(-\frac{g_2}{g_1 + g_2} \sigma_I F \tau \right) \right] \tag{3.10}$$

If a fluence condition is imposed, such as

$$\frac{g_2}{g_1 + g_2} \phi \sigma_I >> 1 \tag{3.11}$$

where ϕ is the fluence, then $n_I = n_1(0)$ and complete ionization is achieved. In order for the RIS process process to be saturated, both the flux condition [Eq. (3.7)] and the fluence condition [Eq. (3.11)] must be met.

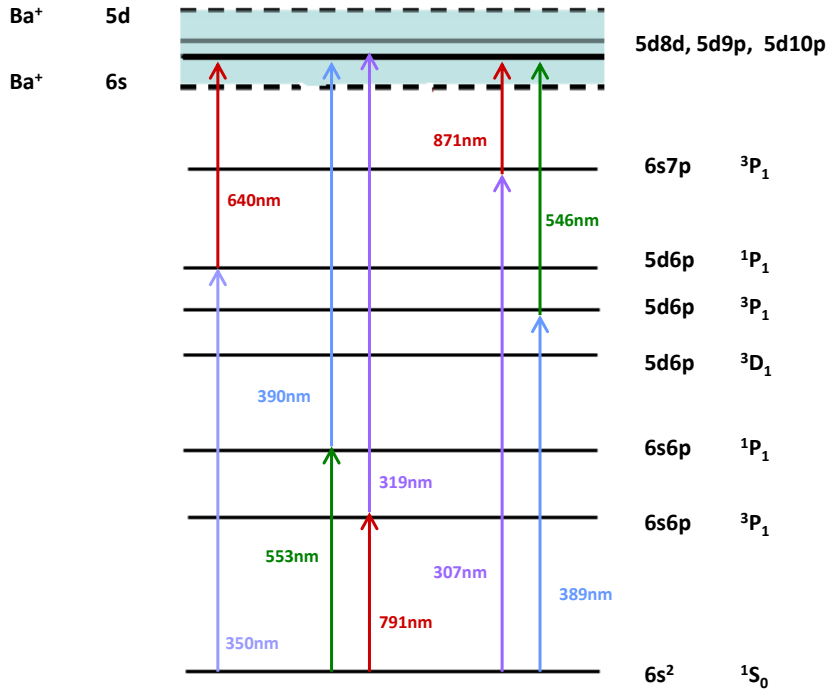

Figure 3.2: Simplified electron configuration of barium, showing transitions that could be used in a RIS scheme.

3.2 RIS Scheme for Barium Tagging in EXO

Though many possible atomic levels could be used for the resonance ionization of barium (see Fig. 3.2), the work presented here makes use of excitation from the $6s^2$ $^1S_0$ ground state to the 6s6p $^1P_1$ excited state by absorption of a single photon at 553.5 nm. Ionization into the autoionized (see below) state 5d8d $^1P_1$ in the continuum between the first and second ionization thresholds is achieved by absorption of a photon at 389.7 nm. This particular sequence is selected because excitation to the 6s6p $^1P_1$ state is both parity and spin allowed and provides access to an autoionized state, thus requiring low energies to saturate, and because the transitions can be reached with relatively cheap dye lasers.

3.2.1 Electronic structure of barium

The ground state electron configuration of barium is [Xe]$6s^2$, making it a quasi two-electron atom. The simultaneous excitation of the two electrons in its valance shell results in a rich and complex electronic structure:

Bound States

Even in the presence of internal excitations, bound states in barium are part of Rydberg series with

$$E_{(nl)} = E_{(\infty)} - \frac{R_M Z^2}{(n-\mu_l)^2} \tag{3.12}$$

that converge to a series limit (ionization threshold) E_∞, where n is the principal quantum number, R_M is the Rydberg constant for the species of mass M, Z is the nuclear charge, and μ_l is the quantum defect that accounts for penetration of inner core electrons.

Furthermore, spin-orbit (LS) coupling causes bound states to split with

$$\Delta E = \frac{\beta}{2}(j(j+1) - l(l+1) - s(s+1)) \tag{3.13}$$

where

$$\beta = \frac{-\mu_B}{m_e e c^2} \left\langle \frac{1}{r} \frac{\partial U(r)}{\partial r} \right\rangle$$

and overcomes the ΔS=0 selection rule so that some bound states are not pure. For example, the 6s6p ^{1}P$_1$ state has significant mixing with the ^{3}P$_1$ state [46]. One should note, however, that the polarization of the lasers used to populate and photoionize these states determines the M_J levels which may be actually populated in a given transition [47].

Autoionized States

Multi-electron systems exhibit structure embedded in the continuum. These states, called autoionizing resonances, are neither purely discrete nor continuous. They arise from simultaneous excitation of both valence electrons. Autoionization is, in essence, an interchannel coupling effect in which an excitation channel contains both a set of

Rydberg states converging on an ionization threshold and the adjoining continuum.

The description of autoionization states using perturbation theory was first done by Fano in 1961 [4]. By this formulation, one can write a wavefunction of energy E consisting of a superposition of a discrete bound state $|\varphi\rangle$ and a continuous state $|\varepsilon\rangle$,

$$|E\rangle = \alpha_\varphi|\varphi\rangle + \int |\varepsilon\rangle b(\varepsilon) d_\varepsilon \tag{3.14}$$

The unperturbed states φ and ε are eigenstates of the unperturbed Hamiltonian H_o so that

$$\begin{pmatrix} H_{\varphi\varphi} & 0 \\ 0 & H_{\epsilon\epsilon} \end{pmatrix} \begin{pmatrix} |\varphi\rangle \\ |\varepsilon\rangle \end{pmatrix} = \begin{pmatrix} E_\varphi|\varphi\rangle \\ \varepsilon|\varepsilon\rangle \end{pmatrix} \tag{3.15}$$

To couple the discrete and continuous channels, an off-diagonal perturbation V is introduced so that the total Hamiltonian is $H{=}H_\mathrm{o}{+}V$.

The corresponding equation for the perturbed system is then

$$\begin{pmatrix} H_{\varphi\varphi} & V_{\varphi\varepsilon} \\ V_{\varepsilon\varphi} & H_{\varepsilon\varepsilon} \end{pmatrix} \begin{pmatrix} \alpha_\varphi|\varphi\rangle \\ \int |\varepsilon\rangle b(\varepsilon) d_\varepsilon \end{pmatrix} = E \begin{pmatrix} \alpha_\varphi|\varphi\rangle \\ \int |\varepsilon\rangle b(\varepsilon) d_\varepsilon \end{pmatrix} \tag{3.16}$$

Taking into consideration that H is Hermitian so that $V_{\varphi\varepsilon} = V^*_{\varepsilon\varphi}$, and that there is only one bound state, a pair of coupled equations can be obtained from Eq. (3.16):

$$\begin{aligned} E_\varphi\alpha_\varphi + \int V^*_\epsilon b_\epsilon d\epsilon &= E\alpha_\varphi \\ V_\epsilon\alpha_\varphi + \epsilon b_\epsilon &= E b_\epsilon \end{aligned} \tag{3.17}$$

Solving the second equation for b_ε, the following is obtained:

$$b_\varepsilon = \frac{V_\varepsilon \alpha_\varphi}{E - \varepsilon} \tag{3.18}$$

A function $\mathcal{Z}(E)$ can be defined such that

$$(E-\varepsilon)^{-1} = \frac{1}{E-\varepsilon} + \mathcal{Z}(E)\delta(E-\varepsilon) \tag{3.19}$$

where one takes the principal part of any integral over $1/(E-\varepsilon)$ and the function $\mathcal{Z}(E)$ is defined by the details of the problem. Substituting for b_ε in the first of the two equations (3.17), one finds that

$$E_\varphi \alpha_\varphi + \mathcal{P}\left\{\int \frac{V_\varepsilon^* \alpha_\varphi V_\varepsilon}{E-\varepsilon} d\varepsilon\right\} + \alpha_\varphi \mathcal{Z}(E)|V_\varepsilon|^2 = E\alpha_\varphi \tag{3.20}$$

Defining

$$F(E) \equiv \mathcal{P}\left\{\int \frac{|V_\varepsilon|^2}{E-\varepsilon} d\varepsilon\right\} \tag{3.21}$$

where $\mathcal{P}$ denotes the principal part of the integral, $\mathcal{Z}(E)$ can be solved for to obtain

$$\mathcal{Z}(E) = \frac{E - E_\varphi - F(E)}{|V_\varepsilon|^2} \tag{3.22}$$

The perturbed function must be normalized in order to determine the coefficient α_φ, which has factored out of the equations. Thus,

$$\langle \tilde{E}|E\rangle = \alpha_\varphi^*(\tilde{E})\alpha_\varphi(E) + \int b_\varepsilon^*(\tilde{E}) b_\varepsilon(E) d\varepsilon = \delta(\tilde{E}-E) \tag{3.23}$$

Substituting for b_ε one has

$$\alpha_\varphi^*(\tilde{E})\left[1 + \int d\varepsilon V_\varepsilon^* \left\{\frac{1}{\tilde{E}-\varepsilon} + \mathcal{Z}(\tilde{E})\delta(\tilde{E}-\varepsilon)\right\} V_\varepsilon \times \left\{\frac{1}{E-\varepsilon} + \mathcal{Z}(E)\delta(E-\varepsilon)\right\}\right]\alpha_\varphi(E) = \delta(\tilde{E}-E) \tag{3.24}$$

The integral can be solved, as discussed in [4], to obtain

$$|\alpha_\varphi(E)|^2 = \frac{|V_\varepsilon|^2}{[E - E_\varphi - F(E)]^2 + \pi^2 |V_\varepsilon|^4} \tag{3.25}$$

which shows that the discrete state E_φ is diluted into a continuous band of energy

states with a half-width $\Gamma/2 \equiv \pi|V_\varepsilon|^2$, about a mean position $E_0 = E_\varphi + F(E)$. The dilution of the energy level to form a resonance is symmetrical and has a Lorentzian shape which can be expressed as

$$|\alpha_\varphi(E)|^2 = \frac{1}{\pi}\frac{\Gamma/2}{(E-E_0)^2 + (\Gamma/2)^2} \tag{3.26}$$

This describes the dilution by mixing of the discrete bound state $|\varphi\rangle$ into the continuum state $|\varepsilon\rangle$, but in practice one must consider not energy levels but rather the transitions from an initial state $|i\rangle$ to the mixed state $|E\rangle$ described by (3.14).

The dipole operator $\tilde{D}$ can induce transitions ending both in the mixed state and in the continuum. The ratio of these probabilities is a measure of the modulation produced by resonance in a continuum cross section, and can be defined by

$$R = \frac{|\langle E|\tilde{D}|i\rangle|^2}{|\langle\varepsilon|\tilde{D}|i\rangle|^2} \tag{3.27}$$

Substituting for $|E\rangle$,

$$R = \frac{|\alpha_\varphi\langle\varphi|\tilde{D}|i\rangle + \int b_\varepsilon d\varepsilon\langle\varepsilon|\tilde{D}|i\rangle|^2}{|\langle\varepsilon|\tilde{D}|i\rangle|^2} \tag{3.28}$$

Using (3.18) and (3.19),

$$R = \frac{|\alpha_\varphi|^2}{|\langle\varepsilon|\tilde{D}|i\rangle|^2}\left|\langle\varphi|\tilde{D}|i\rangle + \mathcal{P}\left\{\int V_\varepsilon \frac{\langle\varepsilon|\tilde{D}|i\rangle}{E-\varepsilon}d\varepsilon\right\} + V_\varepsilon \mathcal{Z}(E)\langle\varepsilon|\tilde{D}|i\rangle\right|^2 \tag{3.29}$$

If the shifted state $|\Phi\rangle$ is defined as

$$|\Phi\rangle = |\varphi\rangle + \mathcal{P}\left\{\int \frac{V_\varepsilon}{E-\varepsilon}d\varepsilon|\varepsilon\rangle\right\} \tag{3.30}$$

then

$$R = \frac{|\alpha_\varphi|^2}{\langle\varepsilon|\tilde{D}|i\rangle^2}\left|\langle\Phi|\tilde{D}|i\rangle + V_\varepsilon \mathcal{Z}(E)\langle\varepsilon|\tilde{D}|i\rangle\right|^2 \tag{3.31}$$

It is interesting to note that (Eq. 3.22) $|V_\varepsilon|^2 \mathcal{Z}(E) = E - E_0$ is simply the detuning from the resonance energy. Defining a new energy variable

$$\epsilon \equiv \frac{2(E - E_0)}{\Gamma}$$

and a parameter

$$q \equiv \frac{\langle \Phi | \tilde{D} | i \rangle}{\pi V_\varepsilon \langle \varepsilon | \tilde{D} | i \rangle}$$

One finds that

$$|\alpha_\varphi|^2 = \frac{1}{\pi^2 V_\varepsilon^2 (\epsilon^2 + 1)}$$

and

$$R = |\alpha_\varphi|^2 \ |\pi V_\varepsilon q + \pi V_\varepsilon \epsilon|^2$$

And so

$$R = \frac{(q + \epsilon)^2}{1 + \epsilon^2} \tag{3.32}$$

which is known as the Fano Lineshape Formula. One can write this formula in terms of the detuning $E - E_0$ and linewidth Γ

$$R = \frac{(q\Gamma/2 + E - E_0)^2}{(E - E_0)^2 + (\Gamma/2)^2} \tag{3.33}$$

If one plots the lineshape R as a function of the energy parameter ϵ for various values of the Fano parameter q (Figure 3.3), one can see that this lineshape is asymmetrical. When $q = 0$, the lineshape becomes Lorentzian.

3.2.2 Saturation energies

As described in § 3.1, the cross section for the resonant transition is given by

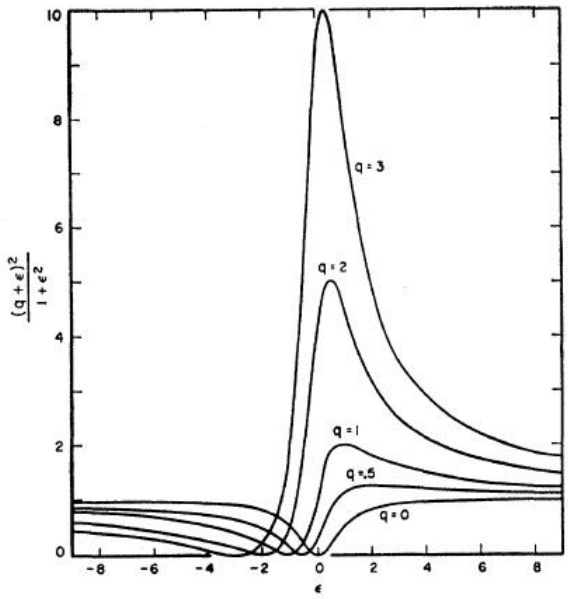

Figure 3.3: Natural lineshapes for different values of q (reverse the abscissas for negative q). From [4].

$$\sigma_{resonance} = \frac{g_2}{g_1}\frac{\lambda^2}{4\pi^2}\frac{\Gamma_{21}}{\Delta\nu_{laser}}$$

For barium, the cross section of the resonant $6s^2\ {}^1S_0 \rightarrow 6s6p\ {}^1P_1$ transition with our experimental setup, described in detail in Chapter 4, is 2.36x10^{-11} cm^2 (see Table 3.1). The cross section of the autoionization transition $6s6p\ {}^1P_1 \rightarrow 5d8d\ {}^1P_1$ is 5.50x10^{-16} cm^2 [5, 48].

Constant	Value
g_2	3
g_1	1
λ	5.53x10^{-5} cm
Γ_{21}	1.19x10^8 s^{-1} [49]
$\Delta\nu_{laser}$	1.17 GHz (0.0012 nm)

Table 3.1: Parameters for the cross section of the $6s^2\ {}^1S_0 \rightarrow 6s6p\ {}^1P_1$ transition in barium.

This results in saturation energies of 0.48nJ and 73μJ respectively, given that

$$E_{sat} = (h\nu)\frac{A}{\sigma} \tag{3.34}$$

and that the 553 nm beam is circular with a 2 mm diameter while the 390 nm beam is elliptical with a 5 mm major axis and a 2 mm minor axis.

Saturation energies can be experimentally determined by following Metcalf's [50] treatment of the optical Bloch equations, which describes the total scattering rate γ_p of light from the laser field in the following manner:

$$\gamma_p = \frac{\gamma(I/I_{sat})/2}{1 + I/I_{sat} + 2(\delta/\gamma)^2} \tag{3.35}$$

where γ is the spontaneous emission rate, I is the intensity, and δ is the laser detuning from the atomic resonance frequency. For the experimental setup described in Chapter 4, Eq. (3.35) can be used to obtain the saturation energies of the 553 nm and 390 nm transitions if one measures the average ion count rate as a function of each laser's energy. In this case, $\delta \approx 0$ since the lasers are at the resonance frequency. Results will be shown in the next chapter.

3.2.3 Linewidth broadening

The ability to selectively ionize using RIS is due, in part, to populating and exciting narrow atomic transitions. However, experimental conditions lead to the broadening of these linewidths. For the experimental setup described in this dissertation, this is mainly due to power broadening and, to a lesser extent, Doppler broadening.

If the laser power is very high so that $I/I_{sat} \gg 1$, then γ_p saturates to $\gamma/2$ and Eq. (3.35) can be written as

$$\gamma_p = \left(\frac{I/I_{sat}}{1 + I/I_{sat}}\right)\left(\frac{\gamma/2}{1 + (2\delta/\gamma')^2}\right) \tag{3.36}$$

where

$$\gamma' = \gamma\sqrt{1 + I/I_{sat}} \tag{3.37}$$

Because of saturation, the linewidth of the transition as experimentally observed is broadened from its natural linewidth γ to its power-broadened value γ'. This is because, for large values of I/I_{sat}, the absorption increases with increasing intensity in the wings of the spectral profile as the center is already saturated.

The danger of power broadening is that the transitions become so broad that states other than the desired ones become populated. The power of the lasers used for RIS has to be carefully controlled so that there is enough power to saturate the atomic transitions (and thus maximize the number of barium atoms ionized) but not so much that power broadening becomes an issue (and thus selectivity is lost).

Linewidths can also be broadened for atoms in thermal motion. In this case, the Doppler shift in the frequency is given by

$$\omega_i = \omega_0 \left(1 - \frac{v_i}{c}\right) \tag{3.38}$$

where ω_0 is the frequency of the atom at rest. As will be discussed in Chapter 6, releasing barium atoms from the surface of a substrate might result in atoms with a Boltzmann distribution of velocities. This distribution, in the direction z of the laser light, is given by

$$P(v_z)dv_z = \sqrt{\frac{m}{2\pi kT}} \exp\left(\frac{-mv_z^2}{2kT}\right) dv_z \tag{3.39}$$

Noting that

$$dv_z = \frac{dv_z}{d\omega_i} d\omega_i = \frac{c}{\omega_0} d\omega_i \tag{3.40}$$

yields the probability distribution of the frequencies:

$$\mathrm{P}(\omega_i)d\omega_i = \sqrt{\frac{mc^2}{2kT\omega_0^2}} \exp\left(-\frac{mc^2(\omega_i - \omega_0)^2}{2kT\omega_0^2}\right) d\omega_i \tag{3.41}$$

This is a Gaussian distribution with a FWHM given by

$$\Delta\omega = \frac{2\omega_0}{\mathrm{c}}\sqrt{2\ln 2\frac{kT}{m}} \tag{3.42}$$

In terms of the wavelength, this is expressed as:

$$\Delta\lambda = \lambda_0\sqrt{\frac{8kT\ln 2}{mc^2}} \tag{3.43}$$

Depending on the temperature of the atoms, this broadening can be very small, smaller than the natural linewidth and so insignificant. In any case, the Doppler broadening can be reduced by counter-propagating the laser beams [51].

Chapter 4

Vapor-Phase Resonance Ionization of Barium

As a first step in the development of a RIS-based ion-transport probe, resonance ionization of barium produced by a neutral barium source is attempted. This allows for a precise characterization of the desired Ba^+ ion signal.

4.1 Theoretical Expectations

Theoretical predictions of states in quasi two-electron atoms have been done both using the Slater-Condon theory and with multichannel quantum defect theory (MQDT) [52]. In quantum defect theory, Rydberg series and the adjoining continuum are regarded as an excitation channel. It follows that MQDT takes into account the perturbation or change in quantum defect along a series that results from coupling between series [53]. In MQDT, the energies and wave functions of bound levels belonging to interacting Rydberg series are expressed in two sets of parameters. One set is formed by the close-coupling eigenchannels of the electron and ion core, while the other set contains the quantum defects of these eigenchannels [54].

For the barium RIS scheme described in Chapter 3, when ionizing through the 6s6p $^1P_1$ resonance, one expects to see a state, or possibly more, of the autoionized 5dnd Rydberg series with J=0,1, and 2 (depending on the polarization of the lasers),

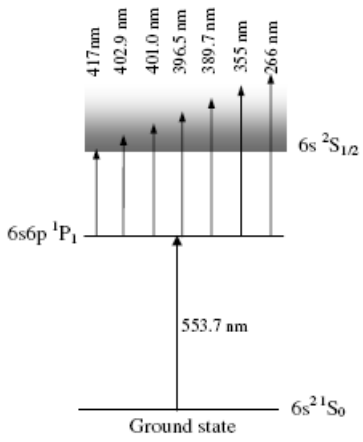

Figure 4.1: Autoionized states reachable from the 6s6p $^1P_1$ excited state of barium. From [5].

converging on the 5d $^2D_{3/2}$ ionization limit [54, 55]. Particularly, the $5d_{5/2}8d$ autoionized state at ∼390 nm and the continuum around the 6s $^2S_{1/2}$ (1^{st}) ionization threshold should be seen (see Fig. 4.1).

Ref. [5] estimates the linewidth of the $5d_{5/2}8d$ autoionized state to be ∼ 0.02 nm. The linewidth of the 6s6p $^1P_1$ state should be 0.0012 nm, limited by the linewidth of the laser employed (see § 3.2.2).

4.2 Experimental Setup

4.2.1 Vacuum system

Operation of the RIS transport probe at the single-ion level, as well as interaction with an ion trap and with the EXO TPC, requires ultra-high vacuum (UHV) compatible materials and techniques in order to minimize impurities. A Kimball Physics 4.50"conflat "spherical cube" is used as a vacuum chamber. Two 4.50"quartz viewports are used for laser entrance and exit. The system is pumped to vacuum with a 30-l/sec turbomolecular pump (TMP) backed by a 10-l/sec dry scroll pump. A custom-made oven bakes the system at ∼ 120 °C, achieving 1×10^{-8} Torr vacuum

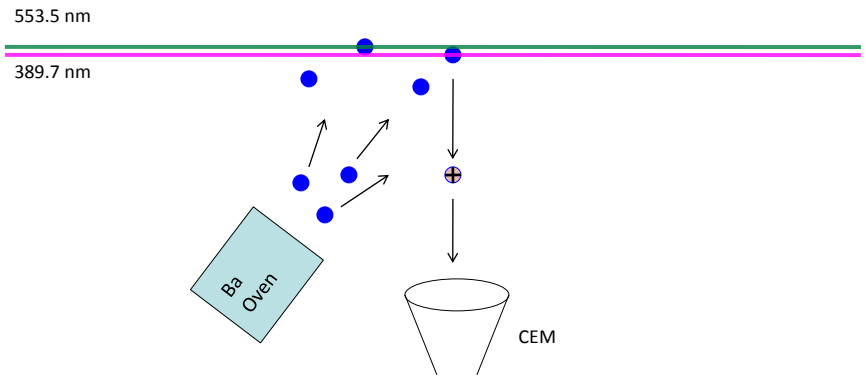

Figure 4.2: A simple schematic diagram that shows how resonance ionization of barium is achieved and detected. A barium oven produces barium atoms which are then resonantly ionized by two laser beams. The resulting barium ions are detected by a CEM.

after one day. A barium oven is used as the source of barium. The oven consists of a barium-getter wire inside a Macor® cylinder closed at one end and pressed against a stainless steel plate with an aperture 1 mm in diameter and 10 mm long at the other end. The barium wire is initially flashed at 4 Amps, which deposits metallic barium onto the walls of the Macor® cylinder. The wire is then run at a constant lower current as a heat source. Neutral barium is thermally released from the walls and exits through the aperture, creating an atomic beam. The vacuum chamber also contains a channel electron multiplier [1] (CEM) used for ion detection. A schematic diagram of this setup is shown in Fig. 4.2.

4.2.2 Spectroscopic laser systems and optics

The 553 nm and 390 nm RIS beams are produced by a pair of Syrah Cobra-Stretch dye lasers pulsed at 10Hz. Green light is generated by a laser[2] containing pyrromethene 580 as a dye[3] dissolved in ethanol and pumped by a frequency-doubled (532 nm)

[1]Model 2403, DeTech, Palmer, MA
[2]Model CSTR-D24, E=18.5 mJ @ 554 nm, Spectra-Physics, Irvine, CA
[3]All dyes obtained from Exciton, Dayton, OH

Q-switched Quanta-Ray INDI Series Nd:YAG laser[4], also from Spectra-Physics. The third harmonic (355 nm) of this same laser is used to pump a mixture of Exalite 389 and Exalite 398 dyes dissolved in p-dioxane in another Cobra-Stretch laser[5] in order to generate UV light.

The 553 nm beam is circularized by a pair of cylindrical lenses with f=150 mm and f=25.4 mm, and collimated with a f=40 cm lens. Its power is adjusted by a half-waveplate and a Glan-Laser calcite polarizer. The power of the 390 nm beam is decreased with another Glan-Laser polarizer and adjusted with ND filters. The two RIS beams are spatially combined with a dichroic filter, and injected into a vacuum chamber.

Though the lasers nominally operate at a repetition rate of 10Hz, the possibility of having a slower 1Hz rep rate was determined to be at times important in understanding the data. For this purpose, a timing apparatus was constructed. This setup utilizes six LeCroy model 222 dual gate generators, a LeCroy model 429A logic fan-in/fan-out module, and a Pragmatic model 2201A high definition arbitrary waveform generator to create and veto lamp and Q-switch triggers to the pump laser. This allows for a tunable rep rate, as well as a tunable delay between the pump laser and another laser used in the desorption experiments described in Chapter 6.

4.2.3 Data acquisition

The data acquisition system (DAQ) utilizes NIM logic to count ions that have been detected by the CEM and meet a certain criteria. The output signal from the Q-switch of the pump laser is used to trigger the acquisition. Every time there is a trigger (at a rate of 1 or 10 Hz, set by the laser timing system), a gate with a certain delay and width is generated using a LeCroy Model 222 gate generator. The delay and width of the gate are chosen to coincide with the expected time-of-flight of the barium ions, and is adjusted once a clear barium signal is detected. The output of this module is fed into a LeCroy Model 365AL coincidence unit. At the same time, the signal from the CEM is passed through an Ortec model 120A fast-timing preamplifier

[4]Model INDI-40, E=200 mJ @ 532 nm, 100 mJ @ 355 nm, 5-8 ns width
[5]Model CSTR-D-3000, E=5.4 mJ @ 390 nm

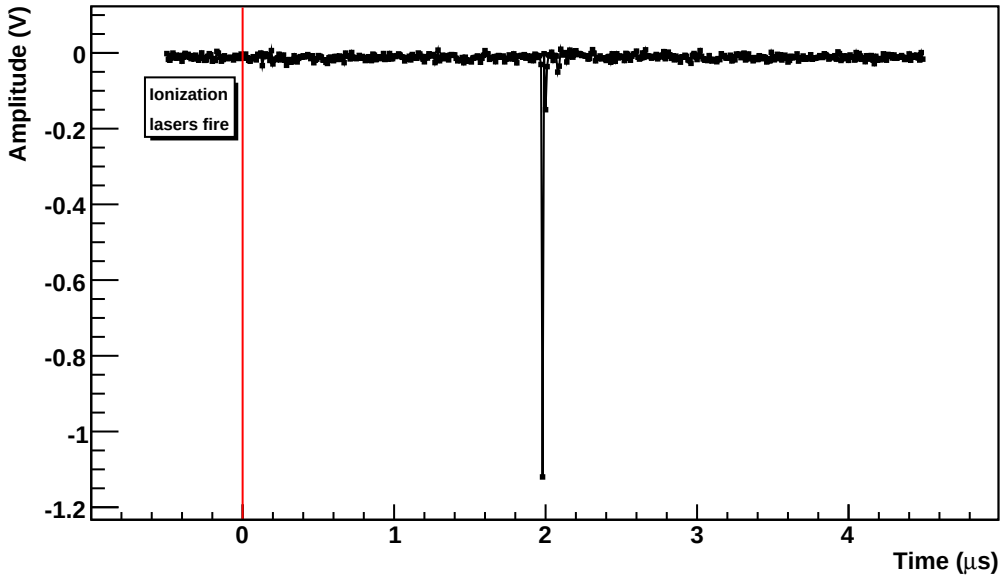

Figure 4.3: Time of flight oscilloscope trace of a candidate resonantly ionized barium ion detected by the CEM. The ionization lasers are fired at t = 0 s, starting the data acquisition. Barium from the neutral beam produced by the oven is immediately ionized, and the ion drifts to the CEM for detection. The time elapsed between ionization and detection corresponds to the time of flight of the ion.

and into another channel of the coincidence unit. An Ortec Model 935 discriminator ensures that only CEM signals above a certain threshold are fed into the coincidence unit. The threshold is set at -0.2 V and is selected so as to maximize signal while minimizing CEM noise. Any coincidences between the gate and the CEM signal are recorded by a Stanford Research Systems Model SR620 counter. The counting of a signal only when in coincidence with a well-chosen gate results in a very low background. Signals from the CEM, laser, and gate are monitored on a Tektronix Model TDS 684B oscilloscope. A candidate data event is shown in Fig. 4.3.

4.3 Results

4.3.1 Evidence for resonance ionization spectroscopy of barium

Evidence for the resonance ionization of barium requires the detection of an ion signal that is correlated to both the barium oven being on and the RIS lasers being on resonance. For data taking conditions, the vacuum inside the chamber is $\sim 1 \times 10^{-8}$ Torr, though pressures as high as 1×10^{-6} Torr still allow for safe operation of the CEM. This high vacuum condition is necessary for a reduced ion background count. The cold-cathode gauge used for pressure measurements needs to be turned off during data taking to reduce the background. The barium oven is turned on, and the RIS beams are steered into the chamber so as to intercept the atomic beam. Laser powers well in excess of saturation (up to 3-5 mJ/pulse) are used initially, and they are turned down once a barium signal is detected. The cone of the CEM is biased at -2000 V. The oscilloscope is used to monitor signals from the CEM as the alignment of the laser beams through the chamber is adjusted.

A typical data set is shown in Figure 4.4. In this case, the green laser is set at 553 nm and 0.99 mJ/pulse, while the UV laser is at 390 nm and 0.35 mJ/pulse and both are at 10Hz. The coincidence gate is set at 1-5 μs, and the discriminator threshold at -0.204V. The barium oven is continuously running. Time 0 seconds indicates the first pump trigger, and ions are immediately seen. For presentation purposes, the number of counts in the CEM is averaged over 5 seconds. After 50 seconds both laser beams are blocked, and the count rate decreases to 0. After 80 seconds, the beams are unblocked and the rate recovers. Between 100-130 seconds the green laser is blocked, and the UV laser is blocked at 175-215 seconds. When either or both of the resonance ionization lasers is blocked, the count rate decreases to zero. The count rate is non-zero otherwise. This strongly suggests that the ion signal is correlated to the RIS lasers.

In order to determine that this ion signal is also correlated to the barium oven, the same operating conditions as described above are employed but the barium oven

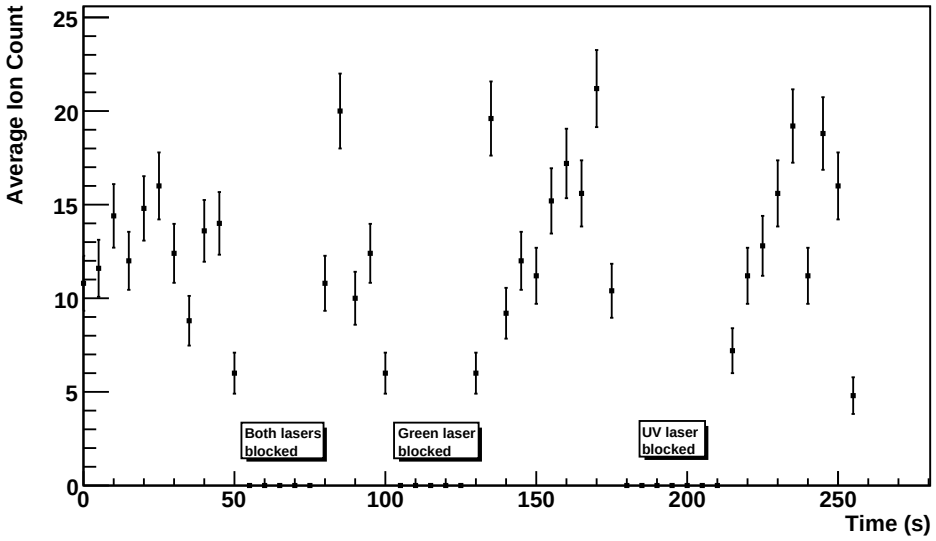

Figure 4.4: Number of ions detected by the CEM, averaged over 5 seconds, for a RIS data run with a gate of 1-5 μs, a green laser energy of 0.99 mJ/pulse, and a UV laser energy of 0.35 mJ/pulse. When either or both of the resonance ionization lasers is blocked, the count rate goes to zero.

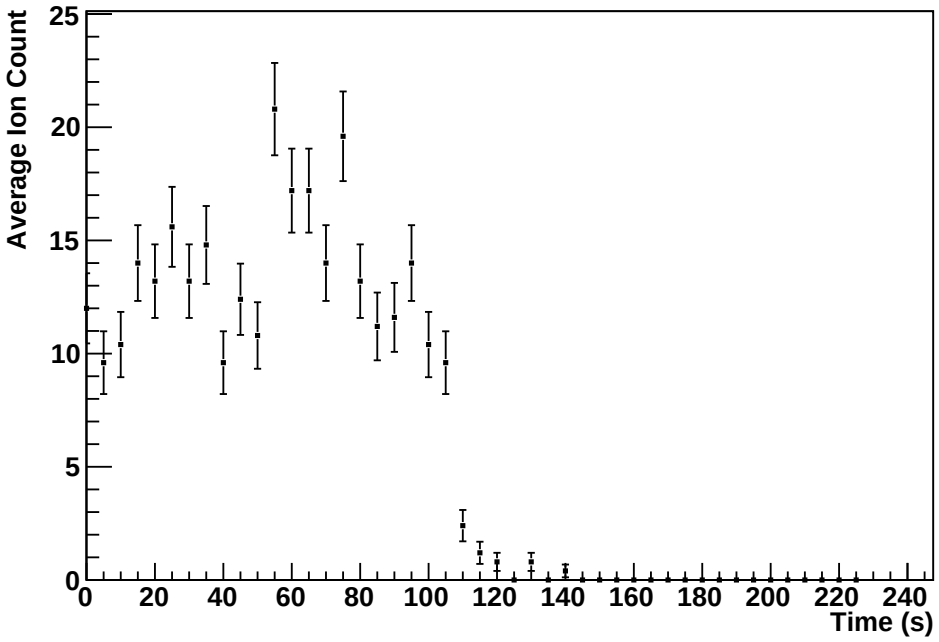

Figure 4.5: Number of ions detected by the CEM, averaged over 5 seconds, for a RIS data run with a gate of 1-5 μs, a green laser energy of 0.99 mJ/pulse, and a UV laser energy of 0.35 mJ/pulse. When the barium oven is turned off at 105 s, the count rate decreases to zero. This decrease is not instantaneous because the barium beam produced by the oven has some thermal inertia.

is turned off halfway through. One expects to see the count rate disappear at this moment, and indeed this is what is observed (Figure 4.5).

4.3.2 Lineshapes of electronic transitions in the vapor phase

An ion signal correlated to both the barium oven and lasers that excite specific transitions presents strong evidence for the resonance ionization of barium. This can be confirmed by transition lineshapes that agree with theoretical expectations and that are corroborated by previous experimental results. For this purpose, wavelength scans both broad (a few nanometers) and narrow (tenths or hundredths of nanometers) are performed around the transitions centered at 553 nm and 390 nm by properly tuning

the lasers. The coincidence gate is set at 1.7-3.2 μs. A High Finesse Model WS6/558 wavemeter is used to monitor the wavelengths.

A wavelength scan of the green laser, centered around 553.55 nm and spanning 0.2 nm in 0.01 nm steps, can be seen in Fig. 4.6, together with a Lorentzian fit. The UV laser has an energy of 0.14 mJ/pulse while the green laser also has an energy close to saturation, $\sim$ 100 nJ/pulse. The lineshape is assumed to be Lorentzian because the contribution from Doppler broadening is thought to be minimal. The fit parameters are shown in Table 4.1. The fit indicates that the resonance transition more accurately occurs at 553.54 nm, with a linewidth of 0.0015 nm which is similar to the linewidth of the laser itself (0.0012 nm).

Parameter	**Value**
Amplitude	1.13±0.04
σ	0.0015±0.0012 nm
μ	553.54±0.01 nm
yOffset	4.19±0.07 counts/sec
χ^2/ndf	46.55/17

Table 4.1: Parameters for a Lorentzian fit of the 553 nm resonant transition in barium.

As discussed in § 4.1, the landscape around the 390 nm transition is more interesting, given the possibility of observing an autoionization state and the continuum that surrounds it. A broad wavelength scan from 387 nm to 397 nm is thus taken. The green laser is set at a wavelength of 553.5 nm with an energy of 2.3 mJ/pulse. The energy of the UV laser is 100 μJ/pulse. The result can be seen in Fig. 4.7. An autoionization state at 389.7 nm is visible. To its right, the structure of the Ba^+ 6s $^2S_{1/2}$ continuum can be seen. If energies well in excess of the saturation energy of this transition are used, the continuum background becomes more pronounced.

A finer scan indicates that the transition occurs at 389.68 nm with a 0.05 nm linewidth. The scan, together with a fit to a Fano lineshape, can be seen in Fig. 4.8. The fit parameters are displayed in Table 4.2.

The lineshape is fit to the Fano formula presented in Eq. (3.33) and including two parameters that account for the portions of the cross section that do and do not

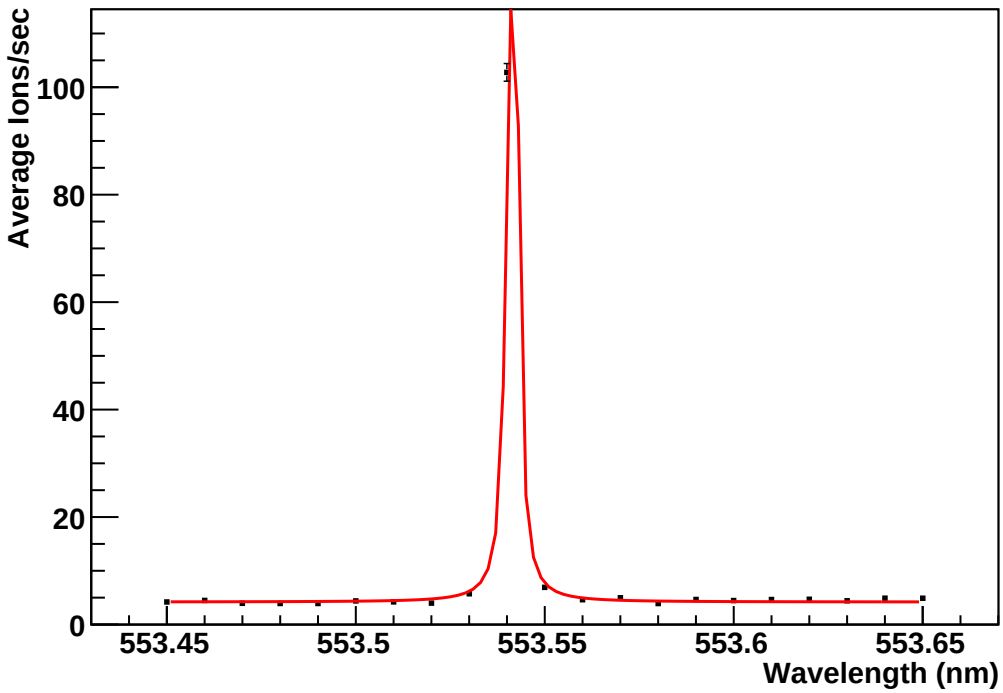

Figure 4.6: Lorentzian fit of the 553 nm resonant transition. The fit indicates the transition to be centered at 553.54 nm with a linewidth of 0.0015 nm.

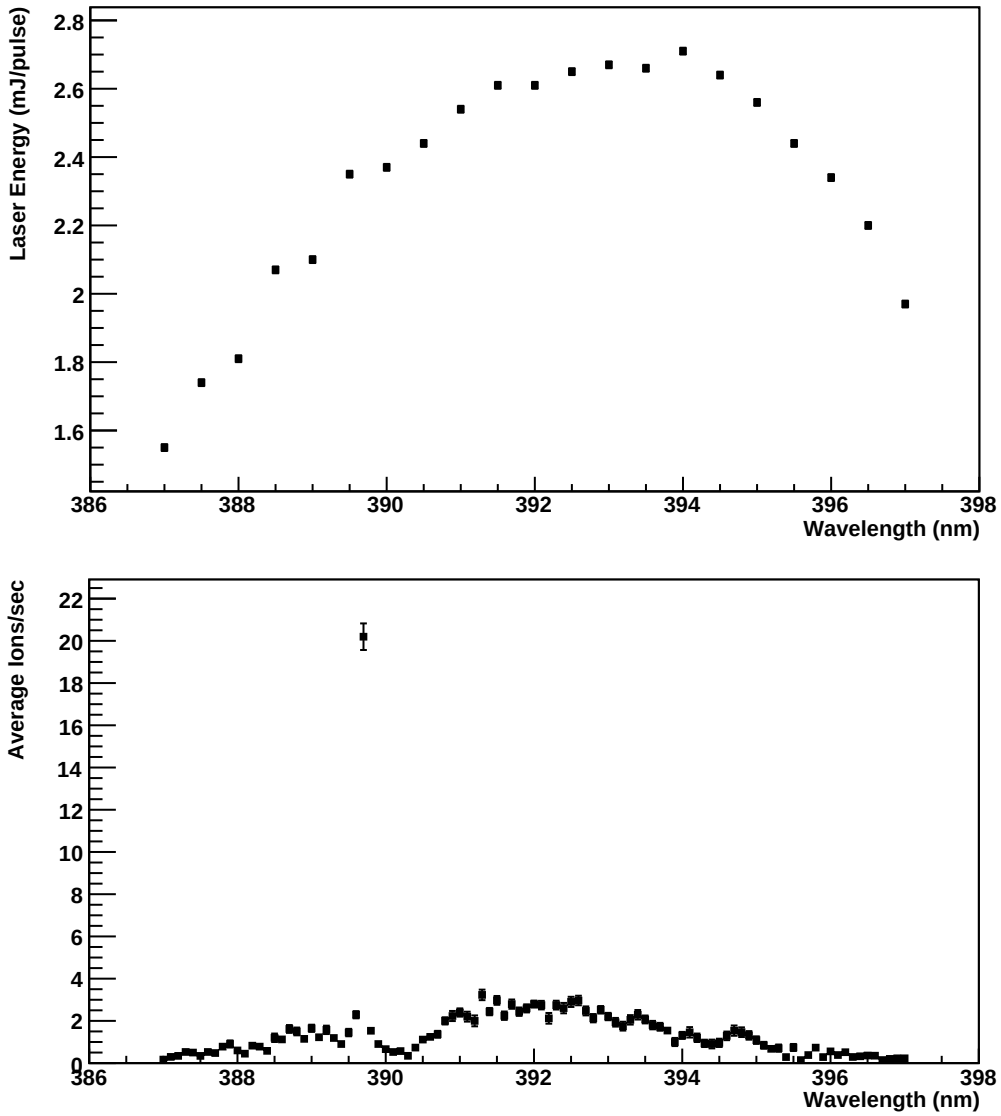

Figure 4.7: (bottom) Broad wavelength scan centered around the ∼390 nm transition with an energy of 100 μJ/pulse. The green laser is set at 553.5 nm and with an energy of 2.3 mJ/pulse. An autoionization state at 389.7 nm, as well as the Ba^+ 6s $^2S_{1/2}$ continuum that surrounds it, can be seen. (top) UV laser energy as a function of laser wavelength, for normalization of the bottom plot.

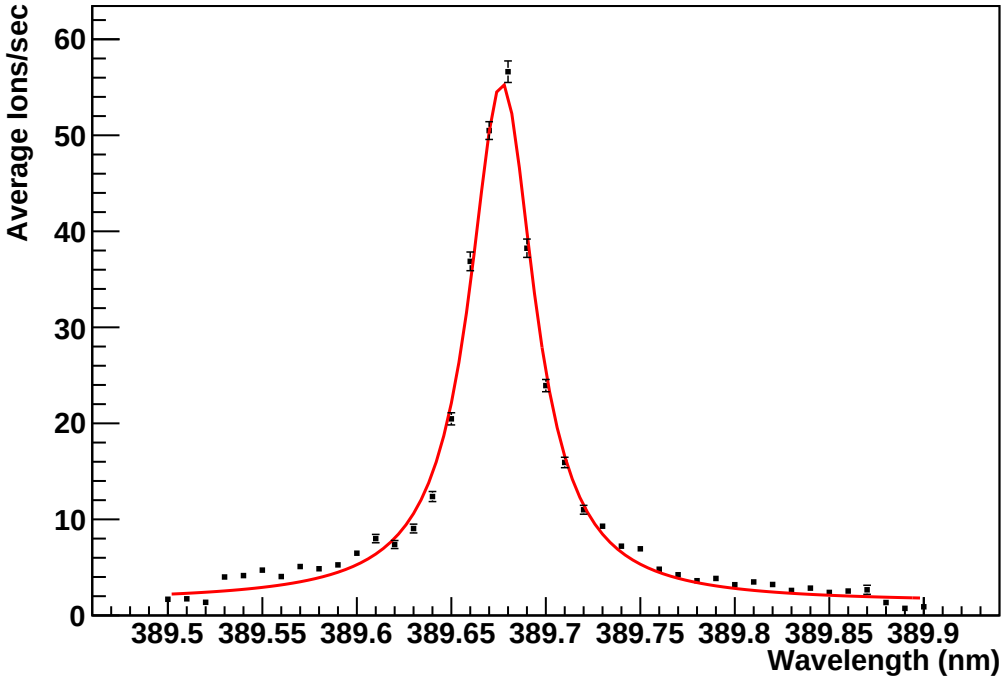

Figure 4.8: Fano fit to the lineshape of the autoionization transition at ∼390 nm.

Parameter	Value
Fano parameter q	-180±70
σ	0.05±0.01 nm
μ	389.68±0.01 nm
Interaction parameter	0.002±0.001
Non-interaction parameter	1.39±0.06
χ^2/ndf	427.2/36

Table 4.2: Parameters for a Fano fit of the ∼390 nm resonant transition in barium.

interact with the discrete autoionizing state [56]. The value of q, as defined in § 3.2.1, reflects the ratio of the transition probabilities to the discrete state Φ and the continuum ε. The rather large value of $|q|$ indicates that ionization occurs by excitation and decay of a discrete autoionizing state, as opposed to direct photoionization to the underlying continuum. The lineshape observed is therefore symmetric and produced on top of the continuum background.

The Fano formula is not applicable only if the autoionization width approaches the separation between successive members in a Rydberg series, if the background continuum is not flat, and if there are other channels for particle broadening [53]. The three conditions apply in this case, but one has to be wary of excess laser power exposing the limitations of the Fano formula, in the sense that power broadening might increase the continuum background and transition linewidth so much that the Fano formula fails to describe the general lineshape of the autoionization resonance well.

4.3.3 Saturation energies of resonant transitions in the vapor phase

As was discussed in Chapter 3, saturation energies can be experimentally determined by using Eq. (3.35),

$$\gamma_p = \frac{\gamma(I/I_{sat})/2}{1 + I/I_{sat} + 2(\delta/\gamma)^2}$$

The green saturation curve (Figure 4.9, top) is obtained by having both lasers at resonance (389.68 nm and 553.54 nm) and scanning the energy of the green laser while keeping the UV laser at constant energy of 1.2 mJ/pulse. The UV saturation curve (Figure 4.9, bottom) is obtained in a similar manner, with the green laser energy constant at 1.47 mJ/pulse. The fit parameters for the curves are shown in Table 4.3.

Parameter	**553.5 nm**	**389.7 nm**
γ (Hz)	388±2	4523±6
I_{sat} (J/pulse)	$(5 \pm 1) \times 10^{-9}$	$(3.9 \pm 0.1) \times 10^{-4}$
χ^2/ndf	171/4	698.4/8

Table 4.3: Fit parameters of the saturation curves for the 553.5 nm and 389.7 nm transitions in barium.

Theoretically predicted values for the green and UV saturation energies, calculated in § 3.2.2, are 0.48 nJ and 73 μJ, respectively. This is about 5-10 times smaller than the experimentally measured ones. This discrepancy can be attributed to uncertainties in the measurements at such low energies arising, in part, from the limitations in sensitivity of the power meter [6] and neutral density filters employed, as well as uncertainties in measuring the beam parameters and not enough data points for a good statistical fit. Furthermore, in measuring the saturation energy of the ∼390 nm resonance, He *et al* [47] found that poor alignment of the optical system lead to hot spots on the laser beam resulting in a poor fit to the data. It is likely that this also played a part here.

[6] Model 818P-015-18, Newport Corporation, Irvine, CA

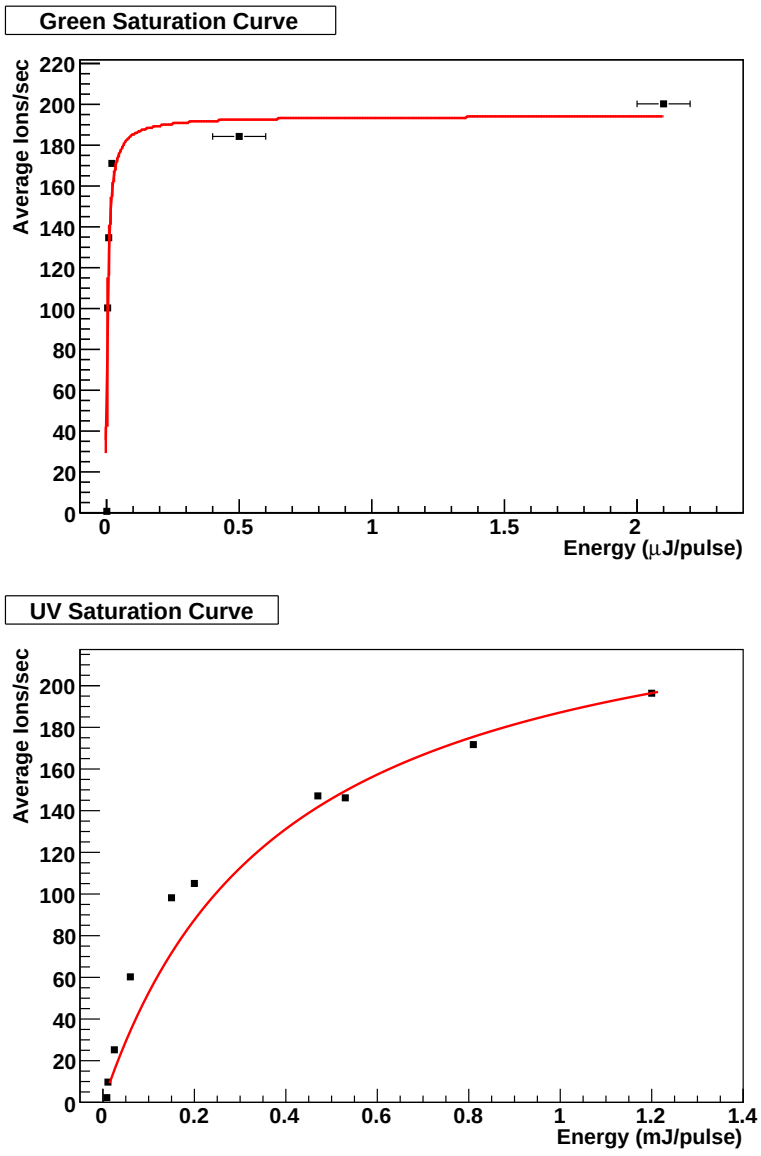

Figure 4.9: Saturation curves for the 553.54 nm (top) and 389.68 nm (bottom) transitions. The black squares indicate experimental data, while the red curves are the fits to Equation (3.35).

Chapter 5

A Radionuclide-Driven Single-Ion Ba Source

The results presented in Chapter 4 provide evidence for the successful resonance ionization of barium. In order to determine the viability of a resonance ionization-based ion transport and detection technology for EXO, the efficiency of this process has to be measured. The tagged Poissonian Ba^+ source described in this chapter was developed for this reason, and its use is described in Chapter 6.

The source presented here makes use of the alpha decay of ^{148}Gd,

$$^{148}_{64}\mathrm{Gd} \rightarrow {}^{144}_{62}\mathrm{Sm} + \alpha \tag{5.1}$$

and the recoiling Sm ($E = 88$ keV) is used to release Ba^+ ions from a BaF_2 layer. ^{148}Gd is a convenient α emitter because its half-life (74.6 y) provides a good compromise between high specific activity and durability. Furthermore, the decay of ^{148}Gd is directly in the ground state of ^{144}Sm, so that no other radioactivity is produced.

A schematic diagram of the source is shown in Fig. 5.1. A few monolayers of Gd are electroplated onto a PIPS® α detector [1], and a thin layer of BaF_2 is then vapor-deposited over the entire detector. For half of the Gd decays, the α particle is detected in the PIPS® detector, providing a tag for the ion emission. At the same

[1] Model PD50 50 mm^2 active area unmounted wafer, Canberra, Meriden,CT.

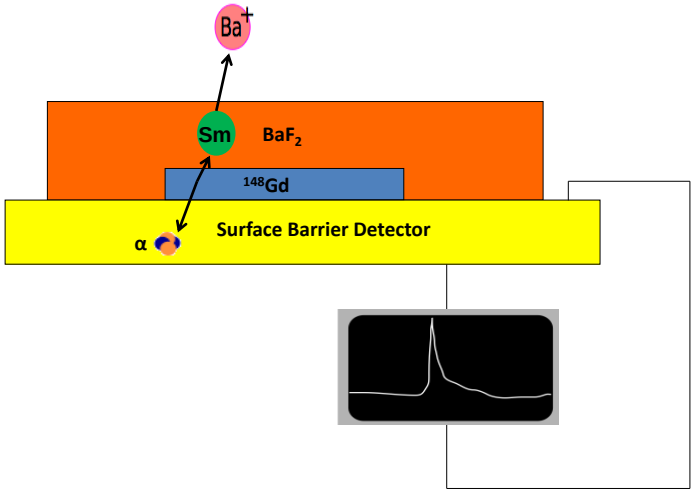

Figure 5.1: Schematic diagram of the radionuclide-driven source. A PIPS® detector is used as the substrate. ^{148}Gd and BaF_2 are deposited on top. After a Gd decay, the alpha particle is detected, providing a tag, while the Sm daughter dislodges Ba^+ from the BaF_2 layer.

time, the recoiling Sm daughter traverses the BaF_2 layer, knocking off Ba^+ ions.

5.1 Source Fabrication

5.1.1 Electroplating

A schematic diagram of the plating setup can be seen in Fig. 5.2. This setup allows for radioactivity to be contained to a small area of the detector. The plating circuit is established by mounting a PIPS® detector on a horizontal support and lowering an anode to a position about 0.5 mm above the center of the detector using a micrometer. The anode consists of a 4 mm-wide slice of a B-doped silicon wafer (resistivity $\approx$ 50 Ωm).

^{148}Gd is obtained in the form of $GdCl_3$ in HCl aqueous solution. Natural Gd is present as carrier in the solution in the approximate ratio [57] ^{nat}Gd:^{148}Gd=1:6.6$\times 10^{-4}$.

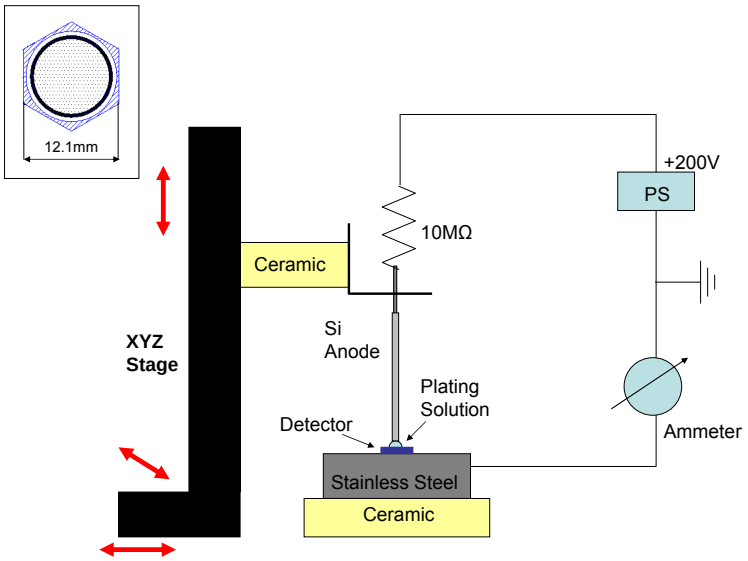

Figure 5.2: Schematic diagram of the radioactive Gd plating setup. The micrometers allow for an accurate positioning of the anode $\simeq$ 0.5 mm above the center of the detector being plated. A drawing of the Canberra PIPS® detector used is provided in the inset.

Gd electroplating works best from gadolinium nitrate[58] in an isopropanol (IPA) solution. The chloride is thus transformed into a nitrate:

$$GdCl_{3(aq)} + 3HNO_{3(aq)} \rightarrow Gd(NO_3)_{3(aq)} + 3HCl_{(aq)} \quad (5.2)$$

The reaction is achieved from 500μL (0.1μCi) of $^{148}GdCl_3$ and a total of 1500μL of 1M HNO_3 [2] delivered in 500μL increments. The $^{148}Gd(NO_3)_3$ is then dissolved in 500μL of IPA [3]. 25μL of this plating solution are calculated to have an activity of 185 Bq. A measurement of the activity, performed by dissolving one 25μL batch in a liquid scintillation counter [4], confirms a carry-over efficiency of $\sim$100%. Since the $Gd(NO_3)_3$ concentration is extremely low, a drop of 0.05M HNO_3 is added in 10L of the IPA in order to increase the conductivity of the plating solution to an acceptable level.

A $\sim$ 5 μL drop of the plating solution is deposited between the anode and the detector, which serves as the cathode in the circuit. The drop remains in place because of surface tension. A 200 V potential is then applied to the circuit via a 10 MΩ current-limiting resistor, establishing a current that is measured to 18 μA. More 5 μL batches of the plating solution are added, as the solvent evaporates, for a total of 25 to 50 μL. Pure IPA aliquots are also added to counter evaporation. The solution is plated for 15 min. Because of the non-radioactive Gd carrier, a source of $\simeq$200 Bq activity, obtained from 25μL plating solution, roughly covers a surface of 8×10^{-2} cm^2 with $\sim$10 monolayers of Gd.

5.1.2 Vapor deposition

Coating with BaF_2 is achieved by vapor deposition, as this technique provides a uniform layer over the entire front surface of the detector and does not chemically interfere with the radionuclide. Vapor deposition is done under 10^{-6} Torr vacuum. A tantalum boat containing a small scintillation-grade BaF_2 crystal [5] is resistively

[2] TraceMetal grade, Fisher Chemical, Pittsburgh, PA
[3] LC-MS Chromasolv® >99.9% grade, Sigma-Aldrich, St. Louis, MO
[4] Measurement performed by the Stanford Health Physics Department, Stanford, CA
[5] Produced by the Beijing Glass Research Institute, Beijing, China

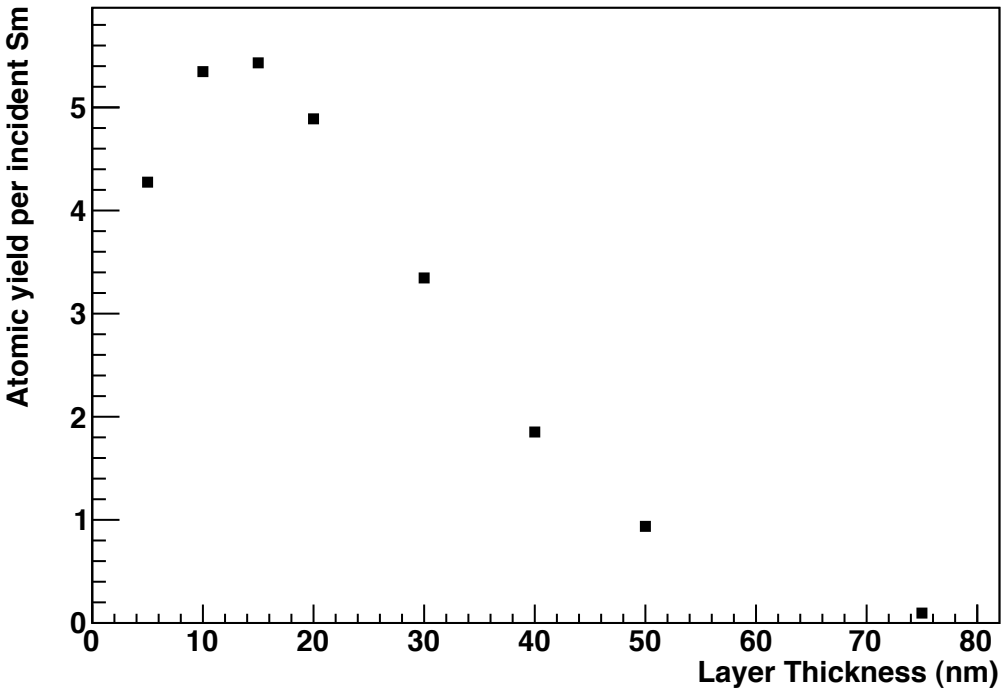

Figure 5.3: Yield for Ba atoms as a function of layer thicknesses, as calculated by a SRIM simulation.

heated with 80 Amps, and the thickness of the deposited layer is monitored by a microbalance located next to the source being plated.

BaF_2 is chosen as the chemical species containing Ba because of its relatively good stability in air [59] and the fact that the other atomic species, fluorine, has a mass that is very different from that of Ba. The optimal layer thickness is estimated using the SRIM [6] [60] simulation package with full damage cascades simulation. Fig. 5.3 shows the predicted Ba yields as a function of thickness. Based on this yield, a thickness of 10-20 nm is optimal.

[6] The Stopping and Range of Ions in Matter

5.1.3 α spectroscopy

Fabrication of the source on the surface of an α detector allows for tagging of the Gd decay, which in turn allows for determination of the number of Ba^+ ions produced and thus RIS efficiency measurements. It is important, then, to make sure that the source fabrication process does not inhibit the detector's ability to tag α decays. This is verified by "self-counting" with the source-substrate detector.

Typical spectra, recorded with a 50 V bias and 2 μs shaping time, are shown in Fig. 5.4. The spectrum from the single 3182.7 keV α emitted by the ^{148}Gd plated on the detector shows (Fig. 5.4(a)) a resolution of $\sim$ 60 keV FWHM. This is worse than 14 keV FWHM stated by the manufacturer, but understandable given the electroplating process the detector has undergone. The spectrum after BaF_2 deposition is substantially broader ($\sim$ 170 keV FWHM, see Fig.Fig. 5.4(b)), presumably due to further deterioration of the detector. The detector is, however, still functional and adequate to tag the decay and subsequent Ba^+ emission.

5.2 Source Characterization

Source emittance is characterized using time-of-flight mass spectrometry.

5.2.1 Experimental setup

A 6" Conflat nipple is used as a vacuum chamber. Inside there is a simple time-of-flight spectrometer comprising two sets of three-electrode lenses separated by a drift region in the center, with an overall $\simeq$ 17 cm length. The spectrometer is designed inhouse and components are machined by the Stanford University Physics Machine Shop. The spectrometer transports ions emitted by the source, mounted on one end with a specially-designed holder, to a CEM mounted at the other end for detection. The electrodes allow for independent adjustment of the electric field at the surface of the source and of the ion impact energy on the CEM. The chamber is pumped to $\sim 10^{-8}$ Torr vacuum by a 30-l/sec TMP backed by a 10-l/sec dry scroll pump. The "start" signal for the time-of-flight measurement is provided by the PIPS® detector

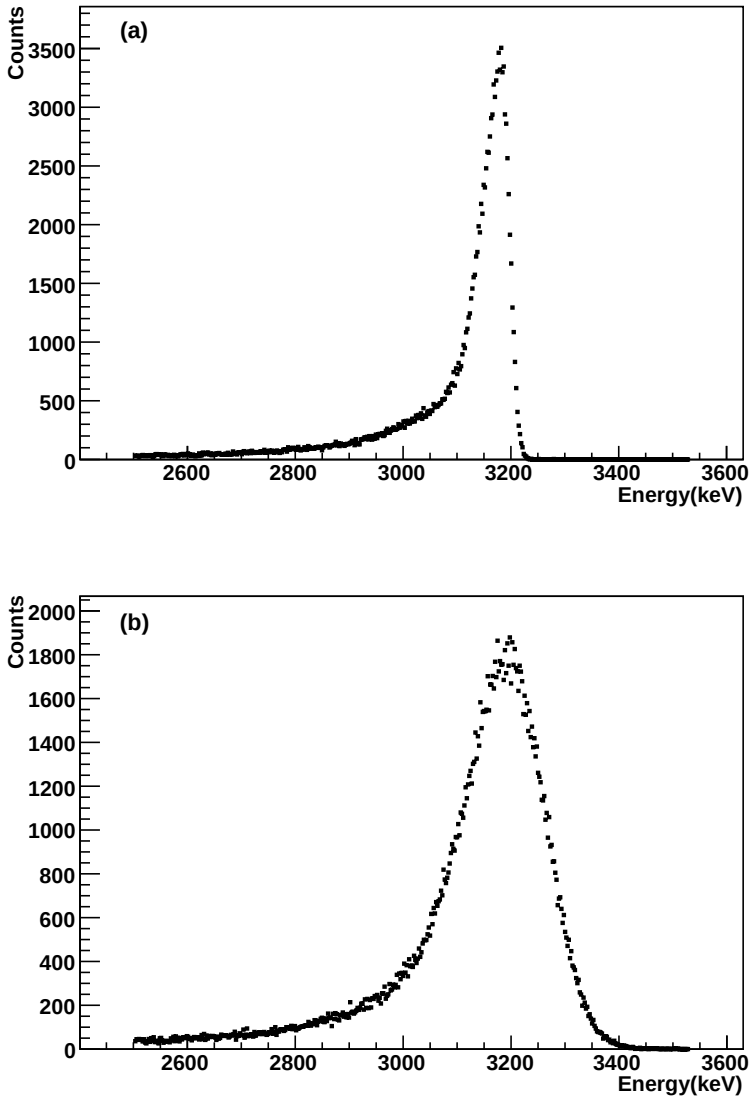

Figure 5.4: ^{148}Gd "self-counted" α spectra. Panel (a) shows the spectrum of the ^{148}Gd layer only. The FWHM energy resolution is ∼60 keV. Panel (b) shows the spectrum after 40 nm of BaF_2 are deposited over the source. The FWHM energy resolution is in this case ∼170 keV.

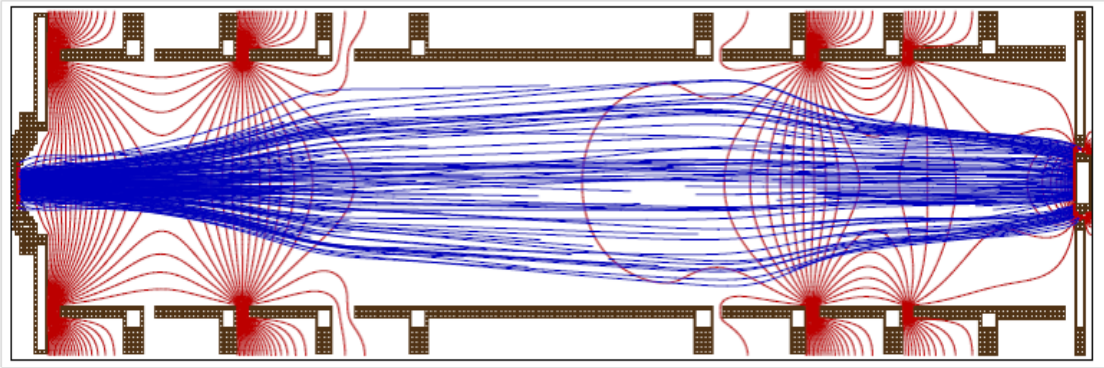

Figure 5.5: SIMION simulations for ions leaving the source (shown on the left) with a field $E_{\text{source}} = 550$ V/cm and having a CEM (shown on the right) impact energy $K = 2800$ eV. The transport efficiency is 85%. Ion trajectories are shown in blue and potentials in red. Courtesy of K. Twelker.

on which the source is built and the "stop" is provided by the CEM pulse. A 45 V bias for the PIPS® detector is provided by a battery, so that the entire source can be floated to high voltage as required by the spectrometer. Signals from both the source and the CEM are digitized with flash ADCs (FADCs) at 250 MS/s. While a fast preamplifier is used for the CEM pulse, the signal from the source is fed into an Ortec model 142 preamplifier followed by a model 474 timing filter amplifier (TFA) with 100 ns shaping. Timing thresholds are applied offline.

A schematic diagram of the time-of-flight spectrometer showing SIMION-calculated ion trajectories (blue) and potentials (red) can be seen in Fig. 5.5.

5.2.2 Ion emission

A typical time-of-flight spectrum obtained for an electric field at the surface of the source $E_{\text{source}} = 550$ V/cm and an ion impact energy $K = 2800$ eV is shown in Fig. 5.6. The prominent peak at 4.99 μs has a position and width (0.21 μs FWHM) consistent with those predicted by a SIMION [61] simulation for Ba^+ ions (5.55 μs and 0.09 μs, respectively). A fit of this peak to five Gaussian functions representing the main Ba isotope masses provides an estimate for the spectrometer FWHM resolution of 5.8 amu at $\simeq$137 amu. The assignment of the peak to Ba^+ is corroborated by

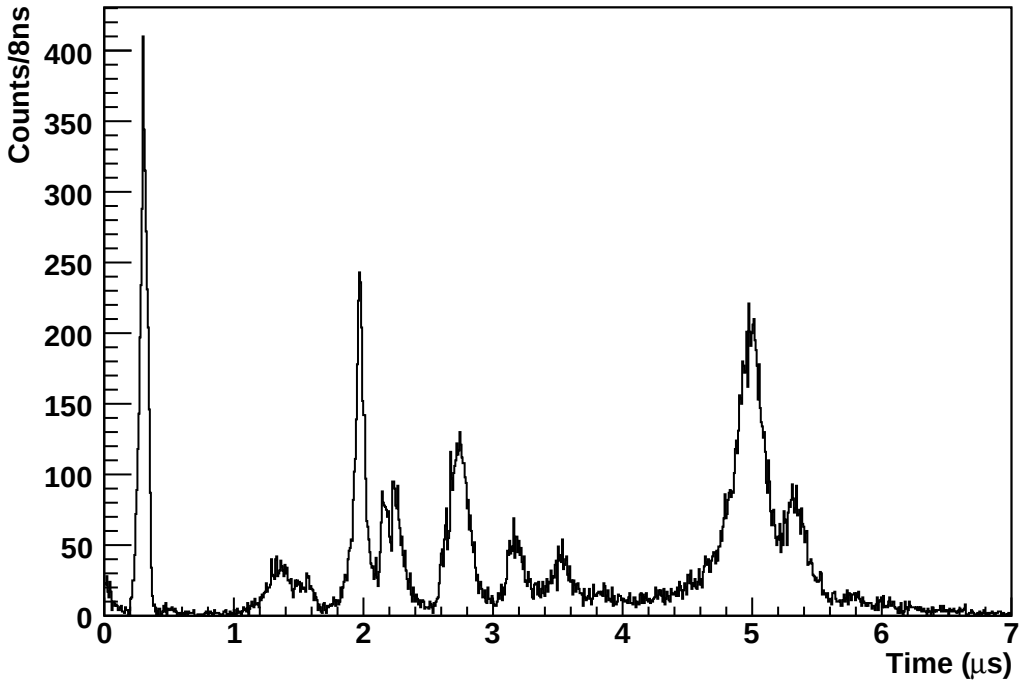

Figure 5.6: Time-of-flight spectrum for a typical Ba source. This source has a measured ^{148}Gd activity of 173 Bq and a 15 nm thick BaF_2 coating. The Ba^+ yield, measured as the integral of the main peak at 4.99 μs, is of 2.7 Hz. Assignments for other peaks can be seen in Table 5.1.

the observation that no such peak is present in a source where the BaF_2 coating is replaced by Al.

Time (μs)	Measured mass (amu)	Possible assignment (known mass in [ ])
0.31	*1.01*	*H^+ [1.01]*
1.44	12.9	C^+ [12.0]
1.99	23.5	Na^+ [23.0]
2.16	27.6	Si^+ [28.1]
2.23	29.3	–
2.75	43.5	$C_2H_5O^+$ [45.1]
3.19	57.9	$C_3H_8O^+$ [60.1]
3.55	70.9	Ba^{2+} [68.7]
4.99	*137.3*	*Ba^+ [137.3]*
5.33	156.2	BaF^+ [156.3]

Table 5.1: Possible assignment of the time-of-flight peaks for the source in Fig. 5.6. The associations of H^+ and Ba^+ (in italics) are assumed and used to compute the mass values for the other peaks.

The time-of-flight spectrum for light masses is similar to the one observed for the source coated with Al (not presented in this thesis), though its interpretation poses some challenges because of the limited resolution of the spectrometer. A possible assignment, obtained using as reference the Ba^+ peak and the peak at 0.31 μs, assuming to be due to H^+ is shown in Table 5.1. The presence of a prominent Na^+ peak is not surprising, given the common presence of sodium contamination on surfaces. Emission of some Si from the substrate is not unexpected, while $C_2H_5O^+$ and $C_3H_8O^+$ are commonly observed in mass spectra of the IPA that is used in the Gd plating process. No compelling assignment is available for the peak at 2.23 μs. Finally, the satellite peak at a mass larger than that of Ba is not present in the Al coated source and it may be attributed to BaF^+.

The presence of these species is corroborated by X-ray Photoelectron Spectroscopy (XPS) [7] performed on the source. The XPS spectrum indicates the presence of Ba, F, Na, and C and O consistent with an organic compound (possibly IPA). Furthermore,

[7] SSI S-Probe XPS Spectrometer, Stanford Nanocharacterization Facility.

XPS spectra of silicon substrates electroplated with plating solutions containing and not containing Gd indicate that the low-mass contaminants arise out of the electroplating process, either because they are dissolved in the plating solution or because the silicon substrate is exposed to air.

5.2.3 Rate of Ba^+ production

The rate of Ba^+ production can be determined by integrating the area under the Ba^+ peak in a time-of-flight spectrum. For an accurate characterization of the source, this measured rate should equal the predicted rate. The predicted Ba^+ production rate can be calculated from the source activity, the "sputtering" yield, and the spectrometer transport efficiency.

The source activity is determined by reading out the PIPS® detector on which the source is fabricated. The "sputtering" yield can be obtained from the SRIM simulation shown in Fig. 5.3. For a source with 15 nm of BaF_2, this yield is about five Ba/Sm. One should note, however, that SRIM simulations are unable to distinguish between neutral and charged states. The expected barium ion fraction, $\alpha = n_+/n_{\text{total}}$, is thus not known.

A general understanding of the ion fraction in sputtering is still an open question, even for pure metals, and not much data exists for ionic compounds, such as BaF_2 [62]. Some models and experimental data describe α with the general form

$$\alpha = F\exp\left(-\frac{v_0}{v}\right) + G \tag{5.3}$$

where F is a constant that takes into account the electronegative of the species, v is the velocity, and G is another constant that takes into account the ionization potential of the atom, the work function of the surface, and the electron temperature. Ion emission takes place around a critical velocity v_0 of $\sim$2 cm/μs [62]. The net result of this function is that the fraction of ions is low at low energy and approaches unity at higher energy. For barium, this transition takes place at $\sim$300 eV. According to SRIM, 17% of barium atoms emitted by the source have energies greater than 300 eV, and so are thought to be ionized. The actual energy distribution of Ba^+ ions affects

the transport efficiency of the spectrometer significantly. While such efficiency is calculated to be 85% for the entire energy distribution produced by SRIM, it is only 8% for the part of such energy distribution exceeding 300 eV.

For the spectrum in Figure 5.6, the Ba^+ yield is measured to be 2.7 Hz. Using the α activity of 173 Bq, SRIM predicts a rate of Ba emission of 430 Hz for the 15 nm thick BaF_2 coating (see Figure 5.3). Assuming that the ions comprise only those Ba atoms ejected with energy above 300 eV (17% of the total), the Ba^+ emission rate is calculated to be 73 Hz. Using the spectrometer efficiency of 8% (appropriate for this energy range), a rate of 5.8 Hz is predicted to arrive at the CEM. The ratio between this figure and the measured rate of 2.7 Hz is consistent with typical CEM efficiencies for ions with the velocities expected here. The agreement between predicted and measured rates indicates that Ba^+ production is well understood.

Chapter 6

Desorption and RIS of Barium

6.1 Desorption Techniques

As described in §2.3.1, an ion-transport probe based on resonance ionization spectroscopy necessitates the inclusion of a desorption step. For this probe to be successful, three desorption requirements must be met:

1. The adsorbant release has to be selective: If possible, one would want only the desired species (barium in this case) to be released from the probe in order to minimize background. This is particularly important if the barium ion is then injected into a buffer gas-cooled quadrupole ion trap for identification, because this trap has limited acceptance and the presence of a substantial amount of background atoms, ions, or molecules might cause ejection.

2. The release has to be efficient: The desorption step is only one of the many needed for the transportation and identification of barium ions created in the LXe TPC. This means that for the complete process to be viable, all the steps have to be highly efficient. Furthermore, every time the ion transport probe is sent in for barium retrieval only one barium atom is expected to be present, so the release from the probe has to be efficient in the single-ion regime.

3. The barium has to be released as a neutral: neutral release allows for selective ionization of barium using RIS, which results in lower background and higher

detection efficiency.

Taking these requirements into consideration, the selection of both an appropriate desorption technique and a substrate are discussed.

6.1.1 Non-resonant processes

Barium atoms can be removed from the surface of a substrate through laser ablation or desorption. Removal by laser ablation is achieved by melting and vaporization of the sample. Initially, the electrons in the sample are excited by absorption of photons. This excitation then decays quickly into heat [63]. When the lattice temperature exceeds the melting point of the sample, surface damage starts occurring. If additional energy is delivered to the melted spot it will vaporize, creating a plume of mass vapor.

In laser ablation one can focus the laser to a small spot size and have a laser pulse of very short (ns) duration. Since the particle release time is also rather short (μs) [64], this should lead to greater atom overlap efficiency with the ionization lasers. The main issue with ablation, however, is that the process is inherently complicated and exponentially dependent on the laser power [65], leading to problems of control unless the pulses are very temporally and spatially stable. At the early ablation stage, emitted electrons gain energy from the incoming laser pulse through collisions with the ionized mass vapor leaving the sample surface. As a result of vapor ionization, the ionized mass plume may absorb the laser energy and shield the sample surface from further exposure to the laser light [66]. This means that even if the pulses are stable, the amount of ablation starts out high on the first pulse and decreases in subsequent pulses. Furthermore, mass leaves the sample surface in the form of electrons, ions, atoms, molecules, clusters, and particle separated in time and space [66], increasing the background and possible reducing the overall efficiency. Ablation also causes irreversible surface damage to the sample, which could affect the efficacy of the substrate as an ion tip and the reproducibility of results.

These problems might be mitigated with the use of a fiber, as it results in greater laser beam uniformity. More control could be had over what is released by having a uniform beam, so that with one shot only a monolayer of barium (and not the

substrate atoms) is released. A UV laser could also be used to dissociate or break up problem molecules created by ablation.

In laser-induced thermal desorption, a pulsed laser is used to thermally heat a surface and desorb molecules [67]. As with laser ablation, light absorption results in electron excitation which then decays into heat. The heat diffuses with time τ during the pulse a distance $\Delta x=(2\alpha\tau)^{1/2}$ into the solid, where α is the thermal diffusivity. When a certain laser power density threshold is reached, surface phonons can couple into the adsorbate bound states, resulting in the breaking of the surface bond [68].

The laser energy required for thermal desorption of barium on a substrate can be determined from a simple model that assumes an energy pulse at the surface of a semi-infinite solid. In this model, the temperature response caused by laser heating is given by [69]:

$$T - T_i = \left(\frac{Q_0}{A\rho c(\pi\alpha\tau)^{1/2}}\right) e^{\left(\frac{-x^2}{4\alpha x}\right)} \tag{6.1}$$

where ρ is the density, c is the heat capacity, and x is the distance (depth) from the surface where heating occurs. Because this is a model for a semi-infinite solid, x is considered to be almost negligible with respect to the total thickness of the solid; the part deep in the bulk remains unaffected by the temperature change in the surface. Though more complicated models of surface temperature rise resulting from laser light exist and are extensively described in [70] and [71], this one was found to be sufficient in providing a general idea of the required parameter values.

At x=0, and assuming a 10 ns laser pulse and a silicon substrate, one thus has

$$T - T_i = \frac{Q_0}{A}\left(0.358\frac{^\circ C}{J/m^2}\right) \tag{6.2}$$

Desorption of sub-monolayers of barium from silicon has been observed at temperatures of at least 800 °C [72]. This corresponds to a laser energy density of 0.223 J/cm^2, and for the 10 ns laser pulse, a power density of 2.23x10^7 W/cm^2. This power density is within the 10^6-10^8 W/cm^2 range usually observed for desorption [73]. It is important to note that impurities have been found to enhance the desorption of barium from metallic surfaces [74], and so one might be able to achieve barium desorption from silicon with less laser energy in this manner.

Ablation usually occurs with densities greater than 10^9 W/cm^2 [73]. This should be avoided so as to minimize the number of ions and maximize the number of neutrals produced for greater efficiency of the desorption and resonance ionization spectroscopy (DRIS) process. For nanosecond pulses, the ablation threshold fluence F_{th} is proportional to the density ρ, the heat of evaporation Ω, the thermal diffusivity α of the substrate, and the duration τ of the laser pulse [75]:

$$F_{\text{th}} \sim \rho\Omega\alpha^{1/2}\tau^{1/2} \tag{6.3}$$

For silicon, this threshold is calculated to be 2.8 J/cm^2, in agreement with experimental values ([76] and its references) and substantially above the energy density required for thermal desorption of barium. This indicates that it is possible to desorb barium from silicon without causing ablation of the silicon substrate, which substantially reduces background for a RIS transport probe. For these reasons, and because it is a rather clean material and readily available, silicon was chosen as the substrate in the DRIS experiments described in this chapter.

6.1.2 Desorption induced by electronic transitions

For a particle to be removed, its bond from the surface of a substrate must be broken. In thermal desorption, as has been previously described, this occurs in thermal equilibrium with the substrate, so that the desorbed particles exhibit a Maxwellian distribution in energy with the temperature equal to that of the substrate. But desorption can also be initiated by transformation of the potential energy of an electronic excitation localized near the particle-surface bond into the kinetic energy of the desorbed particle. This process is known as desorption induced by electronic transitions, or DIET [77].

DIET has been observed mainly in alkaline atoms. The alkali is adsorbed in ionic form on the surface of a substrate [78]. Photon absorption generates hot electrons in the substrate. Some of the hot electrons scatter into an empty resonance state of the alkali, neutralizing it [79]. Since the transition occurs in the repulsive part of the neutral alkali-substrate potential energy curve, the neutral atom is repelled away

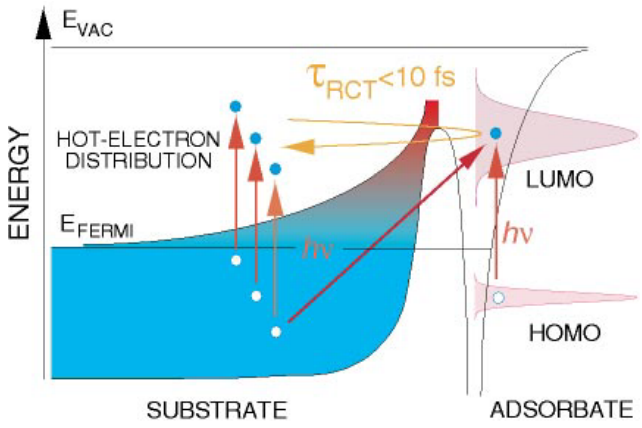

Figure 6.1: Excitation pathways in surface photochemistry. Photochemistry is initiated through the excitation of an unoccupied state of an adsorbate by the scattering of photogenerated hot electrons. From [6].

from the surface. If sufficient kinetic energy is gained in this process, then it will desorb. An illustration of this process is shown in Figure 6.1.

Photodesorption of single potassium atoms from a graphite surface covered with a monolayer of potassium has been observed at 4.9 eV and with a cross section $\sigma = 1.8\text{x}10^{-20}$ cm^2 [79]. Photodesorption of sodium atoms has been similarly observed from a silicon dioxide surface with submonolayer coverage of sodium at ∼5 eV with a cross section $\sigma = 3\text{x}10^{-20}$ cm^2 [78]. In both cases the alkali atom is adsorbed on the substrate surface with some ionicity. If barium, which has a similar ionization potential to sodium, also has partial ionicity when adsorbed, then DIET could very well be possible. This would depend on the number of hot electrons with the right energy scattered towards the surface of the substrate, the electron attachment cross section, and the positions of the potential energy curves of the ionic and ground states.

DIET could allow for very selective desorption of barium, but the photon energy required (estimated at ∼5 eV) would make the use of expensive high-energy UV lasers necessary. For this reason, and because the development and implementation of this system for barium was deemed too complicated given the time constraints of

the work in this dissertation, this desorption method was rejected in favor of laser-induced thermal desorption, which is easier to implement.

6.2 Initial DRIS Setup

The first version of a desorption and resonance ionization spectroscopy (DRIS) setup was designed as a proof-of-principle system for the combination of these two steps. Laser-induced thermal desorption is attempted from the surface of a silicon substrate onto which barium has been deposited. After a short delay, resonance ionization is attempted.

6.2.1 Vacuum system

The vacuum system is the same as described in § 4.2.1, with the addition of a $\sim$ 1x1 inch silicon[1] substrate mounted on a stainless steel support directly facing the CEM used for ion detection. The substrate is kept at ground. A schematic diagram of the experimental setup is shown in Fig. 6.2.

6.2.2 Spectroscopic laser system and optics

The 1064 nm output beam from a Quanta-Ray Q-switched Nd:YAG laser[2] is bounced off two glass slides and injected into a bare 400 μm core diameter multimode fiber[3] after focusing with a f=50 mm lens. The silica cladding is not removed. The fiber is bare so as to maximize the injected energy. For a 10 ns pulse, a maximum injection energy of about 18 mJ/pulse is achieved. Transmission of 50-70% is routinely achieved. The output end of the fiber is also bare, though polished using a specially made fiber holder. The laser can be operated at 1 or 10 Hz.

[1] p-type boron-doped Test I wafer, R=10-90 Ωm, obtained from the Stanford Nanofabrication Facility stockroom, Stanford, CA

[2] Model GCR-150, Spectra Physics, Irvine, CA

[3] Silica Core/Silica Clad Plastic Coated Fiber, Standard OH UV-VIS Superguide Series, Model SFS 400/440Z, 0.22 NA, Fiberguide Industries, Stirling, NJ

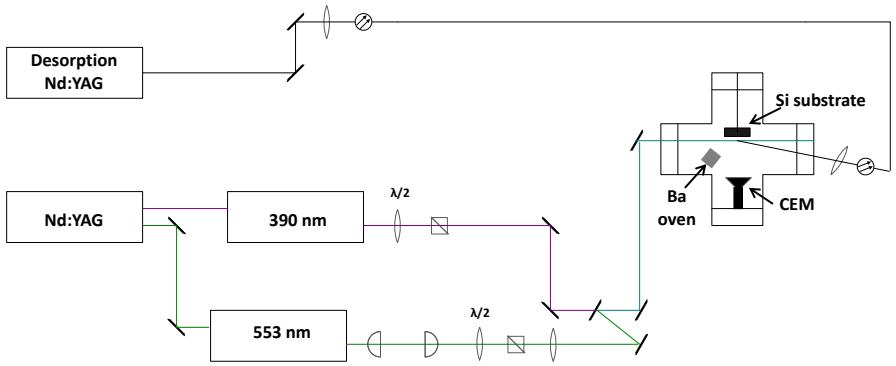

Figure 6.2: Setup for initial experiments on DRIS of barium. A 1064 nm laser beam, delivered via a fiber, desorbs Ba atoms from a Si substrate. The output beams of two dye lasers at ∼553 nm and ∼390 nm are shaped, spacially combined, and injected into the vacuum chamber.

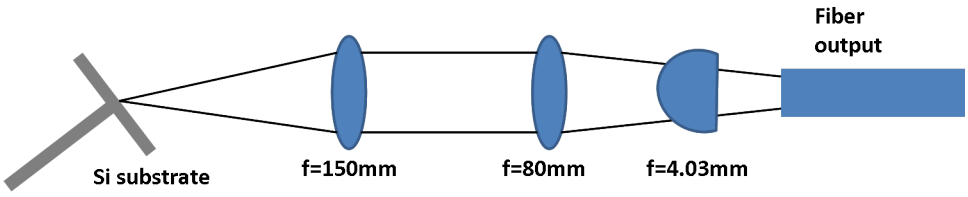

Figure 6.3: Desorption optics used in DRIS experiments. The output of a 400 μm core fiber is collimated with an asphere, recollimated with a lens, and focused with another lens to a spot with radius 1.67 mm on the silicon substrate.

Light coming out of the fiber is collimated with an f=4.03 mm asphere. Because of the large divergence (49.6 mrad, half-angle), the beam is recollimated with a f=80 mm lens. The beam is then focused with a f=150 mm lens through a window to a spot with radius 1.67 mm. It is thought that the beam is focused right on the Si substrate, though it is difficult to measure this exactly. A schematic diagram of the desorption optics is shown in Fig. 6.3.

The fiber output optics are mounted on a micrometer stage with a linear actuator that allows for movement in two axis. Light is injected onto the vacuum chamber where the Si substrate is located at a ∼60° angle.

The setup and optics for the RIS lasers are the same as the ones described in

§ 4.2.2. The beams are injected parallel to the target, with the addition that the last mirror is mounted on a micrometer stage so that the distance between the beams and the target can be changed.

6.2.3 Data acquisition

As in the vapor-phase RIS experiments, the data acquisition is triggered by the output signal from the Q-switch of the desorption laser and a CEM is used for ion detection. A National Instruments waveform digitizer[4] is used as a counter in the manner described in detail in § 4.2.3. An oscilloscope is used to monitor signals. A faster National Instruments waveform digitizer[5] is used to record the CEM waveform for a certain period of time (a few μs) after the desorption laser has triggered the acquisition. A time-of-flight spectrum can thus be constructed in this manner. The combination of these digitizers leads to both count-rate and time-of-flight data which will be used to demonstrate the success of DRIS in the next section.

6.2.4 Results

In data taking conditions, the chamber is kept at a $\sim$1 x 10^{-8} Torr vacuum. The barium oven is run for up to an hour, depositing barium atoms on the silicon substrate. The barium oven is then turned off, and the desorption laser is fired at the substrate, triggering the data acquisition. After an experimentally-determined delay of 1.5 μs, the RIS lasers are fired parallel to the substrate, and the signal detected on the CEM is recorded. A schematic diagram of this approach is shown in Fig. 6.4. If need be, the position of the desorption laser on the Si substrate and of the RIS lasers relative to the substrate can be adjusted to maximize overlap with the barium atoms/ions.

Every time the vacuum chamber is opened, the Si substrate is replaced, the chamber is baked afterwards at $\sim$120 °C for a day to remove water vapor, and a desorption background run is performed. Background runs on the silicon substrate, done before

[4]Model NI 5112, 100 MS/sec, 8-bit
[5]Model NI 5114, 250 MS/sec, 8-bit

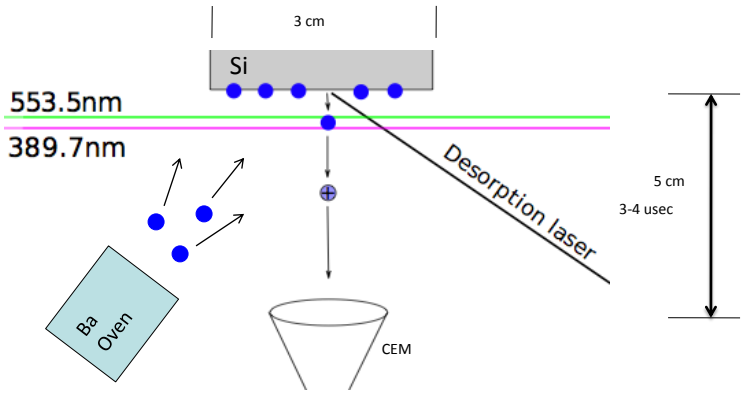

Figure 6.4: A simple schematic diagram that shows how desorption and resonance ionization of barium is achieved and detected. A barium oven deposits barium atoms onto a silicon substrate. The atoms are thermally desorbed via a laser beam and are then resonantly ionized by two other laser beams. The resulting barium ions are detected by a CEM.

any barium is deposited and using only the desorption laser, indicate only the occasional presence of a pulse 1-1.5 μs after the desorption trigger. This pulse is thought to be due to Si^+.

A typical data sequence involves first doing resonance ionization of barium from the atomic beam produced by the oven as it deposits barium on the silicon substrate. This allows one to make sure that the spatial overlap of the two ionization lasers is optimal. Then, laser ablation of barium from the substrate is performed so as to ascertain the location of the adsorbed barium on the substrate. Once the alignment and power of the lasers have been deemed satisfactory, tests for DRIS can commence. This alignment or calibration sequence is done only when a good DRIS signal cannot be obtained, so as to minimize ablation-induced disruptions to the surface of the substrate and the depletion of barium atoms on the substrate.

Using the DAQ system in its counter mode, the time structure of an ablated barium pulse can be seen. An example is shown in Fig. 6.5. Only the desorption laser beam is present, with an energy of 4 mJ/pulse. The number of counts in the CEM is averaged over 5 s. Time 0 s indicates the desorption laser trigger. Here, the pulse is seen within the 1.7-3.2 μs gate deemed to be optimal for barium in the resonance

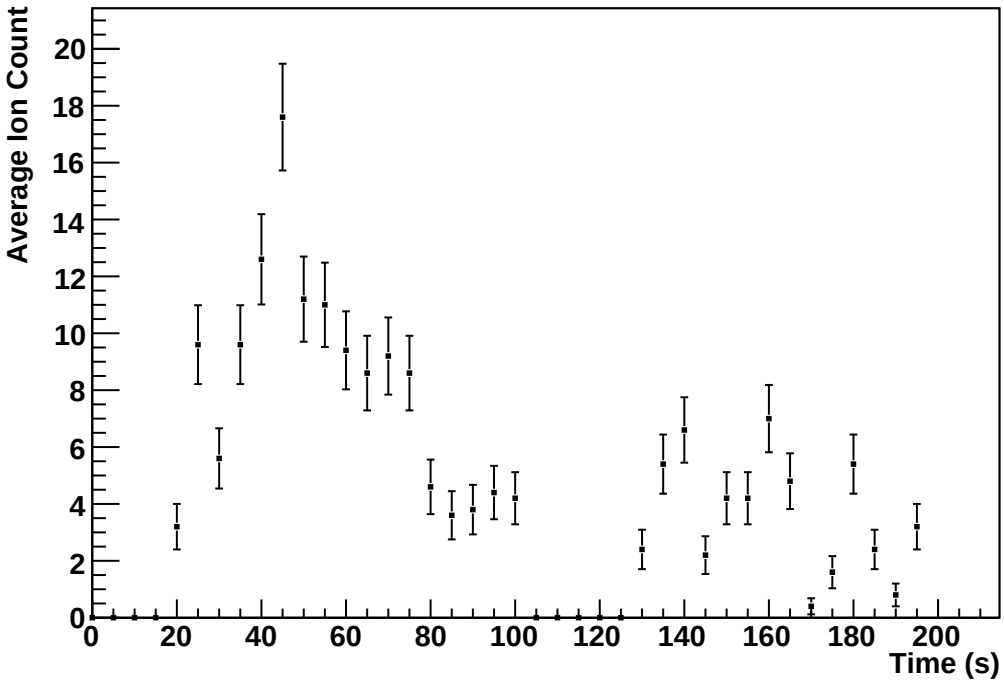

Figure 6.5: Time structure of an ablated barium pulse found within 1.7-3.2 μs from the desorption laser trigger. Originally the desorption beam is not in the chamber. After 20 s, the beam is let in and the count rate increases. When the beam is blocked (100-130 s), the count rate decreases to zero.

ionization experiments described in Chapter 4. If the laser beam is blocked, as it is at t = 0-20 s and 100-130 s, no pulse is seen. Since this pulse is seen only after barium deposition on the target and with no ionization lasers, and since this pulse occurs at the optimal barium window and at a different time than the Si^+ background pulse, it is easy to see that it is indeed due to ablated barium. The signal also exhibits the typical ablation time structure, described at the beginning of this chapter, where the most number of ions are released in the first few shots and the number then decreases at each subsequent shot.

The reason why seeing an ablated barium pulse is important is that it allows for calibration of the time-of-flight spectrum. If one knows at what time after a trigger

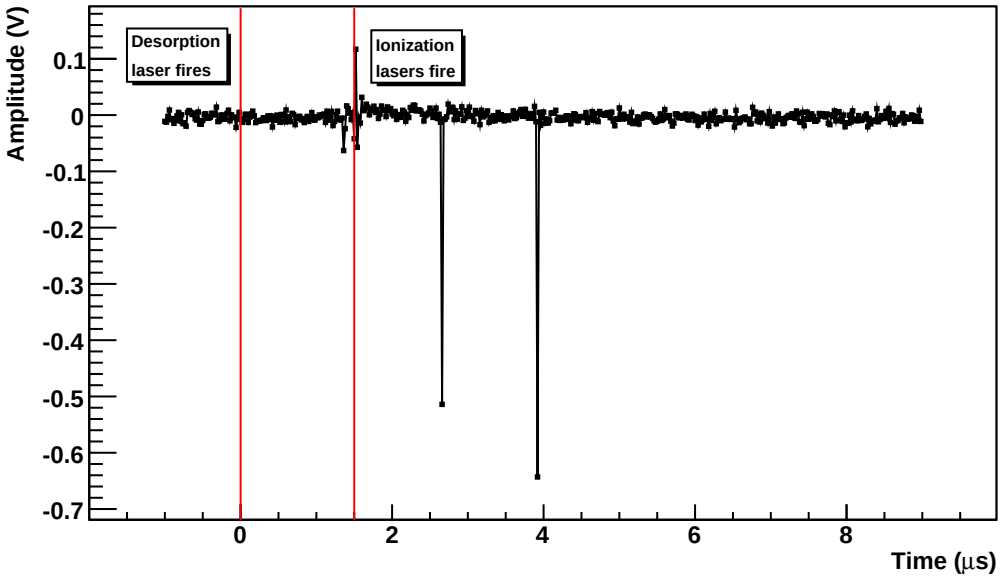

Figure 6.6: Time-of-flight oscilloscope trace. The desorption laser fires at time = 0 μs. Ablated barium can be seen at 2.5 μs, and desorbed and resonantly ionized barium can be seen at 4 μs. The delay between the desorption and ionization lasers in 1.5 μs. The bipolar signal at 1.5 μs is due to pickup from the ionization lasers firing.

ablated barium is seen, and one knows the delay between the desorption/ablation and the ionization lasers, then one knows where to expect the DRIS barium pulse.

Fig. 6.6 shows a typical oscilloscope trace of ion signals obtained by the CEM after barium deposition on the target, desorption, and resonance ionization. In this particular case, the desorption laser energy was 2 mJ/pulse, the green laser energy was 0.027 mJ/pulse, and the UV laser energy was 0.059 mJ/pulse. Two ions pulses are present. An ablated barium pulse is seen at about 2.5 μs, which is not of interest as described earlier, and a DRIS barium pulse is seen at 4 μs. These pulses are separated by 1.5μs, which is the delay between the desorption and ionization lasers.

If one looks at the dependence of this 4 μs pulse on the various laser beams using a gate of 3.6-5 μs (Fig. 6.7), one can see that the signal disappears if either the desorption or ionization beams are blocked. The fact that this signal is seen after the

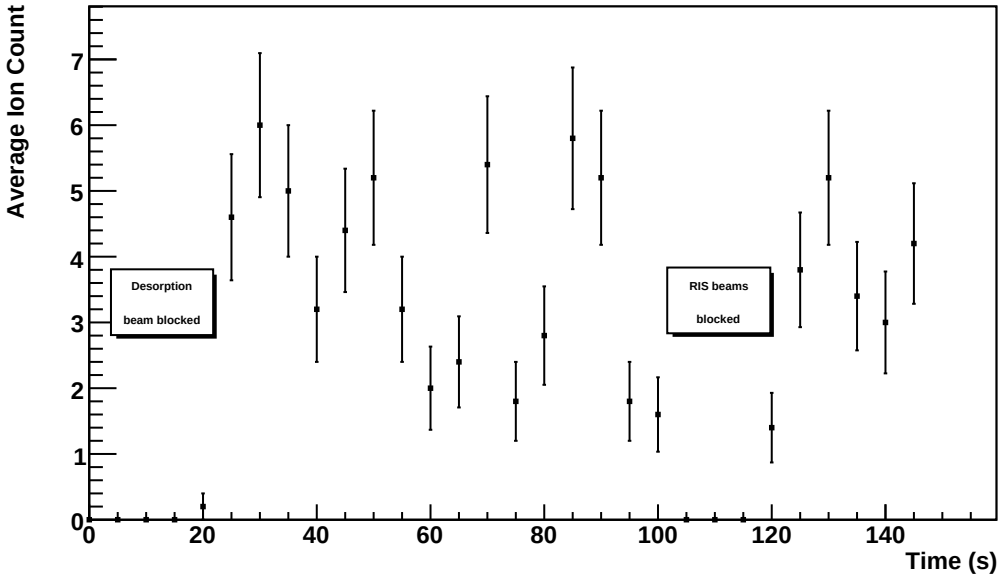

Figure 6.7: Time structure of a DRIS barium pulse within a 3.6-5 μs gate after the desorption laser trigger. The desorption beam is unblocked after 20 s, and counts start to be seen. Between 100-120 s, the ionization beams are blocked and the count rate decreases to zero.

barium oven has been run, only when both the desorption and resonance lasers are present, and with a time difference from the ablated barium signal equal to the delay between the lasers strongly suggests that is due to DRIS barium.

Using the DAQ system in its time-of-flight configuration provides a different and more informative way of looking at data. An example of time-of-flight spectra of the pulses seen by the CEM from the t=0 s desorption trigger over a period of 8 μs is shown in Fig. 6.8. For this data, the desorption laser was operated at 1 Hz and the ionization lasers at 0.5 Hz, so that they would be alternatively on and off with each desorption shot. This allows for differentiation in ions produced when each type of laser is on. The panel on the left shows the spectrum when all laser are on, and the one on the right the spectrum when only the desorption laser is on. The desorption laser energy was 2.5 mJ/pulse, the green laser energy was 3.5 mJ/pulse, and the UV laser energy was 2.5 mJ/pulse.

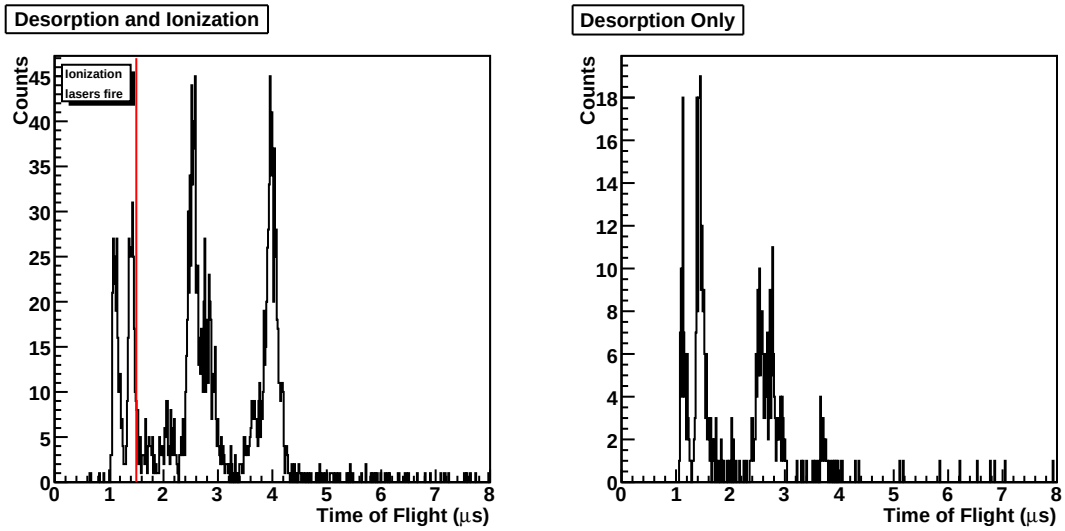

Figure 6.8: Time-of-flight spectra of ions coming off the target when only the desorption laser is on (right) and when the desorption and ionization lasers are all on (left). A pulse from DRIS barium can be clearly seen at 4 μs, a pulse from ablated barium can be seen at 2.5 μs, and a pulse from ablated silicon can be seen at 1.2 μs.

There is a significant difference between the two spectra: a pulse at 4 μs can be seen only when all of the lasers are present, and disappears if only the desorption laser is on. This pulse is seen at the same time after the data trigger as when the DAQ system is run in its counter configuration. The spectra also indicate the presence of ablation-induced signals in the forms of pulses at 1.2 μs (Si^+) and 2.5 μs (Ba^+), as previously seen. The time difference between the ablated and DRIS barium pulses is once again 1.5 μs.

The data presented in this section shows that thermal desorption and resonance ionization of barium using a silicon target is in principle possible.

6.3 Low-Flux Setup with Radionuclide-Driven Barium Source

Using a barium oven as a source of barium does not allow for an efficiency measurement of the DRIS process because the amount of barium produced is not easily measureable. Since the results obtained with the experimental setup described in the previous section are positive and encouraging, the setup was modified to allow for efficiency measurements. This new low-flux setup makes use of a radionuclide-driven single-ion barium source (see Chapter 5).

6.3.1 Experimental setup

Fig. 6.9 shows a schematic diagram of the low-flux setup. A square 64 mm^2 silicon substrate is mounted at the end of a 2 mm diameter titanium rod with silver conductive epoxy. The substrate is cut from a silicon wafer with a diamond scribe so as to minimize exposure of the polished front surface to chemical or mechanical treatments. The barium source is mounted directly in front of the substrate, at a distance of 65 mm. The CEM is mounted at a distance of 19 mm from the substrate and 68 mm above it. Both the source and the CEM are equipped with a plate and a lens for ion acceleration and focusing. These ion guides are also made out of titanium in order to minimize background should they be hit by scattered laser light, since titanium has a very different time of flight than the much heavier barium. The optical setup and DAQ system are the same as described in the previous section.

The low-flux setup can be run in two configurations: "loading" and "DRIS". In the "loading" configuration, the CEM and its accelerator plate and lens are grounded (or "off"). The Si substrate is biased at -1000 V. The source plate is biased at -1000 V and the lens at +20 V ("on"). With these voltage settings, ions are guided from the source onto the substrate. In the "DRIS" configuration, the CEM cone is biased at -2000 V, its accelerator plate is biased at -1000 V, and the lens at +50 V ("on"). The Si substrate is grounded. The source plate is biased +100 V and the lens is grounded ("off"). With these voltage settings, ions (once desorbed from the

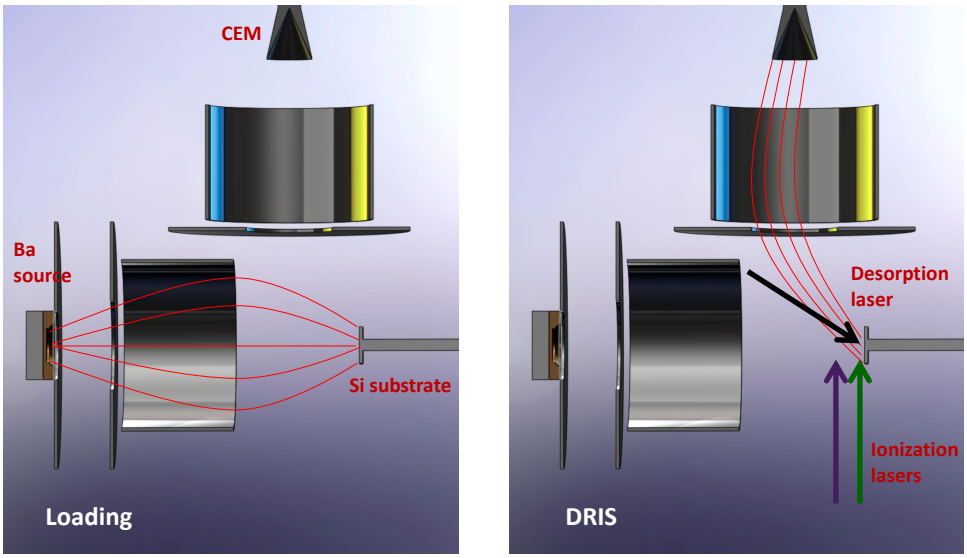

Figure 6.9: A schematic diagram of the DRIS low-flux setup in which a simple plate and lens system guides ions from a radionuclide-driven barium source to the silicon substrate (left), and from the substrate to the CEM after desorption and ionization (right). Ion trajectories are shown in red.

substrate and ionized by the RIS lasers) are guided from the substrate to the CEM. No ions from the source are deposited onto the substrate in this configuration. A summary of the voltage settings can be seen in Table 6.1.

6.3.2 Results

Data taking proceeds under the same conditions as in § 6.2.4. The source is first run overnight (∼14 hours) in the "loading" configuration, and the system is then switched to the "DRIS" configuration to begin data taking. A desorption laser pulse at 1 Hz or 10 Hz triggers the data acquisition, the ionization lasers are fired with a 1.4 μs delay at 0.5 Hz or 5 Hz, and ion signals in the CEM are digitized and recorded for the 20 μs following the desorption trigger. Each data record also contains information on the wavelength of the ionization lasers, which are kept on resonance at 553.54 nm and 389.67 nm. Each data set typically contains a few thousand records.

An example of a time-of-flight spectrum obtained in this manner is shown in

	Loading	DRIS
CEM cone	0 V	-2000 V
CEM plate	0 V	-1000 V
CEM lens	0 V	+50 V
Si substrate	-1000 V	0 V
Source plate	-1000 V	+100 V
Source lens	+20 V	0 V

Table 6.1: Voltages for different ion optics in the "Loading" and "DRIS" configurations of the Low-Flux Setup.

Fig. 6.10. A prominent pulse is present at 9 μs, and only when both the desorption and ionization lasers are on. Very little background in the 8.5-9.5 μs window is seen. The long time of flight of the pulse indicates that the ion that causes it has a high mass. It is likely then that this is desorbed and resonantly ionized Ba^+.

Confirmation of the nature of this pulse can be obtained spectroscopically. If it is indeed resonantly ionized Ba^+, then detuning one of the ionization lasers while keeping the other on resonance should make the pulse disappear. This is what is seen in Fig. 6.11. The plot on the left shows the time-of-flight spectrum obtained when the desorption and ionization lasers are present. If the ionization lasers are both kept on resonance, the prominent pulse at 9 μs is observed (black). If the green laser is detuned +3 nm (blue) or -3 nm (red) from the 553.54 nm resonance in a 553-556-553-550 nm... pattern, the pulse disappears. The plot on the right in Fig. 6.11 shows the time-of-flight spectrum obtained when only the desorption laser is present. No pulse at 9 μs is seen.

6.3.3 Process efficiency

The efficiency of the DRIS process can be obtained if both the number of Ba^+ ions detected by the CEM after desorption and ionization and the number of barium atoms/ions originally deposited on the silicon substrate is known. Integration of the area under the Ba^+ pulse gives the number of Ba^+ ions detected. The number of barium atoms/ions on the silicon substrate is determined from the activity of the

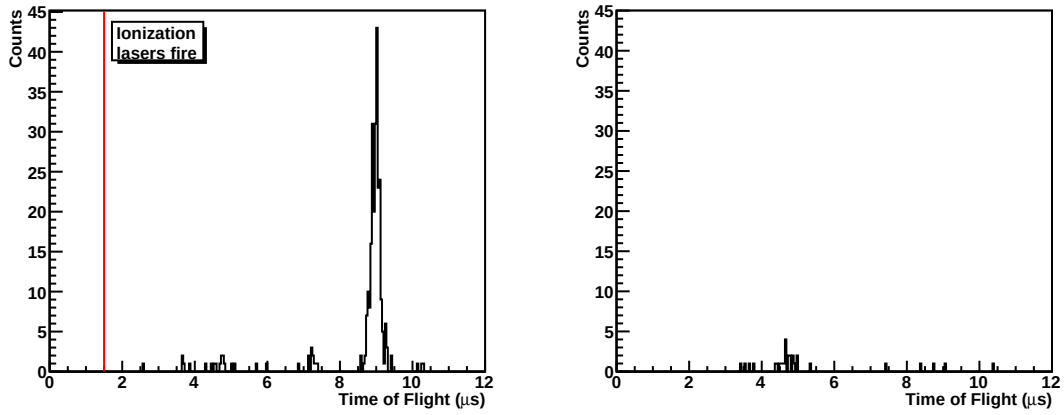

Figure 6.10: Time-of-flight spectra of ions coming off the target when only the desorption laser is on (right) and when the desorption and ionization lasers are all on (left). A pulse from DRIS barium can be clearly seen at 9 μs with very little background.

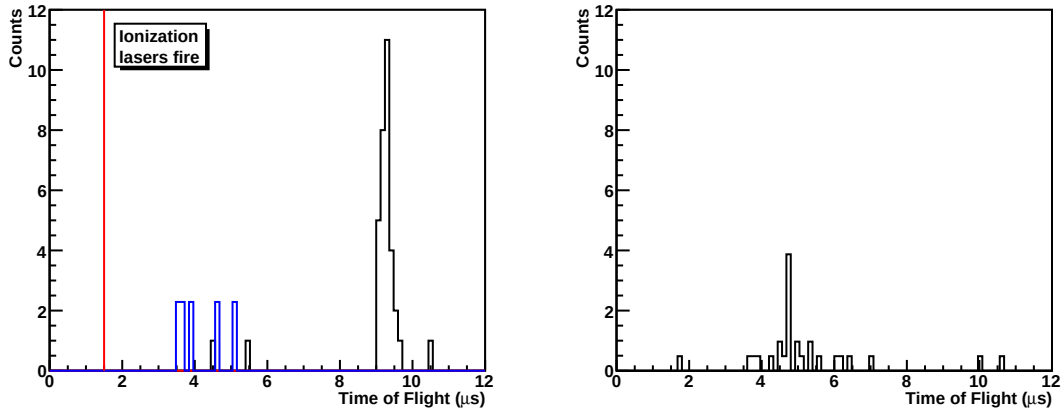

Figure 6.11: Time-of-flight spectrum of ions coming off the target when only the desorption laser is on (right) and when the desorption and ionization lasers are all on (left). Data is taken with the green laser at the 553.54 nm resonance (black) as well as detuned +3 nm (blue) and -3 nm (red), while keeping the UV laser on resonance at 389.67 nm. A peak at 9 μs, corresponding to DRIS barium, is only seen when all the lasers are on and on resonance.

barium source, the number of barium ions produced per decay, and the number of those ions that are transported to the silicon substrate. The source fabrication process is described in Chapter 5. The source consists of 178 Bq of ^{148}Gd covered by 8.8 nm of BaF_2. As can be seen from Fig. 5.3, each Gd decay results in 5 Ba atoms emitted. 18% of the barium emitted by the source is calculated by SRIM to have an energy >300 eV. As was discussed in Chapter 5, this is thought to be the minimum energy required to obtain Ba^+ ions from the source instead of neutral barium. SIMION simulations indicate that the simple plate and lens ion guide for the source has a 2.7% efficiency for guiding ions with E >300 eV to the silicon substrate (this efficiency is 64.9% for all ion energies). Ba^+ is thus deposited on the substrate during the "loading" phase at a rate of 2.2 ions/second. This Ba^+ deposition rate is calculated and not experimentally measured. However, agreement between calculated and measured deposition rates for a similar source in a similar setup, described in Chapter 5 and [80], lead me to believe this number to be accurate.

Neutral loading of the silicon substrate also occurs because it is in direct line of sight of the source. The solid angle subtended by the 64 mm^2 substrate 65 mm away from the source is 1.21x10^{-3} radian. Taking into account, as before, the source activity, the number of barium atoms emitted per gadolinium decay, the percentage of those atoms that are thought to be neutral, and the solid angle, the source deposits 0.44 neutral barium/second. This is an order magnitude less than the amount of Ba^+ deposited in the "loading" configuration, so as long as the time between experimental runs is not too long, neutral loading is negligible. A summary of this information can be found in Table 6.2.

Table 6.3 shows the DRIS efficiencies for five data runs obtained over a period of seven days. DRIS shots are shots in which the desorption and the two ionization lasers are all on and on resonance. Since the resonance lasers are run at half the repetition rate of the desorption laser i.e., alternating on/off, and since the only time a DRIS Ba^+ ion is produced is when all the lasers are on (and on resonance), the ratio of total shots to DRIS shots needs to be taken into account to determine the actual number of Ba^+ ions that should be detected. In this manner, the barium that was desorbed by the desorption laser but could not be ionized because the RIS lasers

Parameter	Value
Activity	178 Bq
Ba/Sm	5
Ions with E >300 eV	18%
Loading eff. E >300 eV	2.7%
Ω	1.21×10^{-3} radian
Ba^+ deposited	2.2 ions/sec
Neutral Ba deposited	0.44 atoms/sec

Table 6.2: Parameters for determining the number of barium ions or atoms present on the silicon substrate.

were off is taken into account for efficiency calculations.

	Run 1	**Run 2**	**Run 3**	**Run 4**	**Run 5**
N shots	1208	8185	7200	6000	30000
DRIS shots	604	4093	2100	6000	14999
Loading t (hours)	14	14	14	17	16
Ba^+ deposited	1.11×10^5	1.11×10^5	1.11×10^5	1.35×10^5	1.27×10^5
t between runs (hours)	24	24	48	72	24
Neutral Ba deposited	3.79×10^4	3.79×10^4	7.59×10^4	1.14×10^5	3.79×10^4
Ba^+ detected	83	252	60	141	94
Efficiency (no neutrals)	0.15%	0.45%	0.19%	0.10%	0.15%
Efficiency (with neutrals)	0.11%	0.34%	0.11%	0.06%	0.11%

Table 6.3: Parameters for determining DRIS efficiency for five different data runs.

For comparison purposes, two efficiencies are provided: one which ignores neutral loading, and one which takes it into account. It can be seen that the number of neutral barium deposited is comparable to the number of Ba^+ deposited during a normal "loading" run after approximately three days, but that having more barium on the target doesn't increase the efficiency of the process. In fact, the slightly higher value of Run 2 notwithstanding, the DRIS efficiency is rather constant at about 1×10^{-3}. This could mean that the present experimental setup is maximized in its efficiency capabilities, and is only sensitive at the 0.1% level, within an order of magnitude. Increasing the efficiency would require a new apparatus.

The question of whether relic barium is present still remains. Relic barium refers to the barium deposited on the silicon substrate during the "loading" phase or by neutral loading that has not been desorbed or removed from the substrate during the "DRIS" phase, and thus accumulates during subsequent runs. Run 1, described in Table 6.3, represents the first time the 64 mm^2 substrate has been exposed to barium (14 hours of Ba^+ together with 24 hours of neutral loading). Its efficiency then could be interpreted as the "true" efficiency, as there is no relic barium. The fact that the efficiency remains relatively constant would seem to indicate that relic barium is not an issue.

The time structure of the Ba^+ pulse might provide some indication of barium being burned off the substrate (completely desorbed) during the "DRIS" phase of the data taking. Such a plot for the barium pulse in Run 2 is shown in Fig. 6.12. The plot shows the number of Ba^+ ions detected as a function of the laser shot number. It is not clear from this plot if there is a trend, though one might venture to say that the number of counts is lower after about 5000 shots. Time structure plots for the other runs are similarly ambiguous. Looking at Table 6.3, one can see that the number of shots in Run 1 is rather low, and the efficiency in Run 2 is higher than average. It might be that there is a threshold of about 6000 shots before the deposited barium is mostly burned off. Since Run 1 only had 1200 shots, some relic barium might be left for Run 2, which might explain the slightly higher efficiency.

It might be insightful to try and separate the detection efficiency from the desorption and ionization efficiency. SIMION predicts a transport efficiency of 31.8% for ions with thermal energy originating at the silicon substrate and going to the CEM. The CEM detection efficiency is estimated to be about 50% (see Chapter 5). This means that for an average of 1.1×10^5 barium ions deposited on the target, 17500 should be detected if the desorption and ionization of the ions is 100% efficient. The measured efficiency is 0.1% instead of the 16% estimated one, a two orders of magnitude different. Of course it could be that the SIMION transport efficiency simulations are incorrect because the actual temperature of the desorbed ions is not known, but it could also be that the desorption and ionization process can be improved, possibly

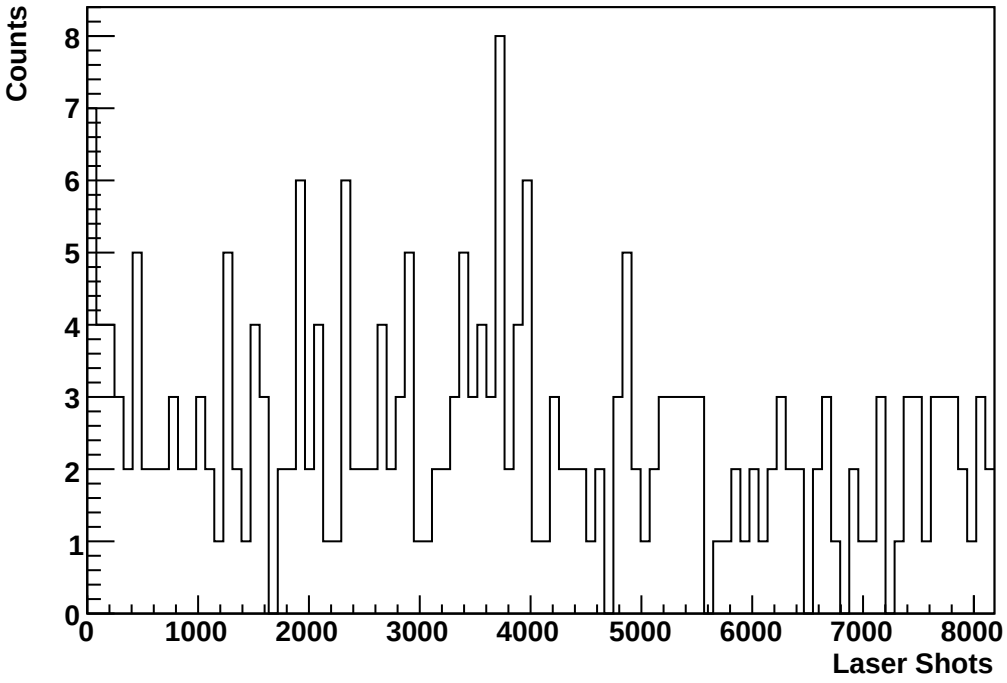

Figure 6.12: Time structure of the Ba^+ pulse seen in Fig. 6.10 (Run 2) in the region 8.5-9.5 μs.

with better desorption optics and spatial overlap between the lasers. The implementation of these improvements, together with more efficient ion transport optics, will be discussed in the next section.

6.4 Single-Ion Setup

In order to achieve single-ion sensitivity with the DRIS process, the Low-Flux experimental setup was altered. This new Single-Ion Setup utilizes better electrostatics to more efficiently transport barium ions from the ion source to the Si substrate, and, once desorbed and ionized, from the Si substrate to the CEM. It also employs different desorption laser optics for a more even beam illumination at the target, and ionization laser optics that allow for better overlap between beams and desorbed atoms.

6.4.1 Vacuum system

The vacuum chamber consists of two 12" conflat flanges screwed into a custom-made zero-length reducer, so the chamber has a characteristic "pancake" shape. Each conflat flange has a 4.5" quartz viewport to allow for laser injection and exit. One of the conflat flanges has a 4.5" port which is connected to a 5-way cross containing vacuum diagnostic equipment (CC pressure gauge and Residual Gas Analyzer) and a 30-l/sec TMP backed by a 10-l/sec dry scroll pump. The other flange has a custom-made 4.5" port comprising two 6-pin feedthroughs and three BNC feedthroughs that allow for high-voltage input and signal readout. The in-vacuum experimental components are mounted on this flange so that they can be easily accessed. These components include a radionuclide-driven ion source, two sets of ion-guiding optics, a Si substrate where ion deposition and desorption take place, and a CEM for ion detection. A picture can be seen in Fig. 6.13.

The ion optics that guide ions from the source to the substrate are similar to the ones employed for characterizing the ion source, as described in Chapter 5. They consist of a three-electrode lens and a two-electrode lens connected by drift tube. Another three-electrode lens guides ions from the Si substrate to the CEM. All ion

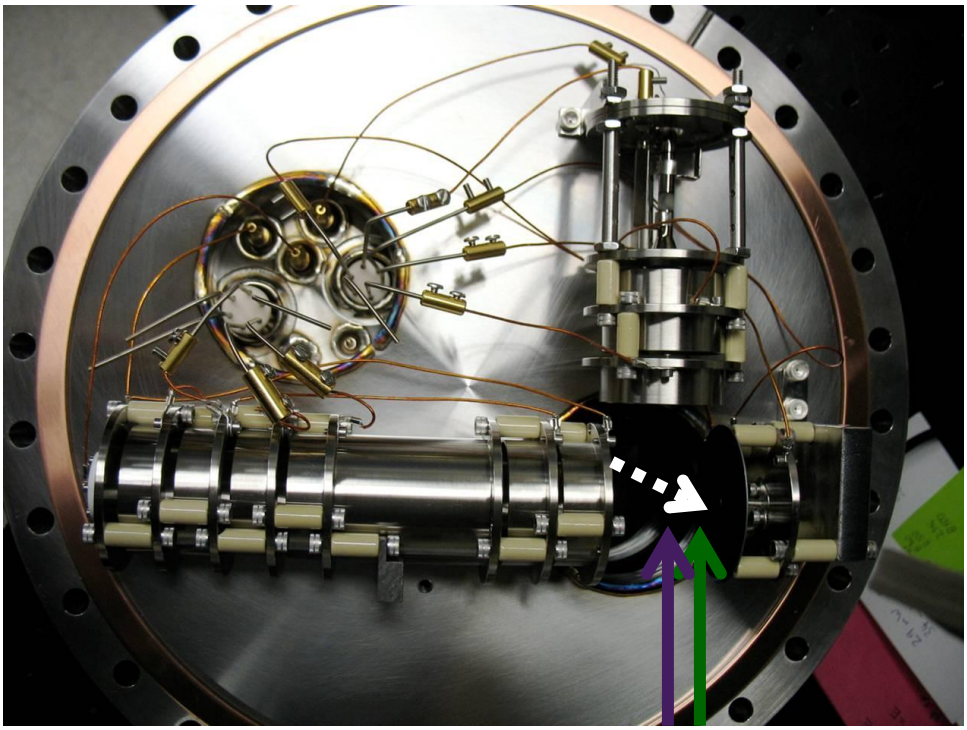

Figure 6.13: Photograph of the single-ion setup. The source is located at the bottom left, next to ion optics that guide ions from it to the silicon substrate. The Si substrate is located at the bottom right, surrounded by a silicon guard ring for better electrostatics. The CEM is located at the top right of the picture, together with its ion optics. The paths of the laser beams are also shown. The desorption beam (white dashed line) enters through the viewport in the back and hits the Si substrate at an angle. The ionization lasers (green and purple lines) enter the chamber parallel to the Si substrate and exit the chamber through the viewport in the back.

optics components are made out of titanium. All in-vacuum electrical connections are made with copper wires and gold-plated wire connectors for UHV compatibility.

6.4.2 Electronics, electrostatics, and silicon substrate design

Two different types of substrates are used, both made out of silicon. The first one is made out of the same type of silicon wafer as the substrates that have been described in this dissertation up to now. Both 4x4 mm square substrates and circular ones with 8 mm diameter are used. The round substrates are cut by the Stanford University Crystal Shop with an abrasive slurry. The second substrate type is made out of a highly resistive silicon wafer [6] featuring two concentric aluminum rings deposited on the back. These rings can be biased so that a potential across the substrate brings ions to its center for better localization. These substrates are cut into 4 mm diameter circles by the Stanford University Physics Machine Shop, also with an abrasive slurry. A picture of the new substrate design can be seen in Fig. 6.14. The substrates are sonicated in acetone and isopropanol baths to remove any particulates that might have been deposited during the cutting process. All substrates are mounted at the end of a 1 mm diameter titanium rod using conductive epoxy. A circular silicon guard ring 48 mm in diameter, placed < 1 mm behind the substrate, is sometimes used. This silicon ring acts as the third electrode in the lens system at the end of the source-to-substrate ion optics and serves to improve the electrostatics so that ion loading is more efficient.

Electrode voltages for the ion optics are optimized using SIMION simulations. An example of these simulations, for a 8 mm diameter substrate, is shown in Fig. 6.15 ("loading" configuration) and Fig. 6.16 ("DRIS" configuration). In the "loading" configuration, voltages are set so that ions can be deposited onto the silicon substrate from the source. In the "DRIS" configuration, voltages are set that so that ions can travel from the substrate to the CEM. A thermal distribution of ion energies is assumed for this configuration for simulation purposes. The efficiency for ion transport in the "DRIS" configuration is close to 100%, regardless of the size and shape of the

[6] $\langle 100 \rangle$ p-type, $>$ 1000 Ωcm, 375-425 μm thick, double-side polished float zone wafer, Wafer Reclaim Services LLCC, San Jose, CA.

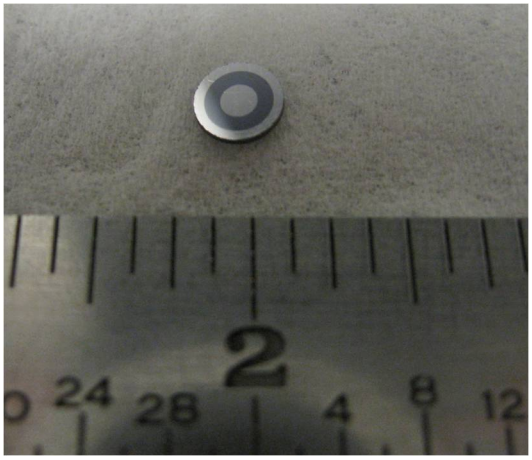

Figure 6.14: Photograph of the back of the new type of silicon substrate. Two concentric aluminum rings are deposited there. Biasing of these rings allows for ions to be localized in the center of the substrate.

substrate used and whether the silicon guard ring is present or not. Ion transport efficiency from the source to the substrate is much more dependent on these factors. This is because the energy profile of the source emittance, determined by SRIM full damage cascades simulations and described in Chapter 5, is rather broad. For the setup shown in Fig. 6.15 in the "loading" configuration, the efficiency is 65% for all ion energies (85% if the silicon guard ring is mounted).

A simplified schematic diagram of the electronics used in this experimental setup is shown in Fig. 6.17. High voltage for electrode, source, substrate, and CEM biasing is provided by a system of 10 MΩ voltage dividers from ±2000 V inputs. Switching of electrode voltages between the "loading" and "DRIS" configuration is done by opto-isolators driven by digital signals supplied by a NI digital I/O unit [7]. When the opto-isolators are "on", their leakage current is high (∼100 μA), and when they are "off" their leakage current is low (∼100 nA). A 7404 Hex Inverter is used to ensure that the digital signals supply the right amount of current to the opto-isolators. The 7404 is powered by a 7805 +5 V voltage regulator. Both the silicon substrate with the concentric aluminum rings and the ion source are biased with batteries (at 15 V

[7]National Instruments model USB-6229 16 bit 250 KS/s Multifunction I/O

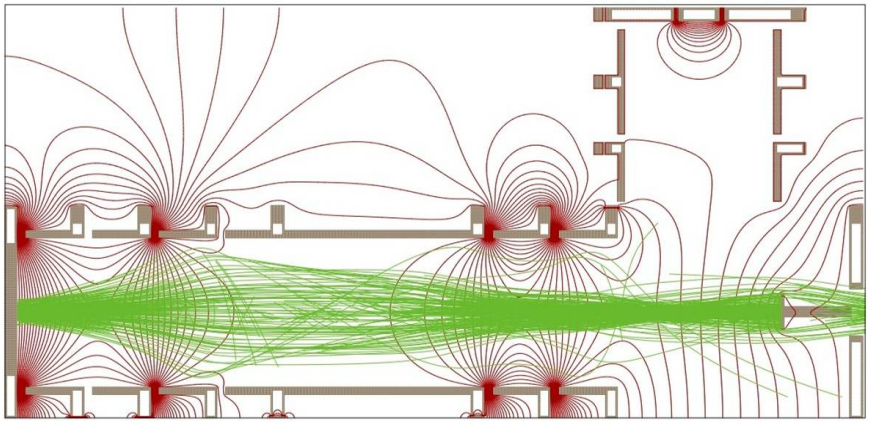

Figure 6.15: SIMION simulations of the "loading" configuration of the single-ion experimental setup with a 8 mm diameter circular substrate and no silicon guard ring. The ion source is located on the left, and the silicon substrate on the right. Ion trajectories are shown in green and potentials are shown in red. The ion transport efficiency is 65%, and increases to 85% if the guard ring is mounted. Courtesy of K. Twelker.

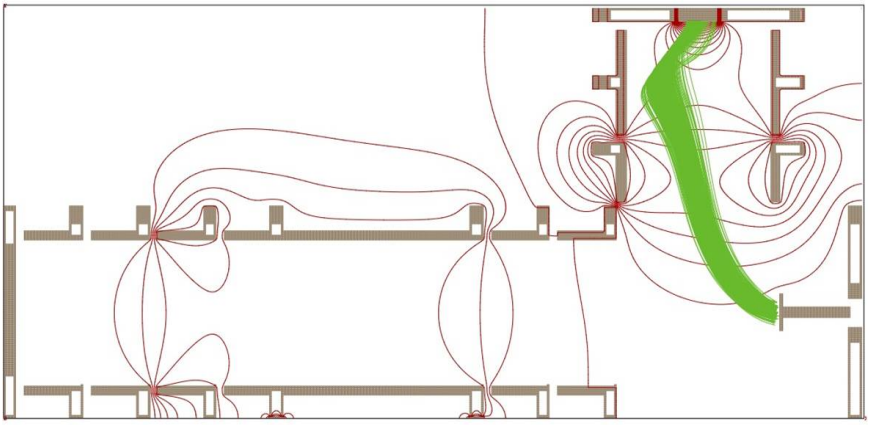

Figure 6.16: SIMION simulations of the "DRIS" configuration of the single-ion experimental setup with a 8 mm diameter circular substrate and no silicon guard ring. The silicon substrate is located on the bottom right and the CEM on the top right. Ion trajectories are shown in green and potentials are shown in red. The ion transport efficiency is 100%. Courtesy of K. Twelker.

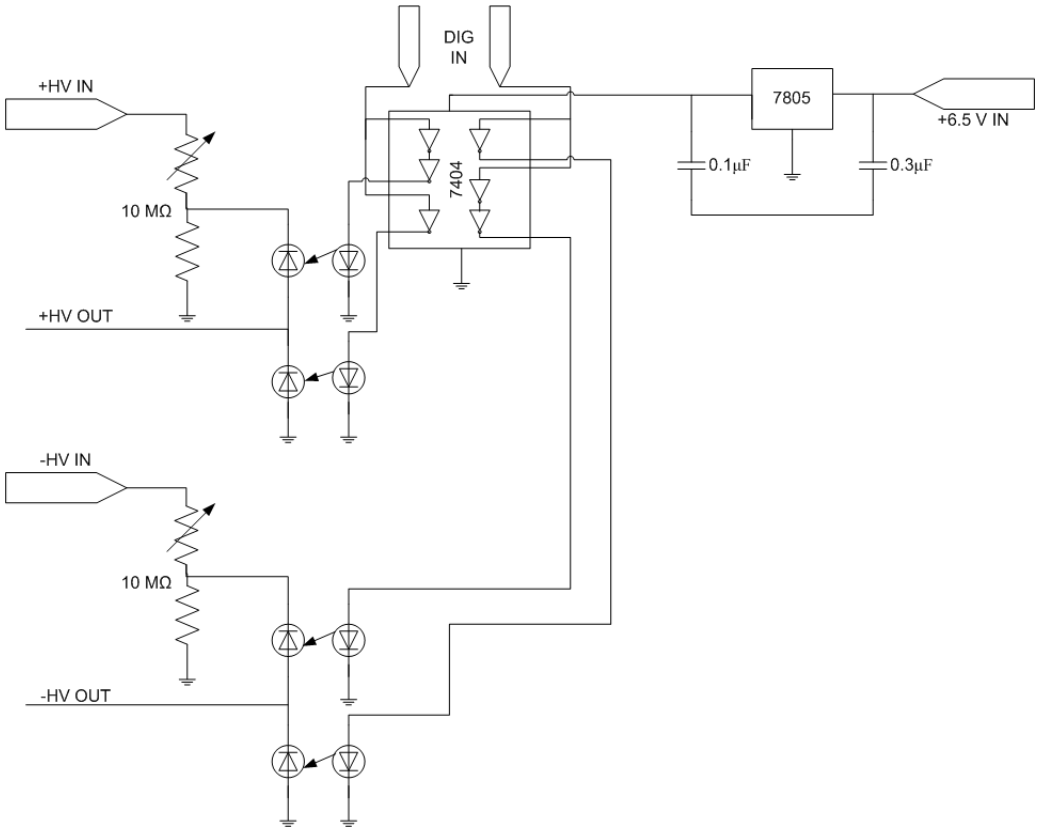

Figure 6.17: Simplified schematic diagram of the electronics used in the Single-Ion Setup. The use of opto-isolators allows for fast voltage switching. The source and substrate biasing diagrams are not shown.

and 45 V respectively, not shown in Fig. 6.17) for so that they can be floated at the requisite high voltages.

The use of opto-isolators allows for voltage switching times of less than one second, which enables operation in the single ion regime. A timing diagram of this operation is shown in Fig. 6.18. Voltages are first set for the "loading" configuration. The radionuclide-driven source then delivers one or two Ba^+ ions to the silicon substrate. The voltages are switched to the "DRIS" configuration, and ions from the source are blocked. The desorption and ionization lasers are fired, and the desorbed and ionized barium is detected by the CEM within a few microseconds. The voltages are set back to the "loading" configuration and the cycle starts again by the time the next

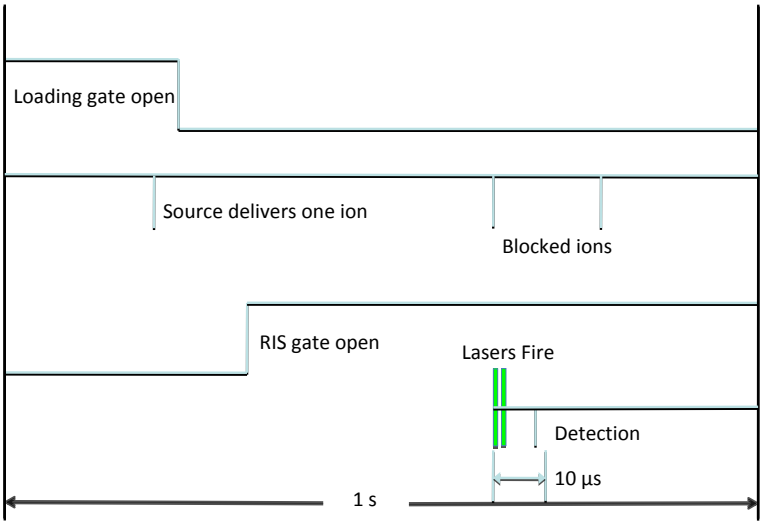

Figure 6.18: Timing for single-ion operation (not to scale). The use of opto-isolators allows for the fast voltage switching required for single-ion operation.

Ba^+-producing decay occurs in the source.

6.4.3 Ionization optical system

The ionization optical system is the same as the one that has been described previously in this dissertation, with a few improvements. The power of the ∼390 nm beam is adjusted by a half-waveplate and a Glan-Laser calcite polarizer, as is done with the ∼553 nm beam. A razor blade, located before the last beam-steering mirror, is used to cut off excess beam at the target (mainly due to the ∼390 nm beam, given its shape). Having beams shaped in this manner allows for maximum overlap between the beams and the desorbed atoms while minimizing the background caused by the beams hitting either the edge of the silicon substrate or guard ring or the titanium mounting pin. An iris, placed after the razor blade, is used to reduce beam halo.

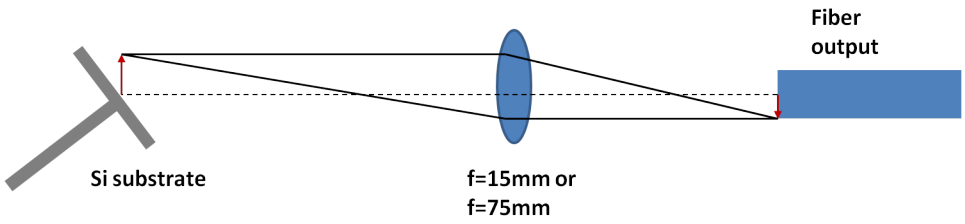

Figure 6.19: Second desorption optical system used for DRIS of barium. An asphere with focal length $f = 15$ mm or $f = 75$ mm is used to directly image the beam onto the silicon substrate.

6.4.4 Desorption optical system

The optical setup before fiber injection now includes high-power mirrors to steer the 1064 nm beam and a half-waveplate and a Glan-Laser calcite polarizer for power control. Fiber injection is achieved by focusing with a $f = 50$ mm lens as before.

Three different optical systems are used for light injection into the experimental vacuum chamber from the output end of the fiber. The first system collimates and focuses the beam to a spot with a 3.34 mm diameter on the silicon substrate and is described in § 6.2.2. A second optical system makes use of an asphere with $f = 15$ mm or $f = 75$ mm to image the beam directly onto the silicon substrate. This allows for an even illumination across the substrate that avoids creating undesirable hot spots. A schematic diagram of this optical system can be seen in Fig. 6.19. A CCD camera can be used to confirm that the image is focused. A comparison between these two optical systems is shown in Fig. 6.20. The top picture shows the beam spot created on the silicon substrate by collimating and focusing a red diode laser. The diode laser is injected into the desorption fiber and is used to align the desorption laser optical elements. The bottom picture shows the YAG desorption laser beam imaged onto the substrate with an asphere, as obtained by a CCD camera. Though the image is saturated, it is useful for determining the exact size of the beam spot, which in this case matches that of the substrate completely.

The third optical system makes use of a pair of cylindrical lenses with $f = 12.7$ mm and $f = 25.4$ mm to achieve a circular beam with a 4 mm diameter parallel to the

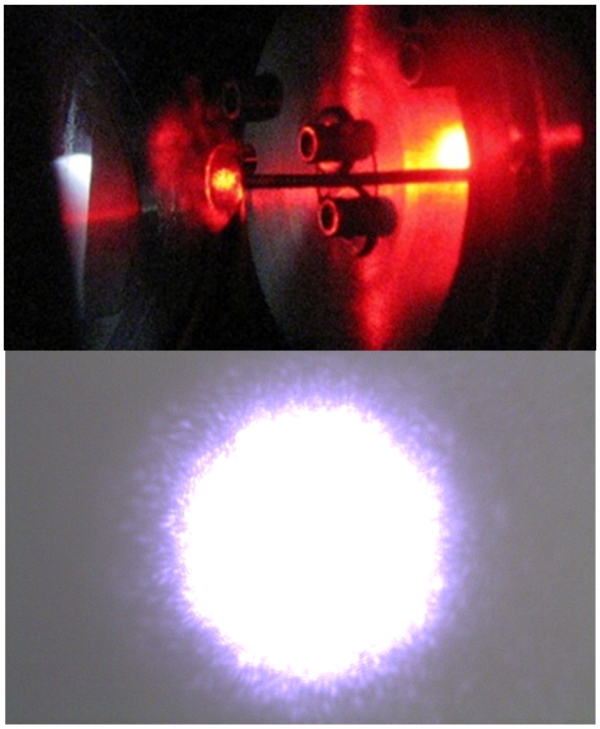

Figure 6.20: Comparison of beam spots created by different desorption optical systems used in the Single-Ion Setup. The top image shows the spot created by collimating and focusing a red diode laser. The bottom image shows the spot created by imaging an infrared YAG laser, which allows for even illumination across the silicon substrate.

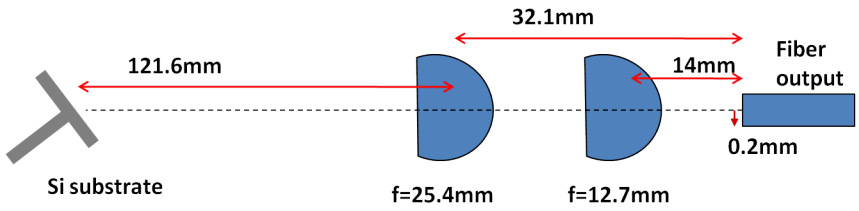

Figure 6.21: Third desorption optical system used for DRIS of barium. Two cylindrical lenses are used to create a circular beam with a 4 mm diameter parallel to the Si substrate.

silicon substrate. This is necessary because injecting the beam through a window at an angle results in an elliptical beam that unevenly illuminates the target. A schematic diagram of this optical system can be seen in Fig. 6.21. These two new optical systems aim to maximize laser coverage of the substrate while achieving an even energy distribution across it, so that no part of the substrate is likely to receive more energy than others, and so no barium atoms are preferentially desorbed over others located in a different position.

A new Q-switched Nd:YAG laser [8], with an internal variable attenuator, is also used for desorption.

6.4.5 Results

To test that both the ion source and the ion guides are working properly, the electrode voltages are set so that ions can travel from the source directly to the CEM for detection. A typical time-of-flight spectrum for this configuration is shown in Fig. 6.22. This spectrum is nearly identical to the one obtained during source characterization (Fig. 5.6), which indicates that the source has not degraded over time. SIMION simulations (overlayed in red) indicate that the Ba^+ time of flight should be 9.3 μs and the Ba^+ rate detected by the CEM should be 0.18 Hz, while the measured time of flight is 10.2 μs and the Ba^+ rate is 0.55 Hz. The agreement between predicted and measured times of flight and the similitude in rates suggest that the voltage settings

[8]Model Minilite I, Continuum, Santa Clara, CA.

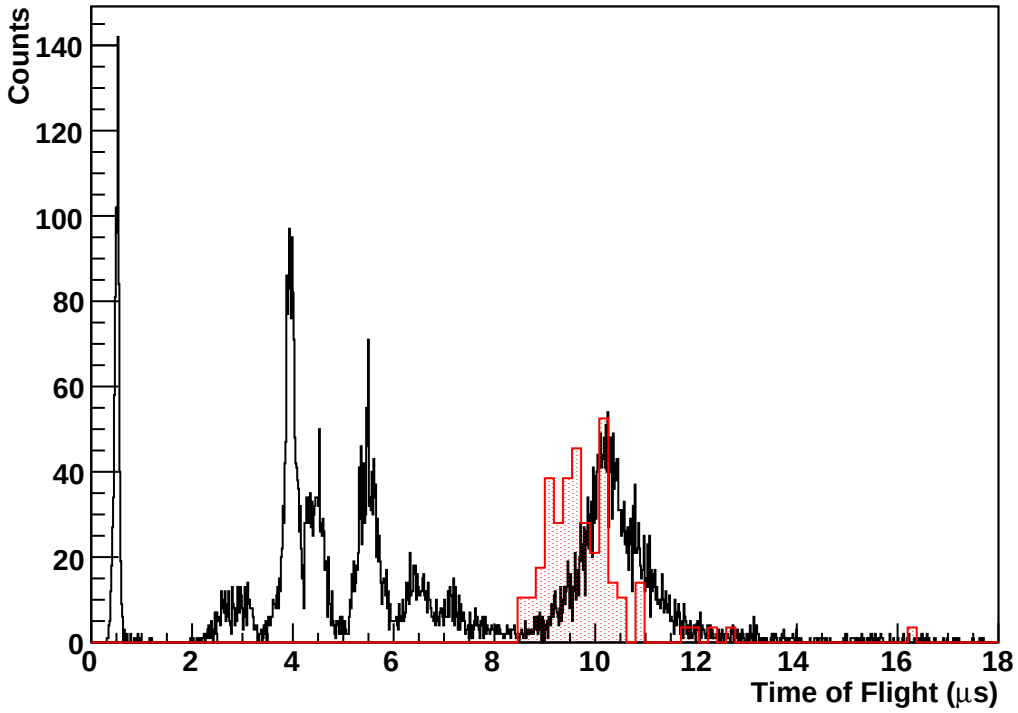

Figure 6.22: Time-of-flight spectrum for the barium source in the Single-Ion Setup. Electrode voltages are set so that the ions can travel from the source to the CEM directly. The Ba^+ peak can be seen at 10.2 μs. The simulated Ba^+ peak, overlayed in red, is at 9.3 μs.

for the electrodes are correct, and the ion optics are working as expected.

For actual data taking the experimental setup is first operated in the "very few ions" mode, even though single-ion operation is possible. Having more ions allows for better optimization of all the parameters that can affect the Ba^+ pulse. Once this signal is maximized, the number of ions can be reduced from a few to one. Data taking thus proceeds by loading the Si substrate for 8000 source triggers. This delivers about 250 Ba^+ ions to the substrate. The voltages are then set to the "DRIS" configuration and lasers are run at 10 Hz for 1200 shots in the following configuration, alternating every 50 shots:

- desorption and ionization lasers are on
- only ionization lasers are on
- only desorption laser is on

Running the lasers in this configuration allows for differentiation of the effect of each laser on the ion signal. Any ions produced by this process are then detected by the CEM. This cycle is repeated for a total of four or five cycles.

The laser powers are monitored with photodiodes, and a PID loop continuously adjusts the half-waveplates to keep the laser powers within a setpoint. This minimizes abnormal ion pulses created by shot-to-shot and long-term power fluctuations. The signals from both the ion source and the CEM are digitized with NI 5114 waveform digitizers. Signals from the photodiodes are digitized with a NI 5105 digitizer [9].

A data set typically consists of 6000 records. A TTL output pulse from the desorption laser triggers the data acquisition for each record. All laser powers, wavelengths, waveplate angles, source load number, laser shot number, which lasers are on and off, room temperature, CEM waveform, and photodiode waveforms are recorded in each data record.

Data is taken using all three desorption optical systems and all target types, shapes, and sizes described in this section. In none of these setups has a clear and reproducible DRIS Ba^+ pulse been detected. Instead, an ion pulse is seen at 8-11 μs. A typical time-of-flight spectrum is shown in Fig. 6.23. The pulse is independent of the desorption laser, and disappears when the UV ionization laser is detuned from the 389.67 nm resonance. Detuning of the green laser from the 553.54 nm resonance has no effect on the ion pulse.

Two possible explanations for this behavior are presented. First of all, misalignment of the UV laser with respect to the Si substrate so that the beam hits the front surface of the substrate can result in barium ablation and direct production of Ba^+ if the laser power is high enough. Indeed, if the UV laser power is reduced, the pulse disappears. Furthermore, this pulse often (though not always), exhibits a time

[9] National Instruments Model 5105 12 Bit 60 MS/s waveform digitizer

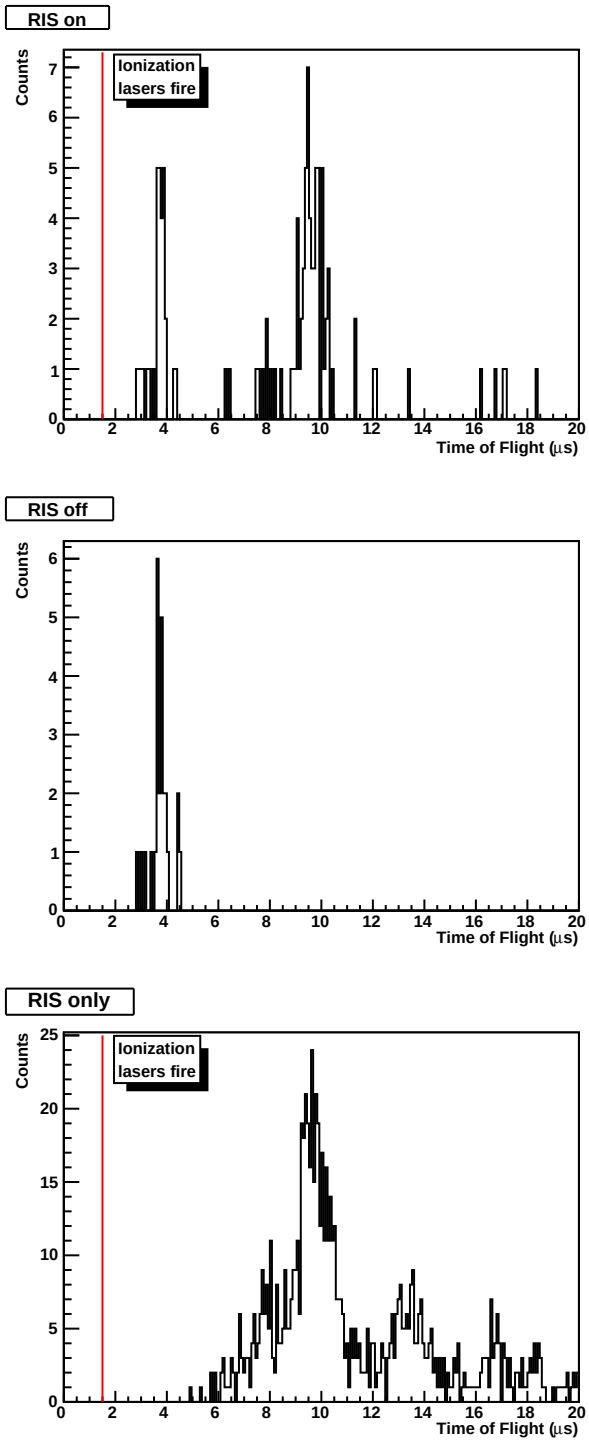

Figure 6.23: Time-of-flight spectra of ions coming off the Si substrate for all three laser configurations (from top to bottom: all lasers on, only desorption on, only ionization on). An ion pulse, dependent only on the ionization lasers, is seen at 8-11 μs.

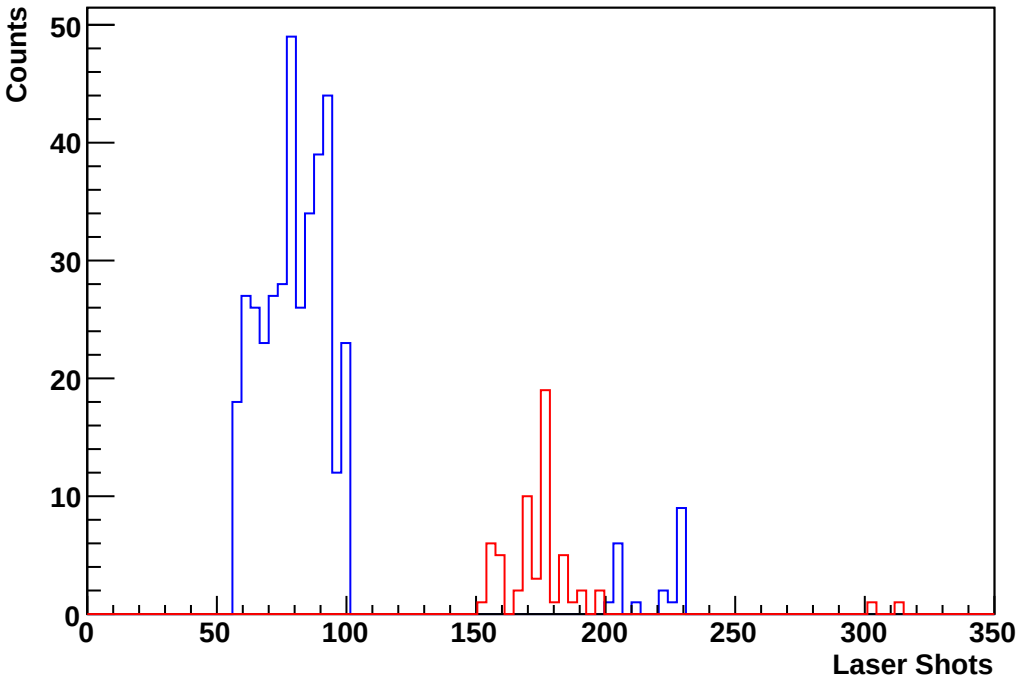

Figure 6.24: Time structure of the ion pulse seen in Fig. 6.23 in the region 8.5-11 μs. The counts in blue correspond to ions detected when all lasers are on, while those in red correspond to ions detected when only the ionization lasers are on. No ions are seen in this region when only the desorption laser is on.

structure similar to that seen in laser ablation, in which the majority of the ions are produced at the beginning, and later laser pulses create less ions. The time structure for the ion pulse seen at 8-11 μs in Fig. 6.23 is shown in Fig. 6.24. However, the fact that this ion pulse is dependent not only on the UV laser power but also on its wavelength seems to indicate a resonance process.

The second explanation is thus that this ion pulse is due to a two-photon RIS process that occurs after UV-induced desorption. As can be seen in Fig. 6.25, an RIS scheme that ionizes barium through a resonant transition at 388.9 nm exists. This would require the original 389.67 nm transition to be substantially power broadened, which might be possible given that the UV laser energy is about an order of magnitude

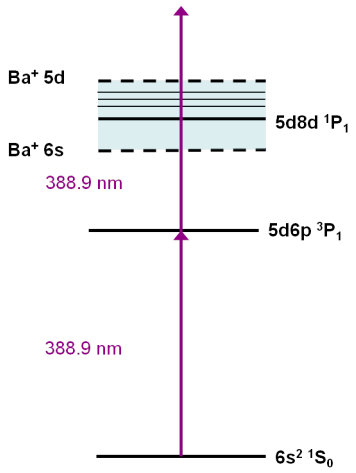

Figure 6.25: Two-photon resonance ionization process for barium, consisting of excitation to a spin-forbidden transition and ionization into the continuum. This ionization scheme can be reached in the current experimental setup if power broadening of the 389.87 nm transition is taking place.

greater than the saturation energy of the transition. This process, in which atoms are desorbed and ionized by one laser tuned to resonant transitions, is called Resonant Laser Ablation (RLA) and is well known [81].

Though still a resonant process, excitation through the spin-forbidden 5d6p $^3P_1$ resonance and ionization into the continuum probably has less sensitivity and is less efficient than the two-laser RIS scheme, so it is not optimal. Nevertheless, RLA of barium was tested in this experimental setup by shining the UV laser on the silicon substrate at an angle, to allow for better desorption and ionization. No ion pulse was seen at any of the laser positions and energies tried, though RLA was not attempted for long.

Instead, experimental efforts have concentrated on determining the reason(s) for the lack of a DRIS Ba^+ pulse. The inability to observe this pulse in the Single-Ion Setup might arise from inefficiencies in one of the three experimental steps (loading barium onto the silicon substrate, desorbing and ionizing barium, detecting Ba^+), or from a combination of these factors. The rest of this chapter discusses the different parameters that might affect the Ba^+ ion pulse and how these issues have been

addressed.

Mobility of barium on the surface of a silicon substrate: Lithium impurities have been known to migrate as positive, singly-charged ions in silicon in temperature ranges of 360-860° C [82], with a diffusion coefficient that is dependent on the temperature. It is possible that on a p-type silicon surface like the one used as a substrate in these experiments barium also acts as a donor and diffuses. This diffusion might be exacerbated by the increase in temperature on the surface of the silicon substrate due to the desorption laser pulse, to the degree that the barium ion migrates to the edges or the back of the substrate where it cannot be desorbed. On the time scale of the duration of the laser pulse (∼10 ns), the diffusion distance is very small, but if the laser spot is misaligned with respect to the barium atom, the number of continuous laser shots (100) might heat the silicon substrate to a high enough temperature for a long enough time for the barium ion to diffuse far enough.

The silicon substrate with the two concentric aluminum rings is designed to mitigate the effects thermal diffusion. Having a potential across the substrate might redirect ions that have drifted around back towards the center of the substrate, so that all barium ions are located within a fixed area. Biasing the rings in the substrate does result in some heating (about 2 mA worth), and it is not known how this affects the ability to desorb barium. No DRIS Ba^+ pulse is seen using this new substrate.

It might also be that defects or impurities in the silicon crystal or topological features on the surface of the substrate caused by laser ablation either enhance diffusion through (not across) the substrate or inhibit desorption of barium. Particulates left over from the cutting process for round substrates, even after sonication, might contribute to an uneven substrate surface or bond to barium to prevent desorption in the single-ion level.

Spatial overlap of ionization lasers: At the single or few-ion level, the spatial overlap between the two ionization lasers has to be exceedingly good. Misalignment might cause the desorbed barium atom to be excited but not ionized, or ionized by another UV process that is not as selective, sensitive, or efficient. This is particularly important in the current setup because the 389.67 nm beam spot is much larger than the 553.54 nm one. In order to improve the spatial overlap between the two ionization

beams, the 390 nm beam is circularized with a pair of cylindrical lenses with f = 25.4 mm and f = 12.7 mm. This makes the beams have the same shape and a diameter ($\sim$2 mm), which makes them easier to align with respect to each other. No DRIS Ba^+ pulse has been seen with this arrangement.

Dependence of Ba^+ time of flight on desorption and ionization position: SIMION simulations of the time of flight of the Ba^+ ion indicate that it is slightly sensitive ($\sim 1\mu$s) to both the desorption position on the Si substrate and the ionization distance from the substrate. The distance of the ionization lasers from the substrate and the delay between the desorption and ionization lasers is scanned so that the best laser position and timing is selected. Ionization of barium is attempted at a distance far enough from the substrate so that ions are not affected by their image charge but close enough so that ions are still localized within a small area for better overlap with the laser beams.

There is a 1.8 μs range of times of flight for any desorption position in the horizontal direction (on a 4 mm substrate), which makes the width of the Ba^+ pulse on a time-of-flight spectrum rather large. When dealing with very few ions, this makes it difficult to see the Ba^+ pulse as it may be smeared and indistinguishable from background. The range in times of flight for the vertical axis is much narrower (0.2 μs), but it widens (to 1 μs) the farther down the substrate barium is desorbed. Because the desorption beam spot has a non-zero diameter, the Ba^+ pulse can be overall quite broad. The silicon substrate with the two concentric aluminum rings serves to mitigate this effect by concentrating the barium ions deposited by the source in a small area, so that the desorption area is also small.

Spectrometer acceptance and voltage settings: Two main factors affect the ion transport efficiency, which in turn affect the overall efficiency of the DRIS process. Firstly, the current design where the ion source and the silicon substrate have direct line of sight but the CEM is perpendicular to the substrate results in complicated electrostatics that might interfere with the ability to detect Ba^+. Secondly, the large energy distribution of atoms emitted by the source and the necessity that these atoms have a high energy for them to be ionized make it hard for the ion optics to focus these ions onto the substrate.

A simulation campaign was undertaken to optimize all the voltages, but this requires a careful balancing act to maximize the barium loading efficiency and the DRIS Ba^+ transport efficiency while minimizing the range in Ba^+ time of flight, which might be impossible. There is also a tradeoff between good electrostatics and easy optical alignment. For example, having the Si guard ring and a larger target improves loading efficiency, but it makes it more difficult to align the desorption laser to the right spot. The current experimental allows for some flexibility but it might not be enough.

Formation of Ba and Si complexes: If the desorption laser power is high enough, it can cause ablation of the surface of the silicon substrate, which creates a variety of ions (see Fig. 6.26). These low-mass particles are detected in the Single-Ion Setup, and their presence constitutes a significant background because the signal is so large that it dwarfs a possible Ba^+ pulse, as shown in Fig. 6.27. Even at 10^{-8} Torr vacuum, it is likely that a monolayer of oxygen covers the surface of the silicon substrate, so formation of $(BaO)^+$ and $(SiO)^+$ complexes is possible. Also, it is well known that depending on the temperature and surface topology, barium can be bonded to one or two [83] or even six [84] silicon atoms. It is possible, then, that laser ablation results in the formation of a variety of barium and silicon complexes that hide Ba^+ from detection, either because the ion optics don't have acceptance for these complexes or because it is hard to resolve different ion pulses in the low-mass area of a time-of-flight spectrum.

In the high-flux and low-flux regimes, the formation of ablation complexes or of other backgrounds might not detract much from the formation and detection of Ba^+, but single barium ions might be more susceptible. The energy of the desorption laser was scanned over a range of a few mJ/pulse with the intent of experimentally finding a point where the ablation background is minimal but the energy is high enough to desorb barium, as was done in the Low-Flux Setup, but this energy threshold was not found.

Neither the use of the specialized silicon substrate, nor improvements to the laser beam characteristics, nor variations of electrode settings undertaken to optimize the

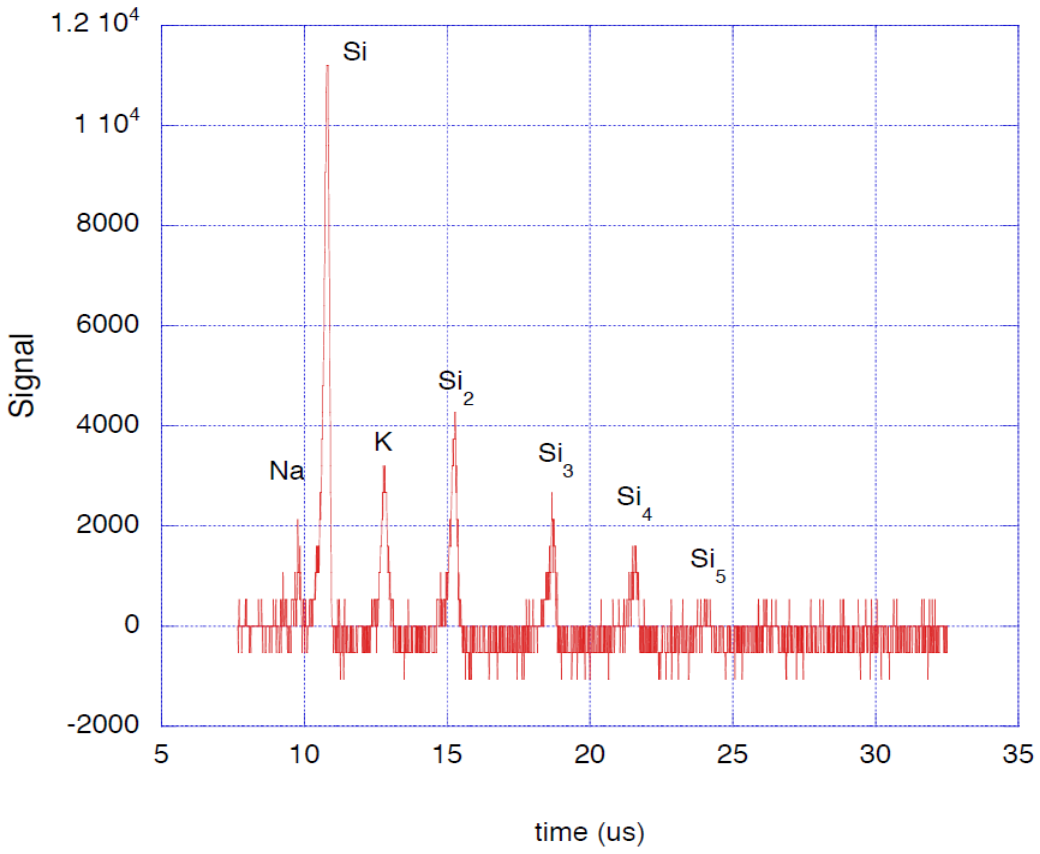

Figure 6.26: Time-of-flight spectrum of species created by laser ablation of silicon. From [7].

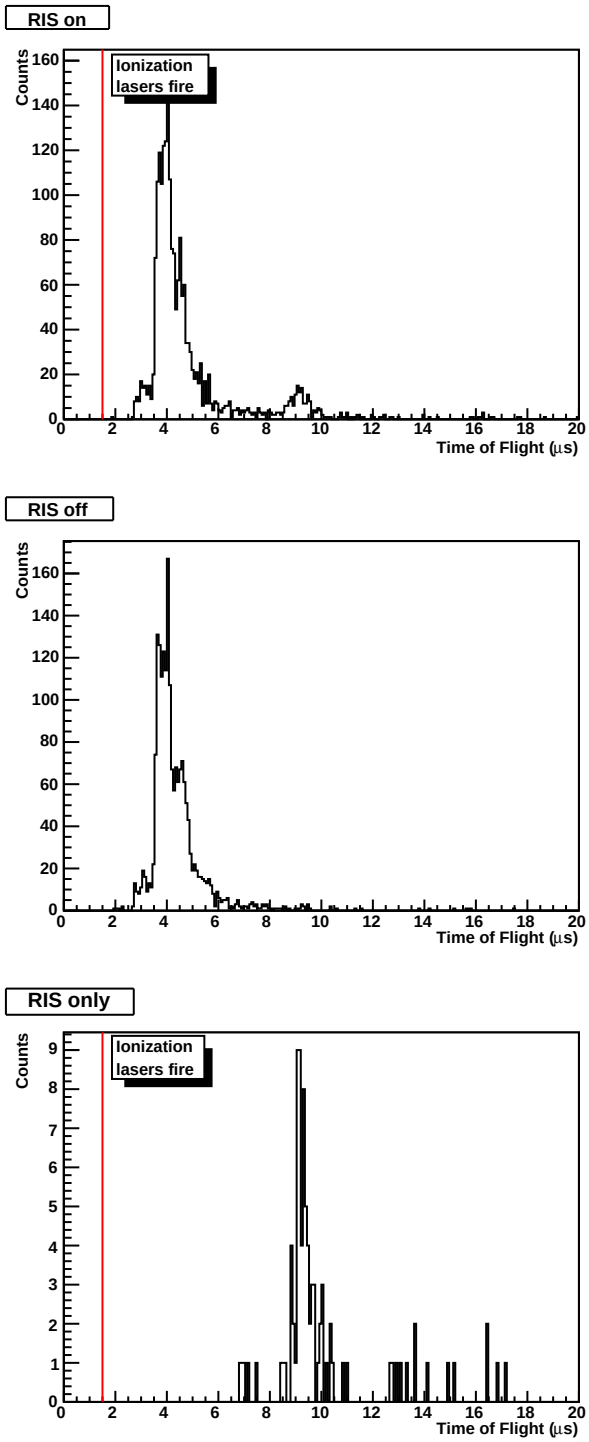

Figure 6.27: Time-of-flight spectra of ions coming off the Si substrate for the same configurations as Fig. 6.23. The large ablation low-mass background, attributed to Si^+ and $(SiO)^+$, makes it difficult to see the possible Ba^+ pulse at 8-11 μs.

Single-Ion Setup, nor running the ion source overnight to load more ions were successful in detecting a DRIS Ba^+ pulse. It might be that operating in the single-ion regime is fundamentally different than doing so in the low-flux regime. Nevertheless, the success in doing DRIS of Ba^+ with the Initial and Low-Flux Setups with a measurable efficiency is encouraging enough to continue this R&D. Chapter 7 gives a general description of the work that will be done after this dissertation to bring the sensitivity of a DRIS ion-transport probe down to the single-ion level.

Chapter 7

Future Directions

The inability of the Single-Ion Setup to ambiguously detect desorbed and resonantly ionized Ba^+ ions does not mean that a DRIS ion-transport probe for EXO is impossible or that it will be abandoned. In fact, a new DRIS experimental setup is being designed, and is described in §7.1. This new setup features several improvements over the previous ones and has the ability to test a variety of experimental concerns, both for DRIS and barium tagging in EXO as a whole. A new source, making use of the spontaneous fission of ^{252}Cf, provides barium ions. The use of this source will confirm whether barium loading was an issue in the Single-Ion Setup. The barium ions are grabbed from xenon in the liquid phase, a test of Ba^+ survival in liquid xenon (LXe) and of the ability to dip a transport probe with minimum disturbance of the fluid. The probe is moved from the LXe chamber to a vacuum spectroscopy chamber with a robotic probe mover, the first demonstration of the entire barium tagging process. Finally, the spectroscopy chamber includes a longer, more sensitive time-of-flight spectrometer with better ion injection optics. This will confirm whether Ba^+ detection was the problem with the previous setup.

A brief discussion on what to consider when implementing a fiber-based DRIS ion-transport probe is presented in §7.2.

7.1 A LXe DRIS Barium Setup

A schematic of the LXe DRIS Setup is shown in Fig. 7.1. This setup employs a ^{252}Cf fission source to produce barium ions. About 5% of the fission products are barium isotopes. The fission source is plated on a platinum foil and mounted on one side of a Cu LXe cell. Daughter nuclei have approximately 70 MeV of energy from the decay, and are stopped 20 μm into the LXe. Two ^{252}Cf activities are used: 100 nCi, which accumulates Ba at a rate of 18.5 Hz and serves to calibrate the system and ensure its proper function, and 27 nCi, which accumulates Ba at a rate of 4.9 Hz and is used for single-ion operation. A photomultiplier tube, mounted on another side of the cell, monitors the source activity. Xenon is liquefied inside the cell by cooling down to $\sim$160 K with a liquid nitrogen-cooled copper cold finger. An ion-transport probe with a biased silicon tip is inserted in the LXe and ions are collected. The probe is moved linearly to the spectroscopy chamber by a robotic mover consisting of a servo motor and a drive screw. The LXe cell is closed off with a gate valve and the chamber is cryopumped down to 10 mTorr, and then turbopumped down to UHV. Desorption and resonance ionization is performed and ions are drifted through a time-of-flight spectrometer for detection. The ion optics and the exact nature of the ion-transport probe are still being considered.

7.2 DRIS Via Fiber

The concept of an ion-transport probe using a fiber with a metalized tip for laser delivery was introduced in §2.3.1 (see Fig. 2.7). For RIS to work in this setup, the metallic coating on the fiber must transmit the resonance and ionization lasers but allow for the desorption of the barium atom. The possible candidate materials for the metallization of the fiber tip have to be conducting, have high ablation thresholds, be nontoxic, and be easy and economical to sputter. Indium tin oxide (ITO) emerges as a viable candidate. ITO is an indium oxide (In_2O_3) material n-doped with tin oxide (SnO_2). Tin substitutes indium sites in the lattice, adding electrons to the conduction band and resulting in a wide band gap of approximately 3.8 eV [85]. ITO

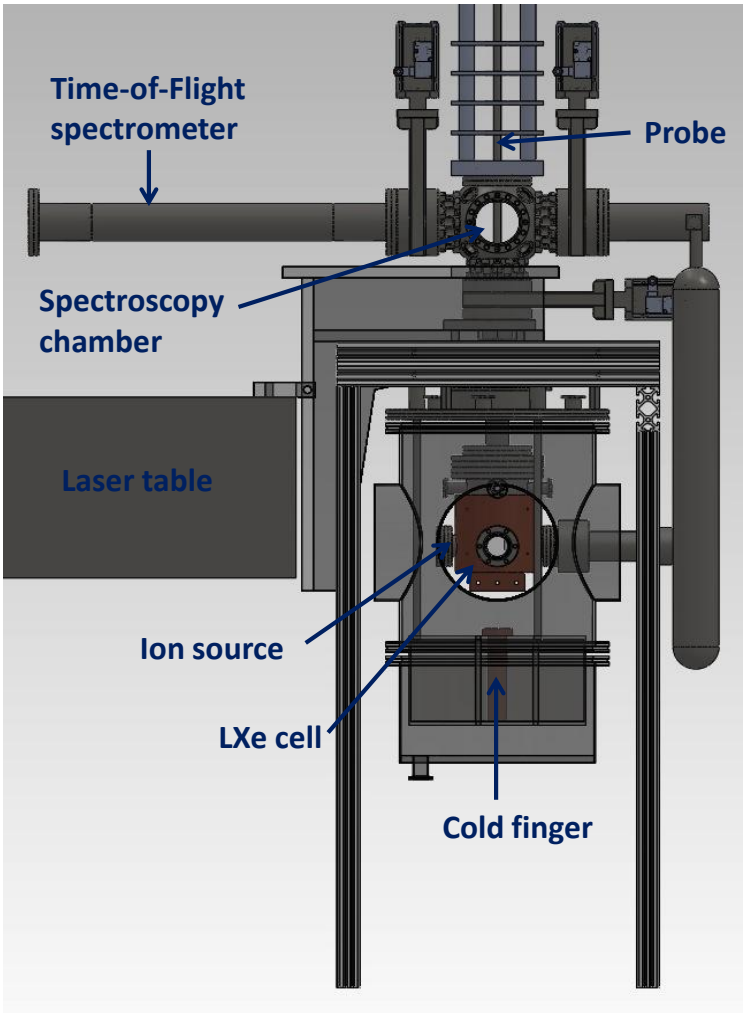

Figure 7.1: Schematic of the LXe DRIS Setup. Courtesy of K. Twelker.

is therefore conductive and transmits well in the visible and near IR. Its fundamental absorption edge lies in the UV but shifts to lower wavelengths with an increase in carrier concentration, due to the Burstein-Moss effect [86], as well as with greater film thickness [87]. So if the film is thin enough (10-100s nm) or doped in the right manner, it would still be transparent to the 389.67 nm ionization beam.

The main concern regarding the use of ITO is in how it affects desorption. It is not clear if ITO is opaque enough at the 1064 nm wavelength currently used for heating to occur and result in thermal desorption. If 1064 nm ligth is not absorbed well enough, two possible solutions can be implemented. First of all, a <300 nm UV laser can be used for desorption, as ITO is opaque at those wavelengths. Secondly, desorption can proceed from the front surface of the fiber tip while the ionization lasers are still delivered via the fiber through the back. This is disadvantageous in the sense that the overlap between the desorption and ionization lasers is not as good as if all three lasers are delivered via the fiber. In any case, one has to consider whether ITO will be ablated when barium is desorbed, and if so, what other materials can be used in its place.

The ablation threshold of ITO has been found to be 2.4 J/cm^2 [88], above the energy density needed for the thermal desorption of barium (see §6.1.1). It should be noted that sub-ablation fluences cause deep melting of the ITO films, which upon resolidification leads to changes in its optical properties, namely a decrease in transmittance [89]. As discussed in the last chapter, an uneven substrate surface is a concern for single-ion desorption and detection. Ti, Ta, and W are other possible coating materials. Their ablation thresholds are relatively high, at least for Ta (0.67 J/cm^2 [90]), but their transmittance at the necessary wavelengths are <20% for thicknesses >15 nm, as calculated by [91]. The coating of fiber tips with ITO, Ti, Ta, and W with a sputtering setup has already been achieved, as a first step in the implementation of a fiber-based RIS ion-transport probe.

Bibliography

[1] F.T. Avignone, S.R. Elliott, and J. Engel, Rev. Mod. Phys. **80**, 481 (2008).

[2] P. Vogel, Nuclear Physics News **16**, 18 (2006).

[3] S.R. Elliott and P. Vogel, Annu. Rev. Nucl. Part. Sci. **52**, 115 (2002).

[4] U. Fano, Phys. Rev. **124**, 1866 (1961).

[5] M.A. Kalyar, M. Rafiq, Samil-ul-Haq, and M.A. Baig, J. Phys. B: At. Mol. Opt. Phys. **40**, 2307 (2007).

[6] H. Petek and S. Ogawa, Annu. Rev. Phys. Chem. **53**, 507 (2002).

[7] W.M. Fairbank, Colorado State University, Private Communication.

[8] Super-Kamiokande Collaboration, Y. Ashie *et al.*, Phys. Rev. Lett **93**, 101801 (2004).

[9] SNO Collaboration, S.N. Ahmed *et al.*, Phys. Rev. Lett. **92**, 181301 (2004).

[10] K. Eguchi *et al.*, Phys. Rev. Lett. **90**, 021802 (2003).

[11] T. Schwetz, M. Tórtola, J.W.F. Valle, New J. Phys. **71**, 113011 (2008).

[12] C. Giunti and C.W. Kim, *Fundamentals of Neutrino Physics and Astrophysics* (Oxford University Press, New York, 2007).

[13] A.S. Barabash, J. Instrum. **1**, P07002 (2006).

[14] KamLAND-Zen Collaboration, A. Gando *et al.*, arXiv:1201.4664v1.

[15] M. Moe, Nucl. Phys. B Proc. Suppl. **19**, 158 (1991).

[16] M. Danilov *et al.*, Phys. Lett. B **480**, 12 (2000).

[17] J. Wodin, *Single ion trapping in a buffer gas and liquid Xe energy resolution studies for the EXO experiment* (PhD Thesis, Stanford University, 2007).

[18] M.P. Green, *In ion probes and traps: barium tagging for the EXO double beta decay detector* (PhD Thesis, Stanford University, 2010).

[19] R. Mohapatra and A. Smirnov, Ann. Rev. Nucl. Part. Sci. **56**, 569 (2006).

[20] E.W. Otten and C. Weinheimer, Rep. Prog. Phys. **71**, 086201 (2008).

[21] U. Seljak, A. Slosar, and P. McDonald, J. Cosmol. Astropart. Phys. **0610**, 014 (2006).

[22] M. Doi, T. Kotani, and E. Takasugi, Prog. Theor. Phys. Supp. **83**, 1 (1985).

[23] F. Boehm and P. Vogel, *Physics of Massive Neutrinos* (Cambridge University Press, New York, 1992).

[24] EXO Collaboration, N. Ackerman *et al.*, Phys. Rev. Lett. **107**, 212501 (2011).

[25] H.V. Klapdor-Kleingrothaus, A. Dietz, H.L. Harney, and I.V. Krivosheina, Mod. Phys. Lett. A **16**, 2409 (2001).

[26] H.V. Klapdor-Kleingrothaus, I.V. Krivosheina, A. Dietz, and O. Chkvorets, Phys. Lett. B **586**, 198 (2004).

[27] A. Aalseth *et al.*, Mod. Phys. Lett. A **44**, 1475 (2002).

[28] A. Balysh *et al.*, Phys. Rev. Lett. **77**, 5186 (1996).

[29] C. Dörr and H.V. Klapdor-Kleingrothaus, Mod. Phys. Lett. A **44**, 1475 (2003).

[30] R. Arnold *et al.*, Phys. Rev. Lett **95**, 182302 (2005).

[31] J. Argyriades *et al.*, Nucl. Phys. A **847**, 168 (2010).

[32] F.A. Danevich *et al.*, Phys. Rev. C **68**, 035501 (2003).

[33] W.J. Lin, O.K. Manuel, G.L. Cumming, D. Krstic, and R.I. Thorpe, Nucl. Phys. A **481**, 477 (1988).

[34] R. Arnold *et al.*, Phys. Rev. Lett. **107**, 062504 (2011).

[35] J. Argyriades *et al.*, Phys. Rev. C **80**, 032501 (2009).

[36] A.L. Turkevich, T.E. Economou, and G.A. Cowan, Phys. Rev. Lett. **67**, 3211 (1991).

[37] M. HFE-7000, http://www.3m.com.

[38] M. Redshaw, E. Wingfield, J. McDaniel, and E.G. Myers, Phys. Rev. Lett. **98**, 053003 (2007).

[39] D. Leonard *et al.*, Nucl. Instr. Meth. A **591**, 490 (2008).

[40] R. Neilson *et al.*, Nucl. Instrum. Meth. A **608**, 68 (2009).

[41] M. Dolinski *et al.*, submitted to J. Instrum. **arXiv:1202.2192**.

[42] M. Green *et al.*, Phys. Rev. A **76**, 023404 (2007).

[43] I.V. Veryovkin *et al.*, Nucl. Instrum. Methods Phys. Res., Sect. B **241**, 356 (2005).

[44] J.E. Parks, H.W. Schmitt, G.S. Hurst, and W.M. Fairbank, Jr., Thin Solid Films **108**, 69 (1983).

[45] G.S Hurst, M.G. Payne, S.D. Kramer, and J.P. Young, Rev. Mod. Phys. **51**, 767 (1979).

[46] L.-W. He, C.E. Burkhardt, M. Ciocca, and J.J. Leventhal, Phys. Rev. A **51**, 2085 (1995).

[47] L.-W. He, C.E. Burkhardt, M. Ciocca, and J.J. Leventhal, Phys. Rev. Lett. **67**, 2131 (1991).

[48] B. Willke and M. Kock, J. Phys. B: At. Mol. Opt. Phys. **26**, 1129 (1993).

[49] S.Niggli and M.C.E. Huber, Phys. Rev. A **35**, 2908 (1987).

[50] H. Metcalf and P. van der Straten, *Laser Cooling and Trapping* (Springer, New York, 2008).

[51] A.L. Schawlow, Science **202**, 141 (1978).

[52] P. Camus, M. Dieulin, A. El Himdy, and M. Aymar, Phys. Scr. **27**, 125 (1983).

[53] J.P. Connerade, *Higly Excited Atoms* (Cambridge University Press, Cambridge, 1998).

[54] M. Aymar and P. Camus, Phys. Rev. A **28**, 850 (1983).

[55] C.H. Greene and M. Aymar, Phys. Rev. A **44**, 1773 (1991).

[56] J.S. Keller, J.E. Hunter III, and R.S. Berry, Phys. Rev. A **43**, 2270 (1991).

[57] Eckert & Ziegler Isotope Products, Private Communication.

[58] K. Moody, Lawrence Livermore National Lab, Private Communication.

[59] R. Weast, editor, *CRC Handbook of Chemistry and Physics*, 56 ed. (CRC, Boca Raton, 1975), p. B-74-76.

[60] J.F. Ziegler, J.P. Biersack, and M.D. Ziegler, *SRIM, The Stopping and Range of Ions in Matter* (Lulu Press, Morrisville, 2008).

[61] http://www.simion.com.

[62] A. Wucher, App. Surf. Sci. **255**, 1144 (2008).

[63] G.L. Eesly, Phys. Rev. Lett. **51**, 2140 (1983).

[64] R.E. Russo, X.L. Mao, H.C. Liu, J.H. Yoo, and S.S. Mao, App. Phys A **69**, S887 (1999).

[65] M.A. Shannon, X.L. Mao, A. Fernandez, W.T. Chan, and R.E. Russo, Anal. Chem. **67**, 4522 (1995).

[66] R.E. Russo, X.L. Mao, and S.S. Mao, Anal. Chem. **74**, 70A (2002).

[67] D. Burgess, Jr., P.C. Stair, and E. Weitz, J. Vac. Sci. Technol. A **4**, 1362 (1986).

[68] I. Hussla and R. Viswanathan, J. Vac. Sci. Technol. B **3**, 1520 (1985).

[69] J.P. Holman, *Heat Transfer* (McGraw-Hill, New York, 2002).

[70] J.F. Ready, *Effects of High-Power Laser Radiation* (Academic Press, New York, 1971).

[71] J.C. Miller and R.F. Haglund, *Laser Ablation and Desorption* (Academic Press, New York, 1998).

[72] S. Hongo, K. Ojima, S. Taniguchi, T. Urano, and T. Kanaji, Appl. Surf. Sci. **82**, 537 (1994).

[73] R.E. Russo, Appl. Spectrosc. **49**, 14A (1995).

[74] R. Forman, Appl. Surf. Sci. **17**, 429 (1984).

[75] B.N. Chichkov, C. Momma, S. Nolte, F. von Alvensleben, and A. Tünnermann, Appl. Phys. A **63**, 109 (1996).

[76] D.M. Karnakis, Appl. Surf. Sci. **252**, 7823 (2006).

[77] V.N. Ageev, Prog. Surf. Sci. **47**, 55 (1994).

[78] B.V. Yakshinskiy and T.E. Madey, Surf. Sci. **451**, 160 (2000).

[79] D.V. Chakarov, L.Österlund, B. Hellsing, and B. Kasemo, Appl. Surf. Sci. **106**, 186 (1996).

[80] M. Montero Díez *et al.*, Rev. Sci. Instrum. **81**, 113301 (2010).

[81] D. Cleveland *et al.*, Appl. Spectrosc. **59**, 1427 (2005).

[82] C.S. Fuller and J.C. Severiens, Phys. Rev. **96**, 21 (1954).

[83] K. Ojima, M. Yoshimura, and K. Ueda, Jpn. J. Apply. Phys. **41**, 4965 (2002).

[84] J. Wang *et al.*, Phys. Rev. B **60**, 4968 (1999).

[85] R.S. Marks, A. Novoa, T. Konry, R. Krais, and S. Cosnier, Mater. Sci. Eng. C **21**, 189 (2002).

[86] E. Aperathitis, M. Bender, V. Cimalla, G. Ecke, and M. Modreanu, J. Appl. Phys. **94**, 1258 (2003).

[87] H. Kim *et al.*, J. Appl. Phys **86**, 6451 (1999).

[88] M. Henry, P.M. Harrison, and J. Wendland, Powerlase Ltd, Unpublished.

[89] T.SzÖrenyi *et al.*, J. Appl. Phys **78**, 6211 (1995).

[90] L. Torrisi, Appl. Surf. Sci. **195**, 8 (2002).

[91] I. Chambouleyron, J.M. Martinez, A.C. Moretti, and M. Mulato, Thin Solid Films **317**, 133 (1998).